

©2019

Hiba Hussein Al-Adhami

ALL RIGHTS RESERVED

AIR-COUPLED SURFACE WAVE TESTING OF PAVEMENTS

By

HIBA HUSSEIN AL-ADHAMI

A dissertation submitted to the

School of Graduate Studies

Rutgers, the State University of New Jersey

In partial fulfillment of the requirements

For the degree of

Doctor of Philosophy

Graduate Program in Civil and Environmental Engineering

Written under the direction of

Nenad Gucunski

And approved by

New Brunswick, New Jersey

May, 2019

ABSTRACT OF THE DISSERTATION

AIR-COUPLED SURFACE WAVE TESTING OF PAVEMENTS

By HIBA HUSSEIN AL-ADHAMI

Dissertation Director:

Dr. Nenad Gucunski

One of the most important parameters in pavement evaluation is the elastic modulus. Significant efforts were put in the development and implementation of nondestructive testing (NDT) techniques for elastic modulus profiling of pavements. Spectral Analysis of Surface Waves (SASW) method is one of the successfully implemented methods. The method utilizes a phenomenon of dispersion of surface waves in layered systems. Once the dispersion curve, representing the surface wave velocity-frequency relationship, is measured, the elastic modulus profile is obtained through an inversion or backcalculation process. Traditional SASW test involves generation of surface wave by application of an impact on the pavement surface, and detection of the propagating waves by a series of sensors placed at various distances from the impact source on the pavement surface of the tested system. The non-contact or air-coupled

SASW method is an extension of the traditional SASW method, where the leaky surface waves are detected using non-contact sensors, instead of the traditional contact sensors.

The main objective of this study is to develop an automated system for pavement elastic modulus profiling based on air-coupled acoustic testing. To improve the speed and automate the modulus backcalculation process, an artificial neural network (ANN) based backcalculation of a pavement modulus profile was developed. Numerical simulations of the air-coupled SASW test using finite elements were used to develop training, testing and validation data sets. Several hundred finite element models of various pavement configurations were used to develop an extensive database of surface wave dispersion curves. The performance of developed ANN models was validated using both numerical and field test data. The validation using numerical data included backcalculation of profiles for synthetic pavement profiles not used in training and testing. The field validation was conducted using field test data collected by a built non-contact SASW testing system. The system was implemented on two pavement sections, which were also evaluated using ground penetrating radar (GPR) and the ultrasonic surface waves (USW) method to obtain pavement layer thickness and top layer modulus, respectively.

Dedication

To My Family

Acknowledgement

The author would like to express her deep gratitude to all her teachers for their guidance and consultation. Special thanks are addressed to the following for their invaluable assistance in the completion of this work:

- To Dr. Nenad Gucunski, her advisor, for his invaluable and continuous support, help and guidance throughout the entire Ph.D. study. The author inspired by the high standards that Dr. Nenad Gucunski sets for himself and his team, and she enjoyed working with him, and she has learned a lot in the field of NDT.
- To Dr. Nazarian, Dr. Ali Maher and Dr. Haw Wang for serving on her defense committee.
- To Dr. Basily B. for sincerely appreciates his assistance during the experimental phase of this research.
- To Dr. Jinyoung Kim for his help and support during different phases of the research.

Finally, the author likes to thank her parents, family and friends for their endless patience, comprehension and love. Especially acknowledge the endless support, encouragement and understanding of her husband, Salah Hameed.

Table of Content

Title Page	i
Abstract	ii
Dedication	iv
Acknowledgement	v
List of Figure.....	ix
List of Tables	xv
CHAPTER ONE	1
Introduction	
1.1 Statement of Problem.....	1
1.2 Research Objective	3
1.3 Research Scope	3
1.4 Outline of the Research.....	4
CHAPTER TWO	6
Background	
2-1 Introduction	6
2-2 Wave Propagation in a Layered Half-Space.....	6
2-2-1 Seismic Wave Types	6
2-2-2 Wave Propagation Equations	13
2-2-2-1 One-Dimensional Wave Propagation.....	13
2-2-2-2 Three-Dimensional Wave Propagation.....	14
2-3 Elastic Waves in Fluid-Solid Half Space System.....	18
2-3-1 Supersonic Leaky Waves	19
2-3-2 Subsonic Surface Waves	20
2-4 Attenuation and Dispersion of Leaky Rayleigh Waves.....	21
2-5 Dispersion Curve in Layered Half-Space	21
2-6 Overview of Wave Equation Solutions for Layered Media	23
2-6-1 Transfer Matrix Approach.....	24
2-6-2 Stiffness Matrix Method.....	24
2-6-3 Global Matrix Method.....	25

2-7 Lamb Waves and Dispersion Curves for Plate	25
CHAPTER THREE	29
Pavement Nondistructive Testing	
3-1 Introduction	29
3-2 Deflection Based Nondestructive Pavement Analyses.....	30
3-3 Ground Penetrating RADAR (GPR) and Noise-Modulated (NM-GPR)	31
3-4 Infrared Thermography.....	34
3-4 Non-Destructive Seismic Methods for Pavement	35
3-4-1 Impulse Response (IR)	36
3-4-2 Ultrasonic Surface Wave (USW) and Ultrasonic Body Wave (UBW)	37
3-4-3 Impact Echo (IE)	38
3-5 Spectral Analysis of Surface Waves (SASW)	41
3-6 Non-Contact NDT	44
3-6-1 Air-Coupled SASW.....	45
3-7 Dispersion Curve Calculation.....	48
3-8 Filtering Criteria	60
3-9 Inversion Methods	63
CHAPTER FOUR.....	65
Numerical Simulation of Air-Coupled SASW Test by FEA	
4-1 Introduction	65
4-2 FE Model Description	67
4-3 Material Properties	69
4-4 General Criteria Implemented in FEA.....	72
4-4-1 Overall dimensions of the model	72
4-4-2 Element Size.....	75
4-4-3 Time Step	77
4-4-4 Impact Duration.....	78
4-5 Receiver locations.....	83
4-6 Verification of Wave Development through the Fluid Solid Half Space System	84
CHAPTER FIVE	88
Inversion Analysis of Air-Coupled SASW Test by ANN	

5-1 Introduction	88
5-2 Overview of Artificial Neural Networks (ANNs)	89
5-3 Transfer Function	91
5-4 ANN Models' Development	92
5-4-1 Development of Training and Testing Sets	92
5-4-2 ANN Training Process	97
5-5 Validation of the ANN Performance Using Numerical Data	105
5-6 Conclusions	111
CHAPTER SIX	112
Field Implementation of Air-Coupled SASW Test	
6-1 Introduction	112
6-2 Air-coupled SASW Test System Description	112
6-2-1 Hardware Platform Integration.....	112
6-2-2 Software Platform Integration.....	115
6-3 Extraction of Radiating Surface Wave Signals	121
6-5 Verification of Components of the Integrated System	124
6-6 Validation of the ANN Performance Using Field Test Data.....	133
6-6-1 Case Study 1.....	133
6-4-2 Case Study 2.....	142
CHAPTER SEVEN.....	149
Clouser	
7-1 Summary.....	149
7-2 Conclusions	150
7-3 Recommendations for Future Research.....	152
REFERENCES.....	154

List of Figure

Figure (2-1) Characteristic wave motion: (a) compression (P-wave), (b) shear (S-wave), (c) Rayleigh, and (d) Love wave (Bolt 1976; Gedge and Hill, 2012; Foti et al., 2017).	9
Figure (2-2) Amplitude ratio vs. dimensionless depth for Rayleigh wave (Richart et al., 1970)	10
Figure (2-3) Relationship between Poisson's ratio ν and propagation velocities of compression (P), shear (S), and Rayleigh (R) waves in a semi-infinite elastic medium (Richart, 1962; Heisey et al., 1982)	11
Figure (2-4) Displacement distributions of waves from a circular footing source on a homogeneous, isotropic, elastic half-space (Woods 1968).....	12
Figure (2-5) Particle displacement for compression waves.....	17
Figure (2 6) Particle displacement for shear waves	18
Figure (2-7) Development of evanescent surface waves over a soil surface (Ryden et al., 2009).....	20
Figure (2-8) Geometric dispersion of surface waves in vertically heterogeneous media (a) sketch of amplitude of the surface wave decreasing with depth at different wavelengths(b) dispersion curve in phase velocity vs. wavelength and frequency domains. (Foti et al., 2017)	22
Figure (2-9) A three layers plate with half-space at the top and bottom (Lowe, 1995)....	25
Figure (2-10) Schematic of a plate with isotropic material and traction-free boundaries	26
Figure (2-11) Mode shapes of (a) symmetric and (b) antisymmetric Lamb wave propagation (Kuttruff, 1991).....	26
Figure (2-12) Lamb waves' dispersion curves in plate (Ryden, 2004)	27
Figure (3-1) GPR B-scan image of a pavement (Celaya et.al, 2018)	32
Figure (3- 2) NM-GPR image of a pavement (Reeves and Muller, 2012)	33

Figure (3- 3) IR image showing serious cyclic end-dump temperature differentials in a hot-mix asphalt mat (Philips and Willoughby, 2003).....	35
Figure (3- 4) Principal of IR technique (Gucunski et.al, 2013)	37
Figure (3- 5) Evaluation of the modulus of elasticity and the thickness of the overlay by UBW and IE methods (Gucunski and Maher, 2002).....	39
Figure (3- 6) Portable seismic pavement analyzer (Celaya et al., 2009).	40
Figure (3- 7) Schematic of SASW test	41
Figure (3- 8) SASW receivers' configuration (a) CRMP (b) CSR (Nazarian and Stokoe, 1985)	42
Figure (3- 9) (a) Multi-channel records and (b) MASW analysis results for the asphalt pavement (Ryden et al, 2004)	44
Figure (3- 10) Schematic of contact and non-contact SASW test (Lu et.al., 2015)	45
Figure (3- 11) The direct and leaky surface waves (Lu et al., 2015).....	46
Figure (3-12) Shadow zone location (Zhu and Popovics, 2008)	47
Figure (3-13) Wrapped and unwrapped phase example	50
Figure (3- 14) Acceleration time histories from a FEM model for different receiver locations	52
Figure (3- 15) Phase angle of cross-power spectrum for four accelerometer spacings	53
Figure (3- 16) Filtered dispersion curves based on acceleration time histories (a) phase velocity vs. wavelength (b) phase velocity vs. frequency.	54
Figure (3- 17) Normalized average dispersion curve	55
Figure (3- 18) Air-coupled sensor records. (a) raw, and (b) windowed data.....	56
Figure (3- 19) Windowed air-pressure time histories for four receiver locations	57

Figure (3- 20) Phase angle of cross-power spectrum for three air-coupled spacing	57
Figure (3- 21) Filtered dispersion curves based on air-pressure time histories (a) phase velocity vs. wavelength (b) phase velocity vs. frequency.	58
Figure (3- 22) Comparison between the dispersion curves for acceleration and air-pressure sensors (example1)	59
Figure (3- 23) Comparison between the dispersion curves for acceleration and air-pressure sensors (example2)	60
Figure (3- 24) Dispersion curves based on air pressure time histories (a) without filtering (b) with filtering.....	62
Figure (4-1) Finite element mesh for a 2D axisymmetric model. (a) Three pavement layer system. (b) Four pavement layer system. (c) Absorbing boundary.	69
Figure (4-2) The source and sensor arrangement.	73
Figure (4-3) Half-sine function shapes as a result of change of the sine power coefficient	82
Figure (4-4) Spectral magnitude for the selected pulse load	82
Figure (4-5) Air-coupled sensors' location	84
Figure (4-6) The air pressure wave at time 1ms.	85
Figure (4-7) Snapshot of the vertical acceleration field.....	87
Figure (5-1) Main concept of forward and inversion problem (Orozco, 2003).....	89
Figure (5-2) (a) Schematic view of typical ANN architecture (b) Artificial neuron (Hecht-Nielsen, 1989)	90
Figure (5-3) Transfer Functions (a) LOGSIG (b) TANSIG (c) Purelin (Hecht-Nielsen, 1989).....	92
Figure (5-4) Normalized dispersion curves defined by same frequency step.....	94

Figure (5-5) Normalized dispersion curve defined by two different frequency steps.	95
Figure (5-6) Effect of the output parameters (a) E_2/E_1 (b) d_2/d_1 (c) E_3/E_1 on the dispersion curve's shape based on air pressure time histories	97
Figure (5-7) Comparison in the computed error of the output parameters (a) d_2/d_1 ; (b) E_2/E_1 and (c) E_3/E_1	100
Figure (5-8) Regression plots for generated by MATLAB ANN toolbox for each output parameter (a) d_2/d_1 , (b) E_2/E_1 and (c) E_3/E_1 for three-layer pavement system	103
Figure (5-9) Four tested cases of pavement profiles.....	106
Figure (5-10) Comparison of actual profiles and output from ANN models for three-layer pavement profiles trained with fixed frequency steps: (a) test case1, (b) test case2	107
Figure (5-11) Comparison of ANNs Models output for three layers pavement profile trained with two different frequency steps: (a) test case1, (b) test case2	108
Figure (5-12) Comparison of ANNs Models output for four-layer pavement profiles trained with two different frequency steps: (a) test case3, (b) test case4	109
Figure (5-13) Comparison of ANNs Models output for four-layer pavement profiles trained by two different frequency steps: (a) test case3, (b) test case4.....	110
Figure (6-1) Schematic view of the built non-contact SASW testing system	113
Figure (6-2) Air-coupled SASW testing system hardware components.....	114
Figure (6-3) The intro page of the computer program for control of the non-contact SASW test.....	115
Figure (6-4) LabVIEW program's four sections (a) setup, (b) display, (c) examination of signal's phase difference, (d) examination of the cross power spectra magnitude, (e) analysis sections and (f) analysis sections.	119
Figure (6-5) Different Time-window designs (a) bin-band pass, (b) bin-low pass and (c) exponential.....	122

Figure (6-6) Leaky surface wave's extraction from the first receiver signal. Raw signal (right), windowed signal (left) by applying (a) bin-band pass, (b) bin-low pass and (c) exponential time-window.....	124
Figure (6-7) Implemented contact and non-contact SASW testing on a concrete floor .	125
Figure (6-8) Low frequency response for the used contact accelerometers	126
Figure (6-9) LabVIEW user interface for data collection and analysis based on contact sensors (accelerometers): (a) setting of the parameters, (b) display of saved signals, (c) cross power spectrum phase and coherence, (d) cross power spectrum magnitude, (e) auto-power spectrum magnitude, and (f) dispersion curve.....	129
Figure (6- 10) LabVIEW user interface for data collection and analysis based on non-contact sensors (microphones): (a) setting of the parameters, (b) display of saved signals, (c) cross power spectrum phase and coherence, (d) cross power spectrum magnitude, (e) dispersion curve.....	131
Figure (6-11) Detected signal by the microphone when the isolators was used.....	132
Figure (6-12) Case study1. (a) Field test layout, (b) GPR scanning	134
Figure (6- 13) GPR B-scans for three test lines.....	135
Figure (6-14) PSPA software program user interface.....	136
Figure (6-15) Implementing air-coupled SASW testing, case study1	137
Figure (6-16) The user interface for setting up the input parameters, case study1	138
Figure (6-17) The user interface with the signal acquisition and analysis for point #6 on test line A, case study 1: (a) time histories of acquired signals, (b)wrapped and unwrapped phase, and coherence, and (c) dispersion curve.	140
Figure (6-18) Validation of the ANN performance through case study 1: (a) the actual pavement structure profile, (b) estimated elastic modulus profiles.	141
Figure (6-19) Drawings of the tested pavement section next to the Richard Weeks Hall of Engineering: (a) plan view with tested locations, and (b) typical cross-section.....	143
Figure (6-20) PSPA software program user interface, case study 2	144

Figure (6-21) Air-coupled SASW testing; case study 2	145
Figure (6-22) The user interface with the signal acquisition and analysis for a test point in case study 2: (a) time histories of acquired signals, (b) wrapped and unwrapped phase, and coherence, and (c) dispersion curve.	146
Figure (6-23) Validation of the ANN Performance, case study 2: (a) the actual pavement structure profile (b) estimated elastic modulus profiles.....	147

List of Tables

Table (3-1) Recommended filtering criteria (Ganji and Gucunski, 1998).....	61
Table (4-1) Values of parameters used in generation of FE pavement profiles for two study cases.	71
Table (5-1) Mean squared error for each ANN models.....	104

CHAPTER ONE

Introduction

1.1 Statement of Problem

One of the most important parameters to evaluate the layer systems, like layered soil or pavement structure is the modulus of elasticity since it is used to characterize the stress-strain behavior of the system. For Pavement system, different methods are available to estimate its profile (i.e. elastic moduli and layers thicknesses); these methods could be addressed under two categories: laboratory test and in-situ test. Generally, these tests have many disadvantages; besides being time consuming and using high-cost equipment, the specimens of laboratory tests core test, for example, could not reflect the in-place material properties because the presence of disturbance due to the in-situ releasing stress and other causing factors. Therefore, significantly increasing efforts towards using in situ non destructive (i.e. non-damaging) tests for system evaluation have been developed.

Seismic methods are an example for in-situ nondestructive test. These methods are based on the characteristic of the wave propagation velocity of elastic waves, in very low strain level, generated from a point source and received by sensors. The Spectral-Analysis-of-Surface-Waves (SASW) method is considered one of these seismic techniques. The method was first introduced by Heisey et al (1982) and has been developed by other researchers at University of Texas at Austin since 1980 ([Nazarian et.al, 1983](#); [Nazarian et.al, 1987](#)).

The SASW test procedure includes three stages. The first stage is collecting the data in the field by generating an impact surface load, so the surface waves will be generated over a wide range of frequencies; then it will be received by a pair of receivers with different configurations. The second stage includes determination of the experimental dispersion curve (i.e. a plot of the phase velocity versus corresponding wavelength or frequency), where the detected signals are transformed into the frequency domain using the Fast Fourier Transform (FFT), and the phase of the cross-power spectrum of the two sensors will be recorded to develop this curve. Finally, the third phase is an inversion of the experimental dispersion curve to obtain the shear wave velocity profile ([Haskel, 1953](#)); detailed explanation can be found in Chapters 3.

The first two phases are considered direct and easy compared with the third one that still needs special attention to find a new inversion algorithm that could accelerate the SASW test, and make the test closer to a fully automated process and achieve the required accuracy in a short time. Many studies have been focused on finding an inversion alternative to accelerate the test's process such as Gucunski and Wood (1992); Yuan and Nazarian (1993); Ganji et.al (1997). One of these inversion alternatives is by using Artificial Neural Net Works (ANN) which is used successfully in a wide engineering applications. The validation of ANN has been improved to accelerate the inversion process. However, still the results of ANN models for the Base layer are weak ([Nazarian et.al, 2004](#)) and investigation a new ANN model is needed.

The non-contact SASW test is considered an extension from the SASW test. It has the same test procedures, but the ground sensors are replaced by non-contact sensors to collect the data (i.e. Leaky surface waves instead of ground vibration) during the first

phase of the test. The potential of air-coupled sensing in SASW testing of concrete and of pavement were previously demonstrated by Zhu and Popovics (2002), and Rydan (2008) respectively.

1.2 Research Objective

The main objective of this research is to develop an automated system for pavement modulus profiling using air-coupled acoustic testing through the use of Artificial Neural Network (ANN) based inversion method. A wider range of thickness and shear wave velocities are predicted using a broad range of input synthetic dispersion curves either generated from the ground vibration signals or from the surface reflected signals.

1.3 Research Scope

To achieve the previous goals, the research work includes the following:

1. Numerical study, implemented by using Finite Element Analysis (FEA) through a commercial ABAQUS Standard, CAE and Explicit to simulate both contact and non-contact SASW test. The numerical study includes generating several hundred hypothetical pavement profile models with a three layer system (single Surface layer, Base layer and Subgrade) and a four layer system (two surface layer includes Surface coarse and Binder coarse, Base layer and Subgrade). The propagation of Leaky Rayleigh waves in a fluid-solid half-space system was

considered by adding an additional acoustic layer behavior (i.e. air layer) to the numerical pavement models.

2. Data processing, using MATLAB software to calculate individual and average synthetic dispersion curves associated with each synthetic pavement profile based on the acceleration and air pressure time histories for contact and air-coupled sensors, respectively.
3. Inversion processing, developing a new ANN models to predict the pavement profile based on the calculated dispersion curves database.
4. Numerical validation, the developed automated system was numerically validated by generated a new pavement profiles.
5. Finally, building up an air-coupled SASW testing system to implement the test and using the field test data to evaluate and verify the recently developed automated system.

1.4 Outline of the Research

This dissertation is divided in to seven chapters. The first chapter introduces the problem statement, and research goals. Chapter two provides a review for previous studies and background related to the wave propagation in layered half-space media. Besides, a general view about the wave propagation equation and the matrix methods to solve it. The fundamental of Leaky Rayleigh waves' propagation in a fluid-solid half-space system are discussed in this chapter too. Chapter three gives a general view about the NDT used to evaluate the pavement layered system, focusing on SASW test and its

new version air-coupled SASW test. Also, this chapter provides the dispersion curve calculation and the generation of the synthetic dispersion curves.

Chapter four includes detailed considerations of the numerical simulation of air-coupled SASW test by FEA; as emphases are placed on finite element analysis aspects in this chapter.

Chapter five is devoted to explain the fundamental concepts of the inversion methods; focusing on the Artificial Neural Networks (ANN) approach, which was considered in this research for the inversion analysis.

Chapter six includes the field implementation of air-coupled SASW test. Air-coupled SASW test is conducted on number of pavement sections to validate the generated ANN models. Finally, Chapter seven presents a summary of this study, conclusions and future study recommendations.

CHAPTER TWO

Background

2-1 Introduction

This chapter includes a literature review of background related to the wave propagation in layered media, fundamental to understanding of the Spectral Analysis of Surface Waves (SASW) testing.

2-2 Wave Propagation in a Layered Half-Space

Soil and pavement systems in most cases can be represented by a layered half-space, or a layered stratum, with constant material properties within each layer (ideal layers) ([Nazarian and Stokoe, 1986](#)). Types of seismic waves and the relationships between their propagation velocities and elastic moduli are reviewed in this section. Two and three-dimensional wave equation formulations will be discussed in this section too.

2-2-1 Seismic Wave Types

Two types of waves can describe the wave motion that is created by a disturbance within an infinite, homogeneous, isotropic, elastic medium. Those are compression and shear waves, so called body waves. On the other hand, at the surface of a half-space, surface waves may form. Those include two wave types: Rayleigh and Love waves. The particle motion due to these two types of seismic waves differs in their moving path and its traveling velocity ([Bolt, 1976](#)).

For the compression waves (P- waves), the particle motion is in the same direction as the direction of the propagated wave, as shown in Figure (2-1a). Compression waves travel faster than the other types of waves, so those appear first in a travel time record. Its velocity (V_{ph}) can be described either in terms of Lamé's constants (λ) and (μ), or in terms of the modulus of elasticity (E) and Poisson's ratio (ν), and the mass density (ρ), as shown in Equations (2.1 and 2.2)

$$V_p = \sqrt{\frac{\lambda + 2\mu}{\rho}} \quad (2.1)$$

$$V_p = \sqrt{\frac{E(1+\nu)}{\rho(1+\nu)(1-2\nu)}} \quad (2.2)$$

Shear waves (also called distortional waves, secondary waves, or S- waves) have a particle motion perpendicular to the direction of wave propagation, as shown in Figure (2-1b). Generally, a shear wave has two components: a vertically polarized shear wave, with a particle motion in a vertical plane, and horizontally polarized shear wave, where the particle motion is in a horizontal plane. In a travel time record, a shear wave appears as the second wave, so it travels slower than a P-wave. The following equations (2.3 and 2.4) can be used to calculate the shear wave velocity, V_s :

$$V_s = \sqrt{\frac{\mu}{\rho}} \quad (2.3)$$

$$V_s = \sqrt{\frac{E}{2(1+\nu)\rho}} = \sqrt{\frac{G}{\rho}} \quad (2.4)$$

On the other hand, the particle motion at the surface of half-space associated with Rayleigh waves can be described as a retrograde elliptical motion (counterclockwise particle motion). It is a result of longitudinal and transverse components of particle motion being 90 degrees out the phase, as shown in Figures (2-1C). By increasing the depth, this particle motion becomes a prograde elliptical motion due to the sign change of the horizontal component, as presented in Figure (2-2). Rayleigh wave in a half-space is a little bit slower than the shear wave, and its corresponding velocity can be estimated from the following equation (2.5):

$$V_R = \frac{0.862 + 1014\nu}{1 + \nu} V_S \quad (2.5)$$

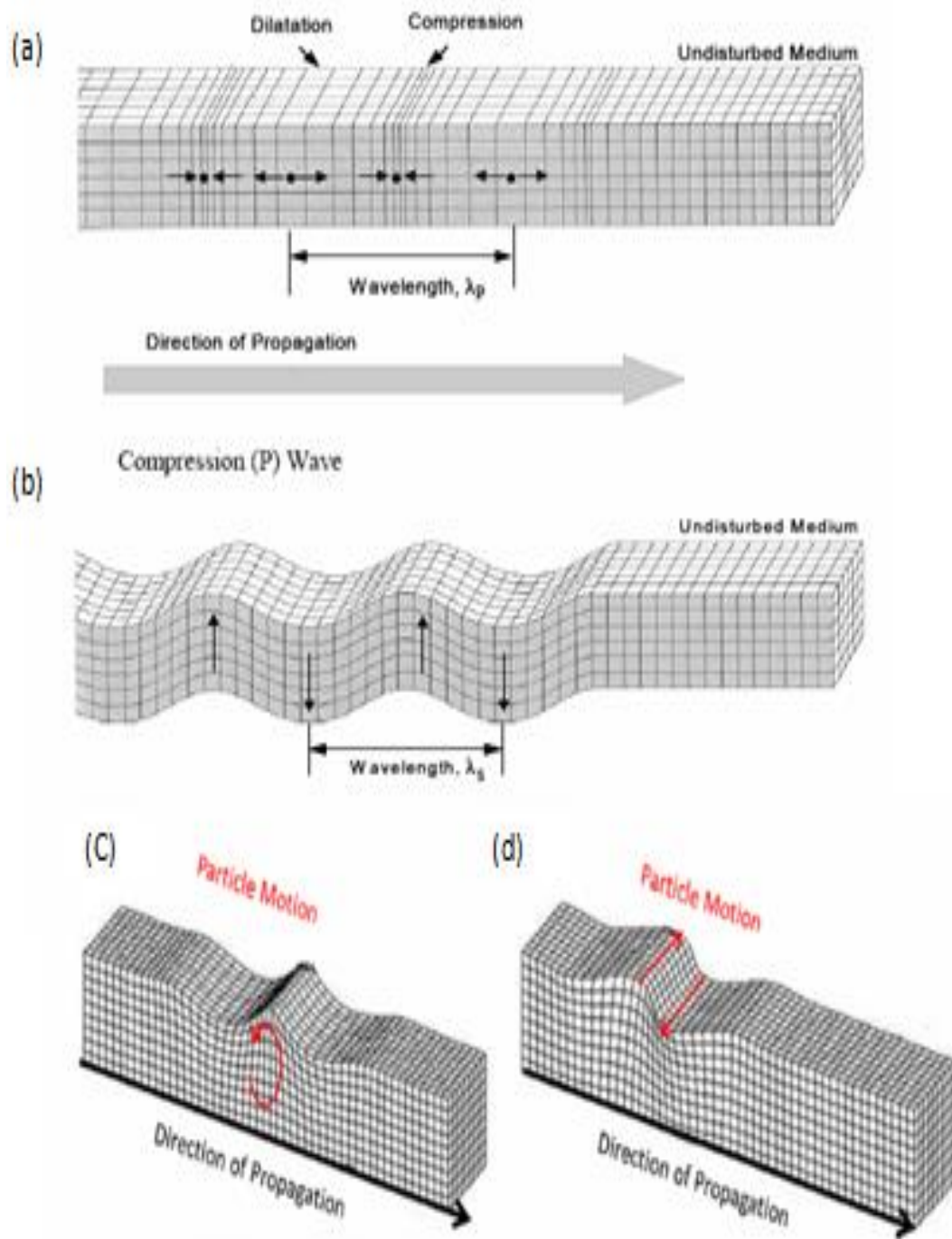


Figure (2-1) Characteristic wave motion: (a) compression (P-wave), (b) shear (S-wave), (c) Rayleigh, and (d) Love wave ([Bolt 1976](#); [Gedge and Hill, 2012](#); [Foti et al., 2017](#)).

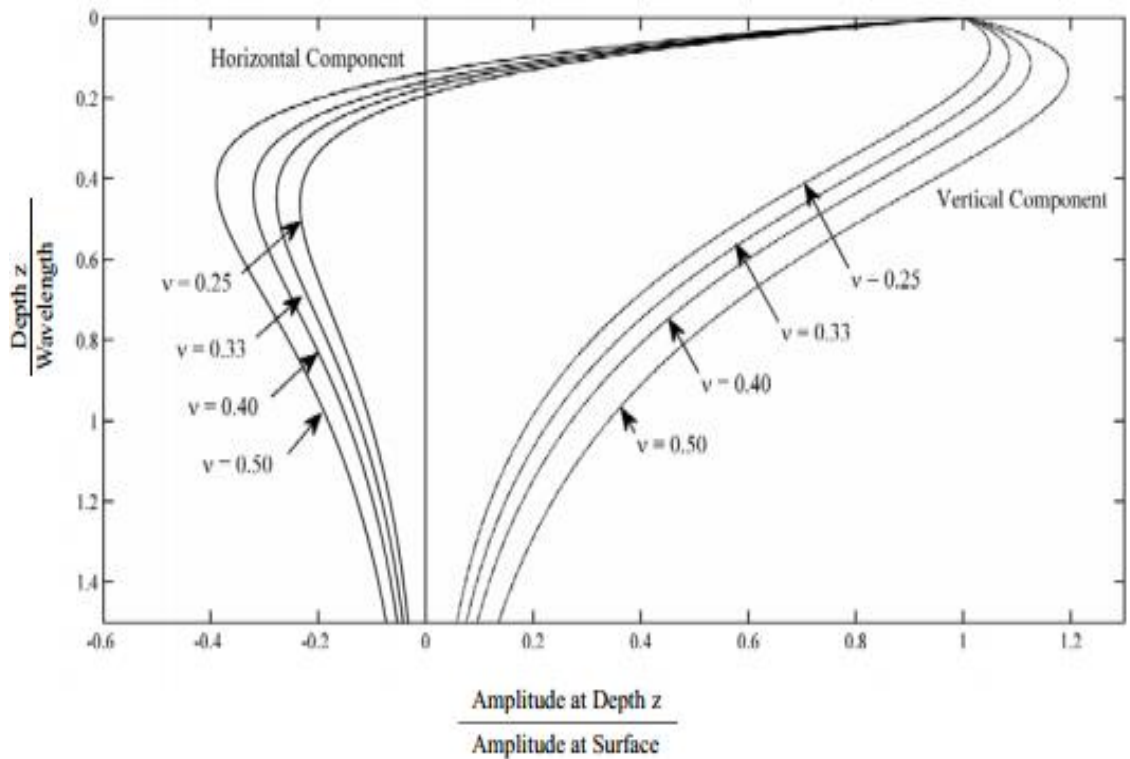


Figure (2-2) Amplitude ratio vs. dimensionless depth for Rayleigh wave ([Richart et al., 1970](#))

From equation (2.5), it is clear that Rayleigh wave velocity does not change with frequency (i.e. waves with different wavelengths travel at the same speed), and that it is dependent on Poisson's ratio and shear wave velocity. However, in a layered half-space, Rayleigh wave velocity varies with frequency. This characteristic is called dispersion and constitutes the core of the SASW method. More details can be found in the following sections.

The relationship between the P-, S- and R-wave velocities as a function of Poisson's ratio is illustrated in Figure (2-3). P- and S- waves attenuate with a factor of $1/r$ and $1/r^2$ in the interior and along the surface, respectively. On the other hand, the amplitude of the Rayleigh wave decreases proportionally to $1/\sqrt{r}$ due to cylindrical wave

propagation, as shown in Figure (2-4). Therefore, the decrease of amplitude with distance due to the geometry of propagation (geometrical damping) is the smallest for the Rayleigh wave.

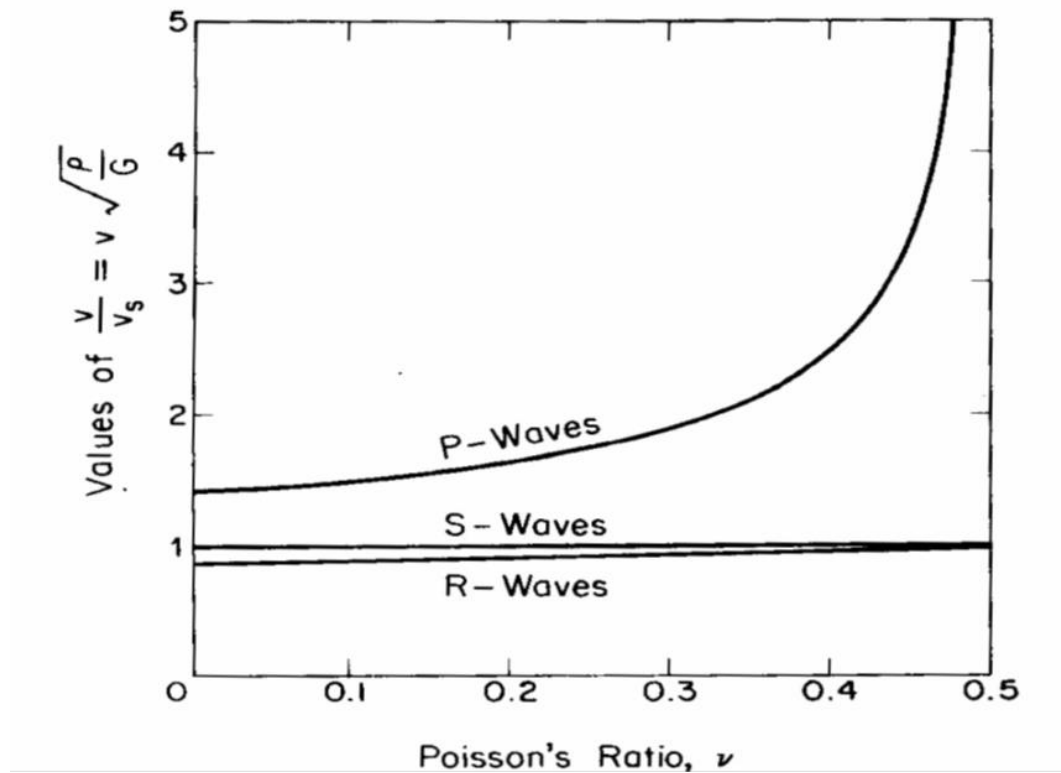


Figure (2-3) Relationship between Poisson's ratio ν and propagation velocities of compression (P), shear (S), and Rayleigh (R) waves in a semi-infinite elastic medium

([Richart, 1962](#); [Heisey et al., 1982](#))

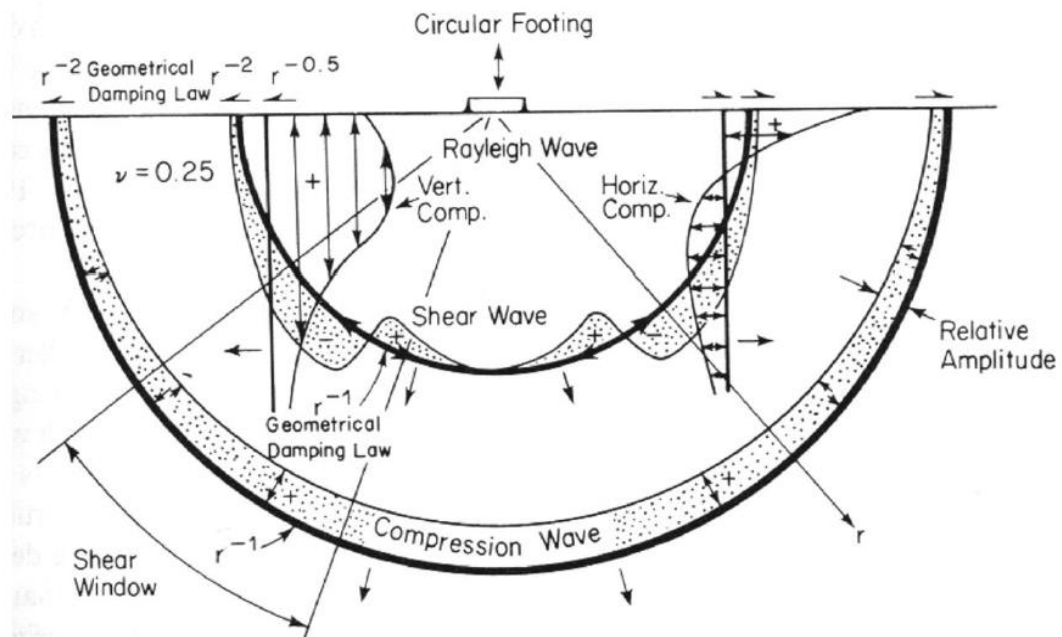


Figure (2-4) Displacement distributions of waves from a circular footing source on a homogeneous, isotropic, elastic half-space ([Woods 1968](#)).

Furthermore, due to a special multiple reflected and refracted of the body waves in the upper surface and at the layer interface reaching the surface, another type of surface waves called Love waves can be generated ([Heiseyet al., 1982](#); [Fotietal., 2017](#)). Love waves are horizontally polarized shear waves confined to a surface layer, as shown in previous Figure (2-1d). All the previous wave types propagate through the medium. There is another wave type that propagates out of the surface, called 'leaky surface wave'. This wave is generated by the particle vibration at the surface due to the surface wave propagation. More details regarding this wave type is provided later in this chapter, including its beneficial usage in non-contact nondestructive testing.

2-2-2 Wave Propagation Equations

The basic wave equations are discussed in this section. More details can be found in [Ewing, Jardetzky, and Press \(1957\)](#); [Elmore](#) and Heald (1969); [Achenbach](#) (1973); and [Graff](#) (1975). In addition, the Rayleigh-Lamb frequency equation for plates is presented in this section.

2-2-2-1 One-Dimensional Wave Propagation

The concept of one-dimensional wave propagation is an important to understand how wave propagation can be used to assess the geometry and material properties of a body. The one-dimensional propagation equation can be derived by applying the equilibrium equation on a differential slice (i.e. along a length of the bar (dx), as defined in Equation (2.6) :

$$-\sigma + \sigma + \frac{\partial \sigma}{\partial x} dx = \rho \cdot dx \frac{\partial^2 u}{\partial t^2} \quad (2.6)$$

where u is the displacement in the x direction, t is time, and ρ is the mass density of bar.

By assuming a linear relationship between stress and strain, the one-dimensional wave propagation can be written as shown below,

$$\frac{\partial^2 u}{\partial t^2} = V_b^2 \frac{\partial^2 u}{\partial x^2} \quad (2.7)$$

where, V_b is the velocity of a longitudinal wave.

2-2-2-2 Three-Dimensional Wave Propagation

Three dimensional waves' propagation has been studied by many researchers ([Graff, 1975](#); [Kolsky, 1963](#); [Rose, 2004](#); [Wolf, 1985](#)). The following sections provide a brief derivation of various wave types. The equilibrium equations for harmonic motion in 3-D are given below:

$$\begin{aligned}\frac{\partial \sigma_X}{\partial X} + \frac{\partial \sigma_{XY}}{\partial Y} + \frac{\partial \sigma_{XZ}}{\partial Z} &= -\rho \omega^2 u \\ \frac{\partial \sigma_{YX}}{\partial X} + \frac{\partial \sigma_Y}{\partial Y} + \frac{\partial \sigma_{YZ}}{\partial Z} &= -\rho \omega^2 v \\ \frac{\partial \sigma_{ZX}}{\partial X} + \frac{\partial \sigma_{ZY}}{\partial Y} + \frac{\partial \sigma_Z}{\partial Z} &= -\rho \omega^2 w\end{aligned}\tag{2.8}$$

To solve the equations, the strain-displacement, and strain –stress relationships are used.

Strain-displacement equations are:

$$\begin{aligned}\varepsilon_X &= \frac{\partial u}{\partial x} \\ \varepsilon_Y &= \frac{\partial v}{\partial y} \\ \varepsilon_Z &= \frac{\partial w}{\partial z} \\ \gamma_{XY} &= \frac{\partial u}{\partial y} + \frac{\partial v}{\partial x} \\ \gamma_{YZ} &= \frac{\partial v}{\partial z} + \frac{\partial w}{\partial y} \\ \gamma_{ZX} &= \frac{\partial w}{\partial x} + \frac{\partial u}{\partial z}\end{aligned}\tag{2.9}$$

Stress-strain (Hooke's law) is used, where its general form is as shown below:

$$\begin{bmatrix} \sigma_{xx} \\ \sigma_{yy} \\ \sigma_{zz} \\ \sigma_{xy} \\ \sigma_{yz} \\ \sigma_{zx} \end{bmatrix} = \begin{bmatrix} C_{11} & C_{12} & \dots \\ C_{21} & C_{22} & \\ \vdots & & \ddots \end{bmatrix} \begin{bmatrix} \varepsilon_{xx} \\ \varepsilon_{yy} \\ \varepsilon_{zz} \\ \varepsilon_{xy} \\ \varepsilon_{yz} \\ \varepsilon_{zx} \end{bmatrix} \quad (2.10)$$

In terms of the two Lamé's elastic constants, λ and G , the Hooke's law is:

$$\begin{aligned} \sigma_{xx} &= \lambda\varepsilon + 2\mu\varepsilon_{xx} \\ \sigma_{yy} &= \lambda\varepsilon + 2\mu\varepsilon_{yy} \\ \sigma_{zz} &= \lambda\varepsilon + 2\mu\varepsilon_{zz} \\ \sigma_{xy} &= \mu\varepsilon_{xy} \\ \sigma_{yz} &= \mu\varepsilon_{yz} \\ \sigma_{zx} &= \mu\varepsilon_{zx} \end{aligned} \quad (2.11)$$

where, ε is the strain, μ is the elastic modulus and Lamé's elastic constants λ and G

$$G = \frac{E}{2(1+\nu)} \quad , \quad \lambda = \frac{\nu E}{(1+\nu)(1-2\nu)} \quad (2.12)$$

By substituting stress-strain and strain-displacement relations in the equilibrium equations, the following equations can be obtained:

$$\rho \frac{\partial^2 \mathbf{u}}{\partial t^2} = (\lambda + \mu) \frac{\partial \varepsilon}{\partial x} + \mu \nabla^2 \mathbf{u}$$

$$\rho \frac{\partial^2 v}{\partial t^2} = (\lambda + \mu)v + \mu \nabla^2 v \quad (2.13)$$

$$\rho \frac{\partial^2 w}{\partial t^2} = (\lambda + \mu) \frac{\partial \varepsilon}{\partial z} + \mu \nabla^2 w$$

where ∇^2 is the Laplace operator:

$$\nabla = e_i \frac{\partial}{\partial x_i} = \left(\frac{\partial}{\partial x_1}, \frac{\partial}{\partial x_2}, \frac{\partial}{\partial x_3} \right) \quad (2.14)$$

$$\nabla^2 = \frac{\partial^2}{\partial x_1^2} = \left(\frac{\partial^2}{\partial x_1^2} + \frac{\partial^2}{\partial x_2^2} + \frac{\partial^2}{\partial x_3^2} \right)$$

By differentiating each equation (2.14) and adding the results together

$$\frac{\partial^2 \varepsilon}{\partial t^2} = \frac{\lambda + 2\mu}{\rho} \quad (2.15)$$

$$\frac{\partial^2 \varepsilon}{\partial t^2} = V_p^2 \nabla^2 \varepsilon \quad (2.16)$$

$$\frac{\partial^2 \varepsilon}{\partial t^2} = \frac{\lambda + 2\mu}{\rho} \nabla^2 \quad (2.17)$$

V_{ph} is the velocity of a compression wave, for which the particle displacement is parallel to the direction of wave propagation, as shown in Figure (2-5), and as discussed previously in section (2-1).

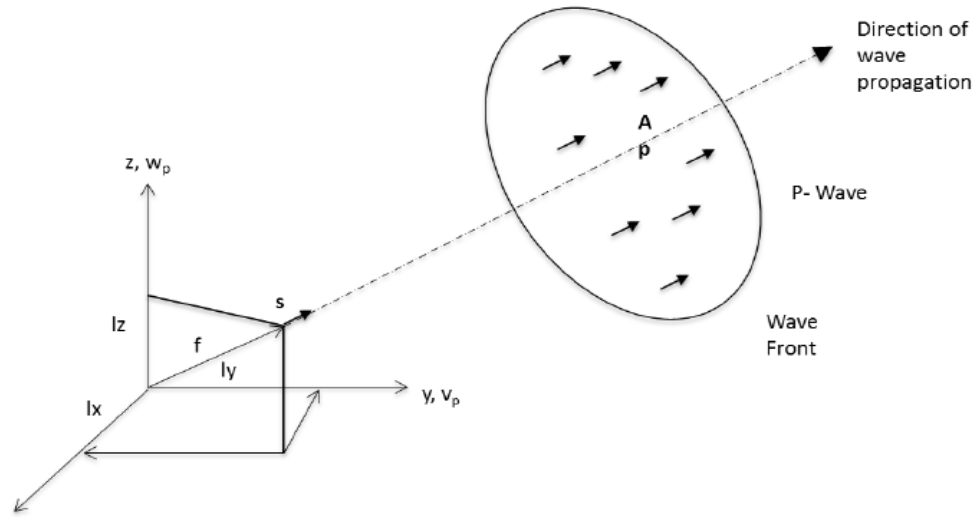


Figure (2-5) Particle displacement for compression waves.

Additionally, the wave equation for a shear wave can be expressed by differentiating equation (2.13) with respect to z and equation (2.14) with respect to y ; and subtracting one from the other. The following wave equation will come out as a result:

$$\frac{\partial^2 \Omega}{\partial t^2} = \frac{\mu}{\rho} \nabla^2 \Omega \quad (2.18)$$

where,

$$\sqrt{\frac{\mu}{\rho}} = V_s = \sqrt{\frac{G}{\rho}} \quad (2.19)$$

The particle displacement for the shear wave is perpendicular to the direction of wave propagation, as shown in Figure (2-6), and as discussed earlier in section (2.1).

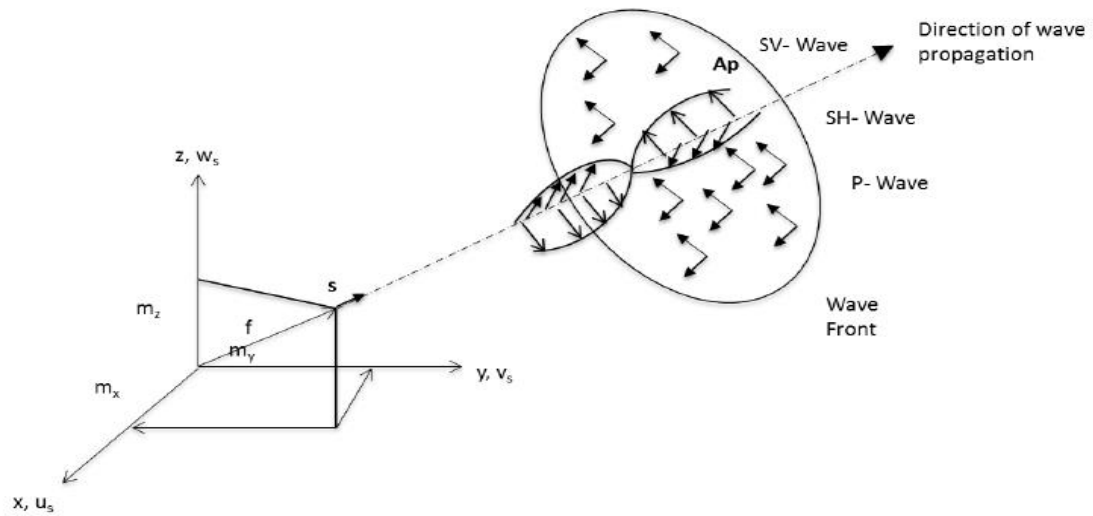


Figure (2-6) Particle displacement for shear waves

2-3 Elastic Waves in Fluid-Solid Half Space System

Leaky surface waves have been studied by many researchers during past 40 years. Viktorov (1967) presented a comprehensive study on the Rayleigh and leaky Rayleigh waves. His study pointed that the leaky Rayleigh waves propagate with a velocity slightly higher than the ordinary Rayleigh wave. Due to a continuous energy radiation into fluid as a result of vibration of the particles on the surface, its attenuation with distance is higher ([Viktorov, 1967](#)).

The effect of viscous damping and heat conduction on the propagation of leaky Rayleigh waves was studied by [Qi \(1994\)](#). He concluded that when the fluid has a Reynolds number larger than 2500, the effect of its viscosity on the propagation of leaky Rayleigh waves can be neglected. Moreover, the full analytical solution for the Lamb's problem in a fluid-solid half space system by using integral transform techniques

was studied by [Zhu and Popovics \(2004\)](#). This problem is associated with isolating the contributions of leaky Rayleigh waves and Scholte waves (i.e. the propagated waves along the interface in both the fluid and solid) generated by a transient point load. These analytical solutions were verified by EFIT (Elastodynamic Finite Integration Technique) numerical simulation by the same authors. More details about this numerical model and the final equations can be found in [Zhu and Popovics \(2008\)](#).

In general, the leaky waves can be classified into two types, based on the surface wave's velocity of the solid half space domain those waves will be generated from. It is explained in the following sections.

2-3-1 Supersonic Leaky Waves

When the waves are propagating in the fast velocity medium along the interface to a lower velocity medium, the supersonic leaky waves will be detected by non-contact or air-coupled sensors ([Ryden et al., 2009](#)). In this study, the detection of supersonic leaky waves was considered, since the numerical models include generation a number of synthetic pavement profiles, which represent fast velocity media, compared to the fluid medium (i.e. air layer). More details regarding the numerical model are presented and discussed in Chapter 4.

2-3-2 Subsonic Surface Waves

In contrast to the supersonic waves, the subsonic surface waves will be detected when the waves propagate in a lower velocity than air medium. Such is the soil surface, where the velocity of surface waves is lower than the wave velocity in air. In this case, the radiation (leaky) waves will not be generated. In this case, the stress at the soil surface is proportional to the pressure in the air. That will generate so called 'evanescent waves' close to the interface ([Ryden et al., 2009](#)). The evanescent wave can decay within a single wavelength distance from the interface. Therefore, it is commonly used in photonic and nanophotonic devices as a waveguide sensor or coupler. Evanescent waves can be amplified, if the soil is unsaturated and the air in the soil pores is coupled to the air pressure above the soil surface. This mechanism is called 'seismic to acoustic coupling'. Figure (2-7) illustrates the development of evanescent waves.

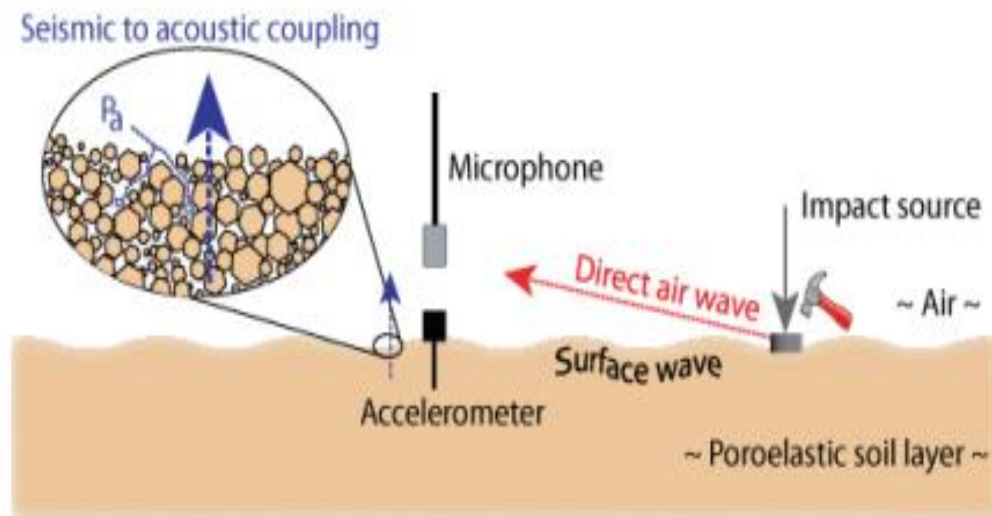


Figure (2-7) Development of evanescent surface waves over a soil surface

([Ryden et al., 2009](#))

2-4 Attenuation and Dispersion of Leaky Rayleigh Waves

When the waves propagate through the fluid-solid half-space system, there will be two attenuation types. In addition to the attenuation of the amplitude of propagation alongside the surface, which it is proportional to the $1/\sqrt{r}$; as discussed previously in sec. (2.1), there is a leaky Rayleigh waves' attenuation caused by continuous radiation (i.e. leakage) of energy into the fluid ([Viktorov, 1967](#); [Zhu and Popovics, 2008](#)). In a frequency domain, this attenuation is an exponential functions of $(-\xi r)$, where ξ has the physical meaning of a wave number k , i.e. the number of waves per unit length. Therefore, a higher frequency (larger ξ) leads to higher attenuation during propagation. In other words, although the phase velocity of leaky Rayleigh waves does not vary with frequency, it shows the dispersion property due to a leakage-induced attenuation ([Viktorov, 1967](#)).

2-5 Dispersion Curve in Layered Half-Space

In general cases and for the engineering purposes, the pavement system can be approximated by a layered half-space or layered stratum. Therefore, its profile can be assumed to be homogeneous and extending to infinity in two horizontal directions. In the vertical direction, it can be assumed to be heterogeneous. This heterogeneity is represented by a number of layers with constant properties within each layer, and the material in each layer as elastic and isotropic.

Surface wave velocities of different wavelengths or frequencies propagate within such heterogeneous media with different penetration depths and different propagation velocities, as illustrated in Figure (2-8a). The velocity variation is termed 'dispersion',

while the distribution of wave velocity as a function of frequency or wavelength is called 'dispersion curve' ([Ewing et al, 1957](#); [Nazarian and Stokoe, 1986](#), [Gucunski, 1991](#); [Gucunski and Maher, 2002](#); [Fotietal., 2017](#)). Dispersion curves for an elastic half-space with a surface layer of different properties are shown in Figure (2-8b). The dispersion curve calculation steps are explained in details in Chapter 3.

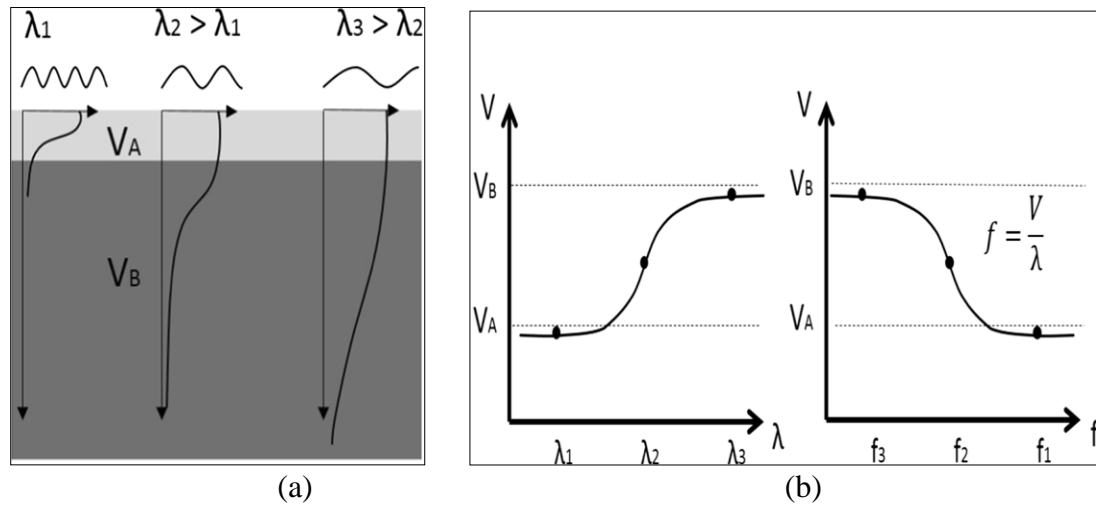


Figure (2-8) Geometric dispersion of surface waves in vertically heterogeneous media
 (a) sketch of amplitude of the surface wave decreasing with depth at different wavelengths
 (b) dispersion curve in phase velocity vs. wavelength and frequency domains. ([Fotietal., 2017](#))

The shape of dispersion curve in a layered half-space is affected by three material properties of each layer for a given profile. These properties are: shear wave velocity, the mass density and Poisson's ratio, however, it was demonstrated by ([Nazarian and Stokoe, 1985](#)) that the effect of the last two parameters on the surface wave dispersion is quite small. So in general, the surface waves are dispersive, only if there is a shear wave velocity variation within a layered half-space.

For a flexible pavement system, when the surface waves are generated at wavelengths shorter than the top layer thickness, the phase velocities are close to the R-wave velocity of the layer. In this case, the top layer acts like a half-space. In contrast, at very long wavelengths, the phase velocity is quite close to the R-wave velocity of the deepest layer. There will be a transition zone in which the phase velocity is bound between the R-wave velocities of the softest and stiffest layers in the profile ([Nazarian and Stokoe, 1986](#)). Otherwise, when the waves propagate in a rigid pavement system, another wave types are formed and a different dispersion behavior can be noticed ([Lamb, 1917](#); [Viktorov, 1967](#)). The characteristics of dispersion curves in such a system are similar to those in plates. This is explained in Section 2-6.

2-6 Overview of Wave Equation Solutions for Layered Media

The analysis of elastic wave propagation in layered media has been studied by many researchers ([Thomson, 1950](#); [Haskell, 1953](#); [Kausel and Peek, 1882](#)). In this section, different matrix analysis based approaches are briefly discussed. The discussion will provide a general background regarding the use of matrix techniques in the solution of the wave propagation due to external loads, and evaluation of the response in general. Solving the wave propagation equations has been considered to be an essential element in estimation of a system's elastic modulus profile from the dispersion curve. This process, called the "inversion process", is explained in detail in Chapter 5.

2-6-1 Transfer Matrix Approach

This approach is based on the use of transfer matrices, i.e. a matrix that transfers the forces and displacements at the top of the layer to the bottom of the layer in the frequency-wave number domain. It was presented by [Thomson](#) (1950) and improved by [Haskell](#) (1953). The fundamental mathematical structure of this matrix is derived by assuming the load to be harmonic in both time and space.

2-6-2 Stiffness Matrix Method

This method is first proposed by [Eduardo Kausel](#) in 1981 to resolve the numerical instability of the transfer matrix method. Where, it only involves displacements as unknowns, so the number of degrees of freedom is reduced comparing with the transfer matrix, which includes both displacement and stresses. Therefore, the computing time is almost 8 times faster. Moreover, the stiffness matrices are symmetric, so less storage is required.

Naturally, when solving for zero loading the stiffness matrix is accompanied by the solution of an Eigen-value problem, which leads to the normal modes without any extra steps.

2-6-3 Global Matrix Method

This method offers an alternative to the Transfer matrix method. It is a suitable method for formulation of problems concerning multi-layers as shown in Figure (2-9).

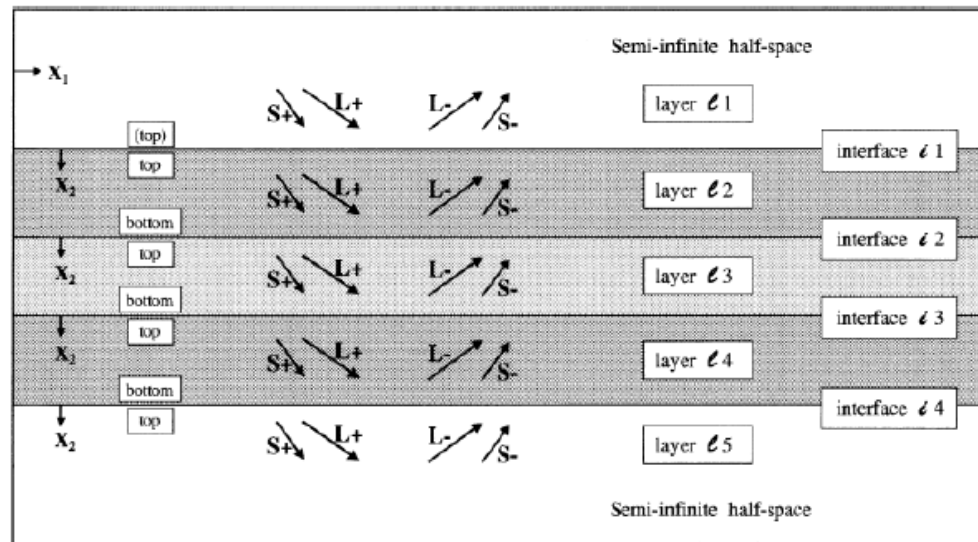


Figure (2-9) A three layers plate with half-space at the top and bottom ([Lowe, 1995](#))

Define the boundary conditions are needed for this method which can be shown as matrices and vectors. Besides, it can simultaneously consider effects of material damping and wave leakage to the environment. It is better than other matrix methods for numerical stability ([Lowe, 1995](#)).

2-7 Lamb Waves and Wave Dispersion in Plates

"Guided waves" is a term referring to the body waves propagating in a finite, homogenous and isotropic medium. It is formed by the interaction between the P-waves and S-waves at the layers interface. When guided waves propagate in an elastic plate, as illustrated in Figure (2-10), such as in a rigid pavement, with a free boundary at the top, it

will generate two-dimensional wave types called Lamb waves (Viktorov,1967). The characteristics of Lamb waves were first studied by Lamb (1917). Generally, the Lamb waves include three wave types: the bending, Rayleigh, and quasi-longitudinal waves.

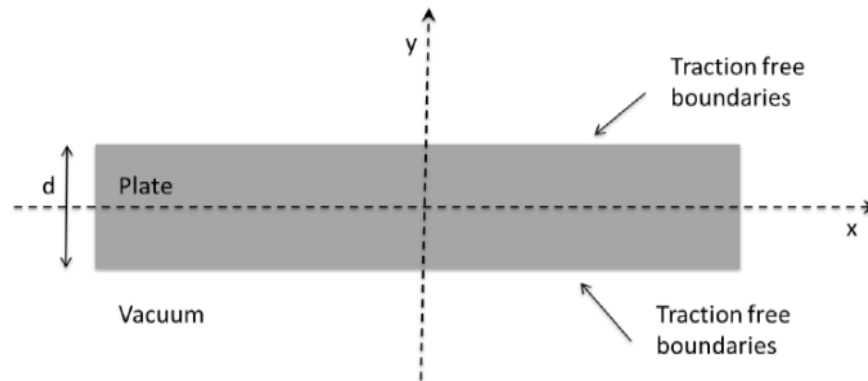


Figure (2-10) Schematic of a plate with isotropic material and traction-free boundaries

The particle displacement associated with Lamb wave propagation can be symmetric or antisymmetric, with respect to the middle plane of the plate, as shown in Figure (2-11).

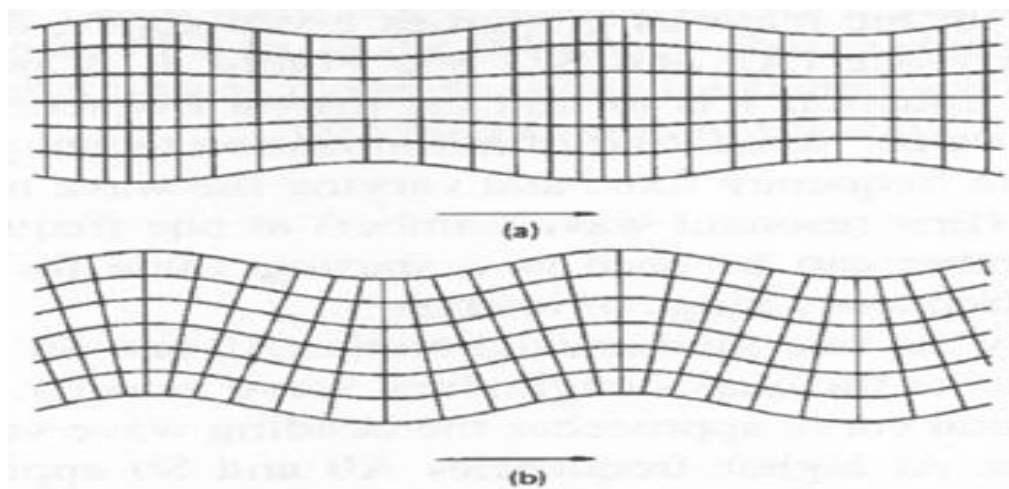


Figure (2-11) Mode shapes of (a) symmetric and (b) antisymmetric Lamb wave propagation ([Kuttruff, 1991](#))

The three Lamb wave types are dispersive, as shown in Figure (2-12), which illustrates the Lamb wave dispersion curves for waves generated in a bridge deck (Ryden,2004).

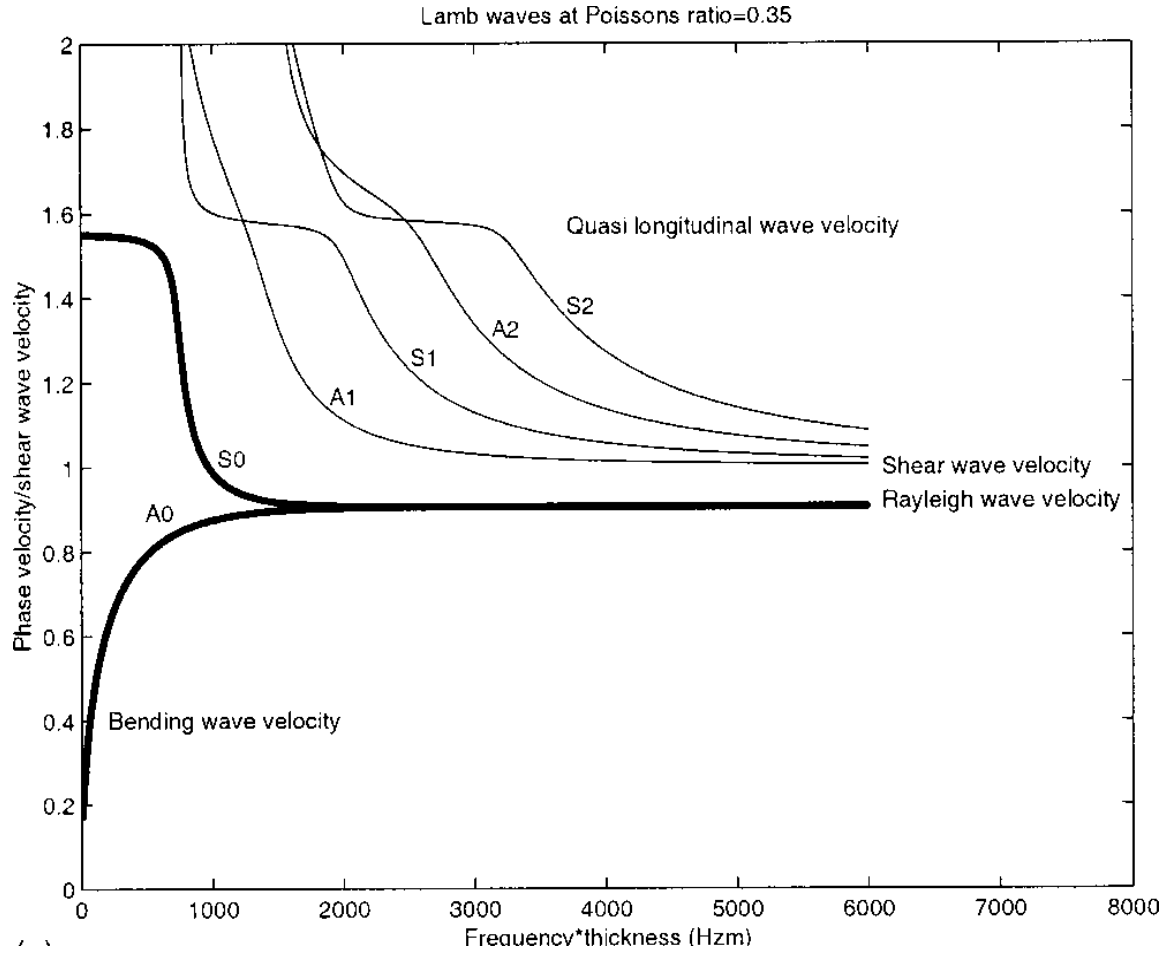


Figure (2-12) Lamb waves' dispersion curves in plate (Ryden, 2004)

The solutions for propagation of symmetric and antisymmetric waves are obtained from Equations (2.20 and 2.21), respectively.

$$\frac{\tan(\frac{\beta h}{2})}{\tan(\frac{\alpha h}{2})} = -\frac{4\alpha\beta k^2}{(k^2 - \beta^2)^2} \quad (2.20)$$

$$\frac{\tan(\frac{\beta h}{2})}{\tan(\frac{\alpha h}{2})} = -\frac{(k^2 - \beta^2)^2}{4\alpha\beta k^2} \quad (2.21)$$

where,

$$\alpha^2 = \frac{\omega^2}{V_p^2} - k^2 \quad (2.22)$$

$$\beta^2 = \frac{\omega^2}{V_s^2} - k^2 \quad (2.23)$$

and h is the thickness, k the wave number ($k=\omega c$), ω is the circular frequency, c is the phase velocity, and V_{ph} and V_s are the compression and shear wave velocities, respectively.

CHAPTER THREE

Pavement Nondestructive Testings

3-1 Introduction

The in-situ nondestructive testing (NDT) methods have become very important for functional and structural evaluation of pavement systems. The main advantage of these techniques is that the pavement material and geometrical properties, and possible presence of deterioration and defects, are evaluated without any induced damage. The application of NDT in pavements can be divided into three main categories: pavement evaluation, pavement diagnostics, and quality control/quality assurance (QA/QC). Various NDT technologies are used to evaluate the structural properties of pavement systems. In some of them, the data can be collected while the equipment is moved continuously along the pavement, such as in Ground Penetrating Radar (GPR) or Traffic Speed Deflectometer (TSD) testing. In the case of other NDT technologies, the measurement is made at particular test points, for example in the case of Impact Echo (IE), Falling Weight Deflectometer (FWD) ([Maser, 2003](#); [Reeves, 2014](#); [Wang and Li, 2016](#)).

The NDT based structural evaluation of pavements depends either on the deformation characteristics of the pavement surface, deflection methods, or on the analysis of elastic waves propagation in pavement layers, seismic methods. Traffic Speed Deflectometer (TSD) test and Spectral Analysis of Surface Waves (SASW) test are examples of those evaluation processes, respectively. Moreover, the evaluation for the defect detection, like debonding, can be based on the detection of thermal radiation from

a pavement system, such as it is with Infrared Thermography (IRT) technique ([Ahmed and Tarefred, 2017](#); [Chao et.al, 2017](#)).

Recently, additional efforts have been made to accelerate some of the NDT methods (e.g., IE and SASW) by replacing the traditional surface-mounted transducers with non-contact acoustic transducers. This chapter explains briefly the techniques commonly used for in-situ NDT of the pavement evaluation. The emphasis will be on the description of the non-contact SASW; including the illustrations of the process in the development of synthetic dispersion curves database that was further used in the development of the ANN-based inversion method, one of the core elements of this research.

3-2 Deflection Based Nondestructive Pavement Analyses

The pavement evaluation concept of this group of NDT methods is based on the application of a static, or dynamic or impact load, and measurement of the pavement surface response to that load. The surface deflection is measured at several points. Plate loading tests and Benkelman beam test are examples when the static load is used. Those are the first tests used and are considered to be time-consuming and of high cost ([Smith et.al, 2017](#)). In contrast the Falling Weight Deflectometer (FWD) technique is widely used for pavement evaluation that involves application of a dynamic load. This technique includes dropping a weight ranging from 40 to 71kN for standard FWD devices, and 53 to 160kN for Heavy Weight Deflectometer (HWD) devices on a plate set on the pavement surface ([Wang and Li, 2016](#); [Smith et al., 2017](#)).

In recent years, a number of higher speed deflection measurement devices have been developed. One such device is the Traffic Speed Deflectometer (TSD), which is operated at a traffic speed. As such, it eliminates the need for a lane closure, as it is in the case of a stationary device, such as the FWD. The TSD consists of a semi-trailer vehicle equipped with a dedicated dead weight of 100 kN (22 kips) located in the proximity of the rear-axle. Besides, it is instrumented with high-rate sensors, including doppler sensors, accelerometers and laser distance sensors. These sensors are used to keep the beam as parallel to the pavement surface as possible during the measurement, and to measure the pavement response due to the TSD weight ([Muller and Reeves, 2012](#); [Nasimifar et.al, 2015](#)). The accuracy and precision of TSD measurements can be influenced by a number of internal and external factors, such as calibration, wind and temperature during the measurement, pavement roughness, and the tire-pavement interaction. ([Zofka and Sunday, 2015](#)).

3-3 Ground Penetrating RADAR (GPR) and Noise-Modulated (NM-GPR)

Pavement evaluation by GPR is considered rapid since there is no direct contact with the pavement surface is required. During the test, electromagnetic waves pulses are emitted via the radar antenna on the pavement surface, and the reflected waves from the interfaces between the materials are captured by the same antenna. The reflected waves carry information about the wave velocity and wave attenuation.

The capability and accuracy of GPR depends on many factors, such as the antenna frequency and operating setting parameters (max time window, EM wave velocity and

sampling interval) ([Karim and Al-Qaissi, 2014](#)). By calculating the electromagnetic wave velocity (v) in a dielectric material, as illustrated in Equation (3.1), and the travel time (t), the depth of reflecting interfaces can be determined ([Bungey, and Millard. 1993](#); [Bungey, 2004](#)).

$$V = C_0/\sqrt{(r)} \quad (3.1)$$

where C_0 is the speed of light in air and r is the relative dielectric constant of a material.

B-scan or C-scan images are used to represent the GPR results. Figure (3-1) shows an example of a GPR B-scan of a pavement section.

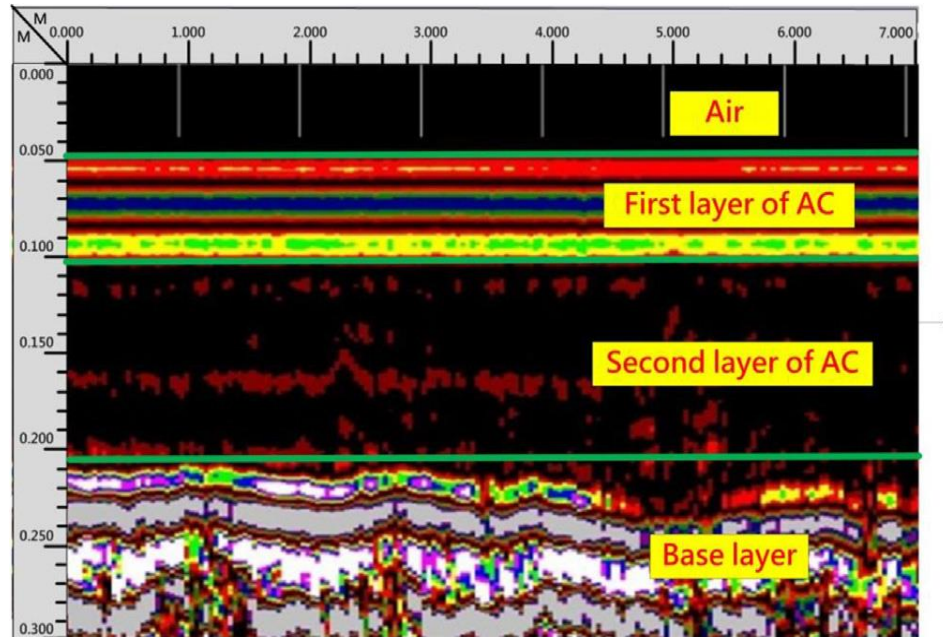


Figure (3-1) GPR B-scan image of a pavement ([Chao et.al, 2017](#))

A new type of high-performance GPR is the Noise-Modulated GPR (NM-GPR). The benefits of this technology include the high operational efficiency and stable performance, which produces a high definition image of the subsurface. Therefore, it can help to complete understanding of the pavement structure, including layer depths, the location of changes in construction and extensions, areas of high moisture content, including water filled cracks, location of utilities and other subsurface anomalies ([Reeves and Muller, 2012](#); [Reeves, 2014](#)). Figure (3-2) illustrates a NM-GPR image of a concrete pavement. It can be noticed that the system performance is such that it allows rebar detection even in the scans from high speed surveys.

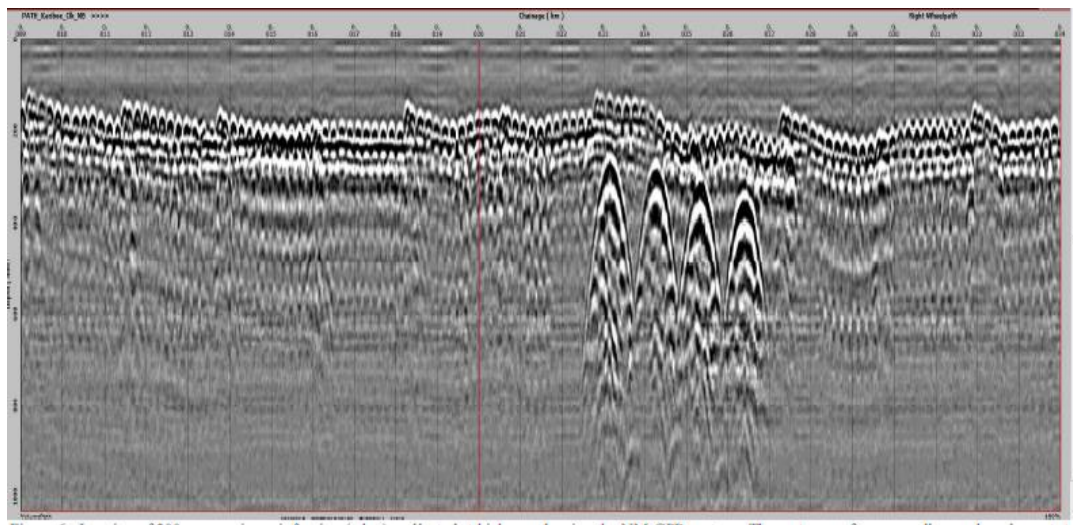


Figure (3- 2) NM-GPR image of a pavement ([Reeves and Muller, 2012](#))

One of the GPR and NM-GPR limitations is that they cannot provide any information about the mechanical properties of the pavement layer material (e.g. elastic modulus). Also, their results generally require being correlated or validated by some other NDE methods ([Gucunski et al, 2013](#); [Reeves, 2014](#)).

A GPR test was implemented during the experimental phase of this research to evaluate the layer thickness of a selected pavement section that was used in the ANN verification. A detailed explanation can be found in Chapter 6.

3-4 Infrared Thermography

Infrared Thermography (IRT) is a technique used for detecting the near surface delamination or debonding in the pavement and other structures. IR images can be collected using a camera installed on the top of a vehicle that can travel at a speed of 16 km/h (10mph) ([Gucunski et.al, 2013](#); [Lu et.al, 2017](#)). The basic principle of this technique is sensing of the emission of thermal radiation from the pavement surface. It depends on two basic principles from the heat transfer that are conduction and radiation. When the pavement is exposed to sun radiation, delaminated parts of a pavement system will interrupt the heat transfer to deeper layers, since air has a lower thermal conductivity than the pavement materials. Therefore, spots that are located above a delamination will be shown as hotter than the spots above sound parts ([Lu et.al, 2017](#)).

Moreover, this technique can be used for HMA paving monitoring. The thermal difference information between different asphalt sections is used to determine issues that may arise in the future of the pavement ([Philips and Willoughby, 2003](#)). Figure (3-3) shows an IR image showing serious cyclic end-dump temperature differentials in a hot-mix asphalt mat.

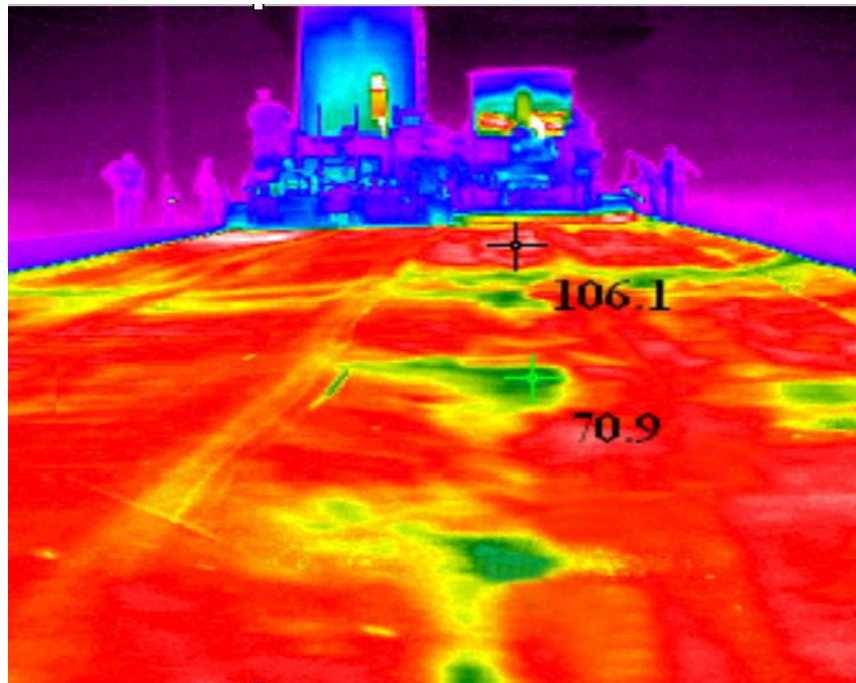


Figure (3- 3) IR image showing serious cyclic end-dump temperature differentials in a hot-mix asphalt mat ([Philips and Willoughby, 2003](#)).

The limitation of this technique is that it does not provide information about the depth of the defect. Finally, the method is affected by surface anomalies and boundary conditions. For example, when sunlight is used as a heating source, clouds and wind can affect the deck heating by drawing away heat through convection cooling ([Gucunski et.al, 2013](#)).

3-4 Nondestructive Seismic Methods for Pavements

The main concept of seismic methods of evaluating the material properties and defects in the structure is based on the generation of elastic waves and measurement of various wave propagation phenomena, most commonly the velocity of wave propagation. These methods are performed at low-strain levels (usually less than 0.001%). Seismic

methods can be categorized into two groups: borehole and surface methods. Surface methods are advantageous, since they do not require boreholes and, therefore, are nondestructive. Moreover, the surface methods are less expensive, since the testing is performed from the surface([Gucunski et.al, 2011](#); [Azari et al., 2014](#); [Tofeldt and Ryden, 2017](#)).

The most common seismic NDT techniques used in evaluation of pavement systems include: impulse response (IR), ultrasonic surface waves (USW), ultrasonic body waves (UBW), impact echo (IE) and spectral analysis of surface waves (SASW). Those are explained briefly below. More details about these techniques including their description, principle of operation, advantages and limitations can be found in [Fernando, Scullion and Nazarien \(2001\)](#); and [Gucunski et al. \(2013\)](#).

3-4-1 Impulse Response (IR)

This technique is used for evaluation of the shear modulus of subgrade in rigid pavements, or the modulus of the overall system for flexible pavements. Also, it is used to detect the presence of voids or loss of support beneath rigid pavements. A closely placed receiver is used to detect the response of a pavement due to applied impact load. Generally, a signal from the impact hammer and the response at a nearby geophone (velocity transducer) are transformed into the frequency domain to obtain the corresponding spectra. A ratio of the displacement and impact spectra represents a flexibility spectrum ([Gucunski and Maher, 2002](#); [Jackson and Gucunski, 2015](#)). Then, by assuming that the pavement acts as a single-degree-of-freedom (SDOF) system, the flexibility spectrum for a pavement with assumed subgrade properties is calculated. Once

the two spectra are matched, the modal properties of the SDOF system provide information about the shear modulus of the subgrade and damping of the system. Figure (3-4) illustrates the principle of IR testing.

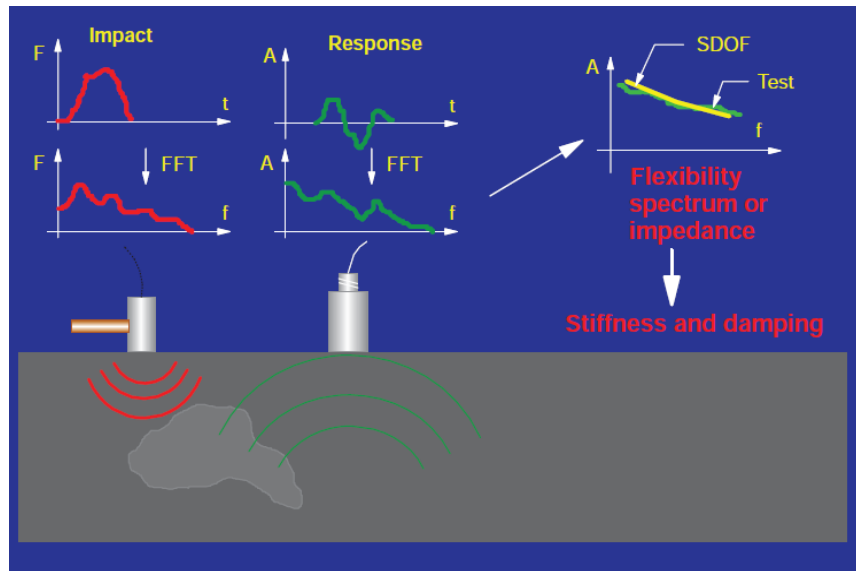


Figure (3- 4) Principle of IR technique ([Gucunski et.al, 2013](#))

3-4-2 Ultrasonic Surface Waves (USW) and Ultrasonic Body Waves (UBW)

These techniques are used in bridge deck and near surface pavement evaluation. Both techniques are based on a wave generation, in a generally high frequency range, to measure the compression wave velocity in the UBW method, and the surface wave velocity in the USW method. During the USW test, the shear wave (S-wave) velocity is determined from the average phase velocity of the surface wave in a high frequency, and often in the ultrasonic frequency range. The velocity is obtained using calculation steps similar to those in the SASW test, which is discussed in detail in sec (3-5). Also, the USW

test was used to study the effect of daily temperature changes in asphalt pavements and irregular curing in concrete pavement ([Gucunski and Maher, 2002](#); [Azari et.al, 2014](#)).

On the other hand, during the UBW test, the compression wave (P-wave) velocity is calculated from the measured arrival time difference between two receivers. Then, by applying the relationship between the modulus, the P-wave velocity, Poisson's ratio and mass density, as illustrated previously in Equation (2.19), the elastic modulus can be obtained. Figure (3-5) provides a schematic of the UBW test, which indicates that the P-wave is the first wave detected by the receivers ([Fernando et al., 2001](#)). The USW technique is a more accurate method than the UBW in evaluation of moduli of the top paving layer. In addition, the USW is capable of measuring modulus variations within that layer.

3-4-3 Impact Echo (IE)

IE test is conducted with the UBW test to determine the thickness of the surface layer, or to detect the location of delamination or debonding. During this test, a receiver close to the impact source is used, as shown in Figure (3-5). The fundamental concept of this test is based on the fact that a significant or complete reflection of P-waves occurs at an interface, if there is a significant change in the stiffness of a medium. Therefore, the resonant or "return" frequency of the P-wave reflected from either the bottom of the surface layer or the delamination ([Azari et.al, 2014](#); [Olson, 2018](#)).

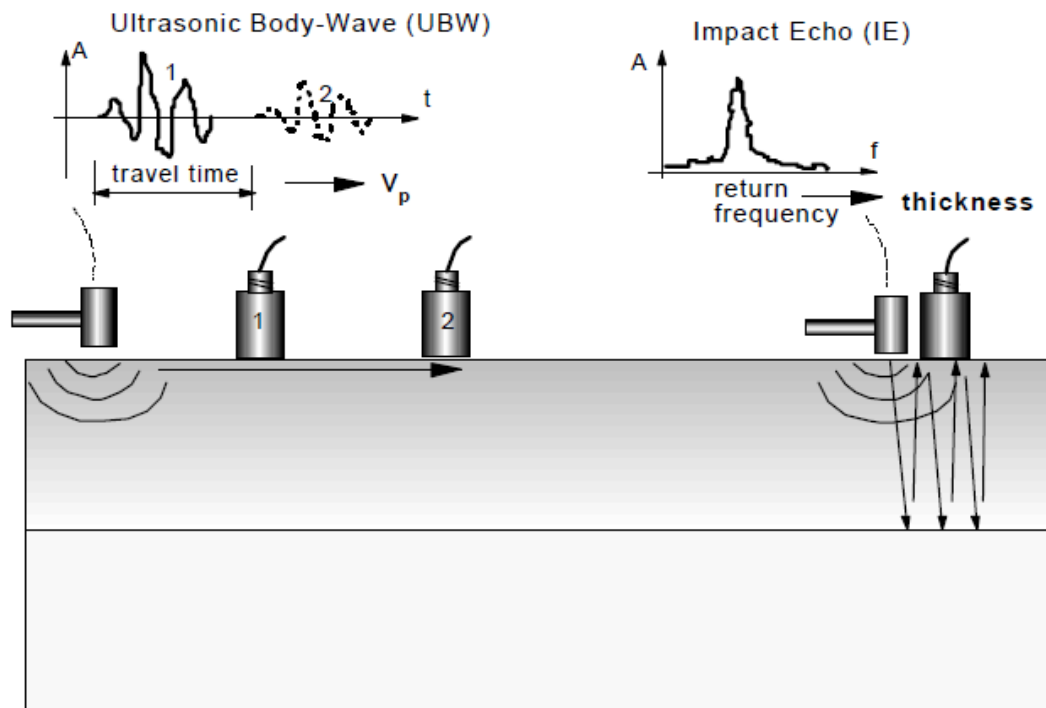


Figure (3- 5) Evaluation of the modulus of elasticity and the thickness of the overlay by UBW and IE methods ([Gucunski and Maher, 2002](#))

The resonant or return frequency is evaluated from a linear spectrum of a signal recorded. Once both the P-wave velocity and “return” frequency are known, an approximate thickness of the surface layer can be calculated using the following equation:

$$t = \frac{V_p}{2f_r} \quad (3.2)$$

where t is the thickness, V_{ph} is the P-wave velocity calculated from the UBW test, and f_r is the return frequency.

The previous three ultrasonic techniques (USW, UBW, and IE) were integrated in a device called Portable Seismic Property Analyzer (PSPA) ([Celaya et.al, 2009](#)). This device was developed as an extension of the Seismic Pavement Analyzer ([Nazarian et al., 1993](#); [Fernando et.al, 2001](#)). The device is widely used in evaluation of surface pavement layers and bridge decks. Generally, the PSPA system includes a sensor box, which contains a solenoid type impact hammer and two high frequency accelerometers, 7.5 and 21.5 cm away from the hammer ([Gucunski et al., 2008](#)). The latest PSPA design has all data acquisition and control elements as a part of the unit, as shown in Figure (3-6).

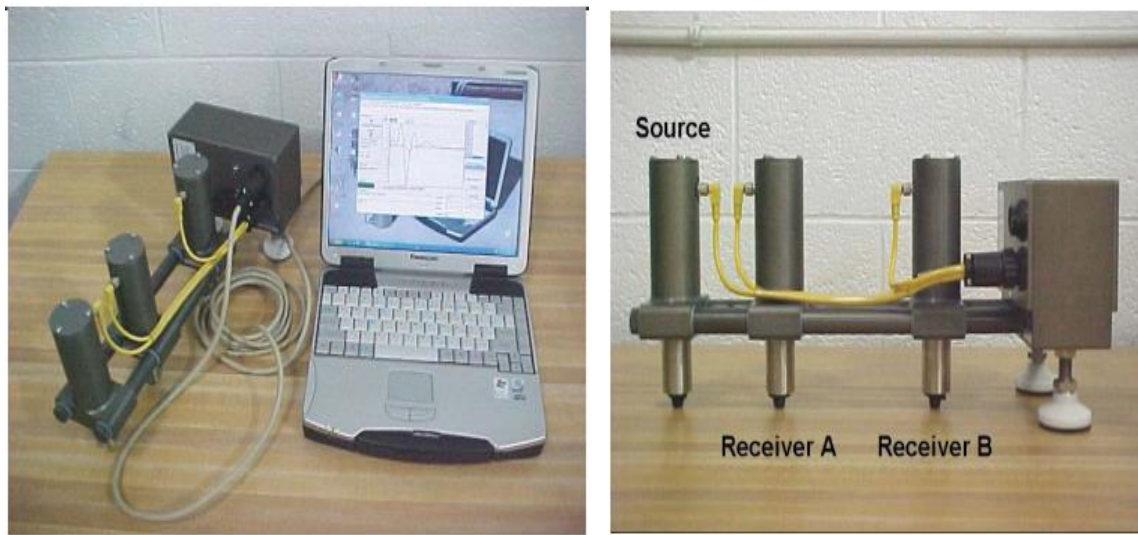


Figure (3- 6) Portable seismic pavement analyzer ([Celaya et al., 2009](#)).

Testing using the PSPA device was implemented during the experimental phase of this research, in which the elastic modulus of the surface layer of tested pavement sections was verified. The test results are presented in Chapter 6.

3-5 Spectral Analysis of Surface Waves (SASW)

The SASW method was first introduced by Heisey et al. (1982) and then further developed by other researchers at the University of Texas at Austin ([Nazarian et al., 1983](#); [Nazarian et al., 1987](#)). The main concept of this method is illustrated in Figure (3-7).

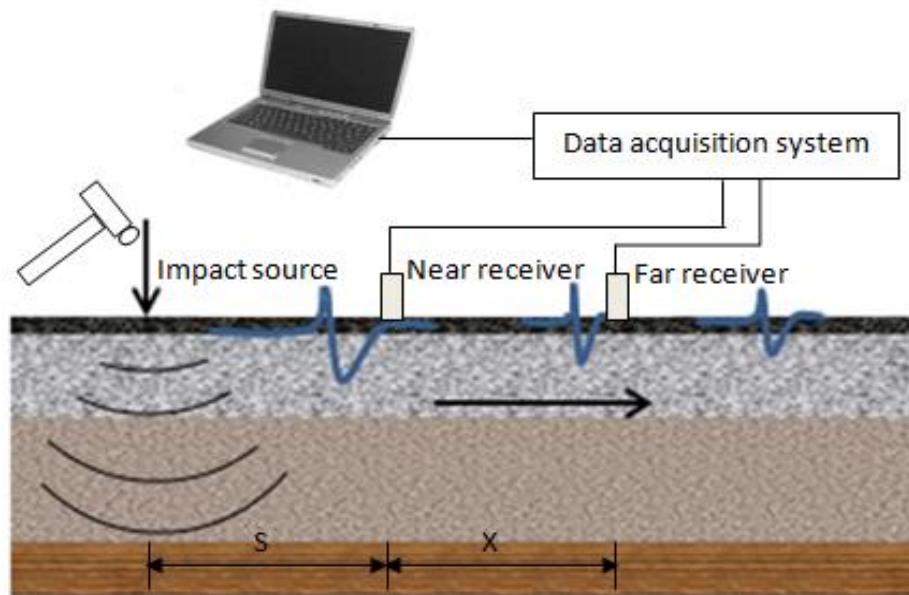
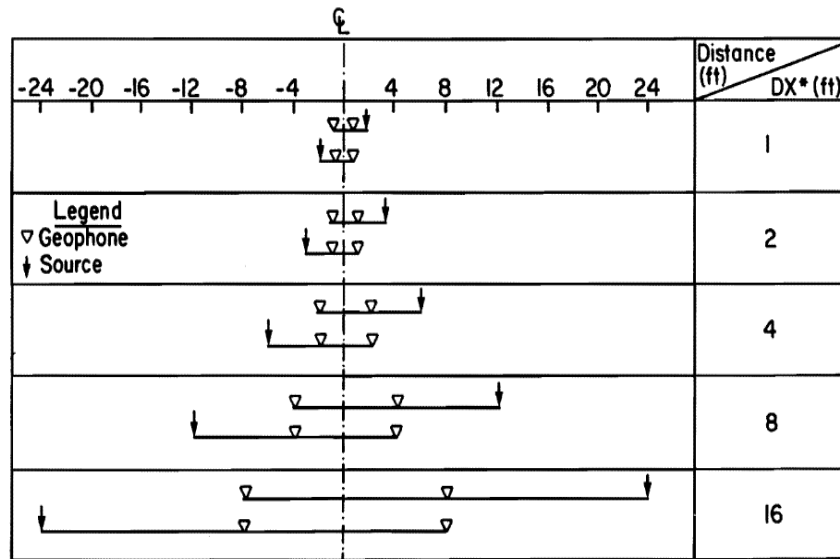


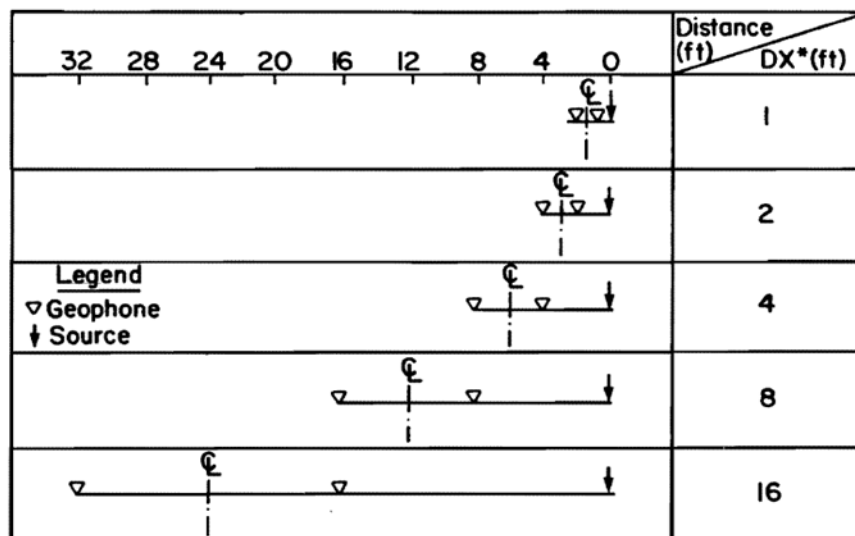
Figure (3- 7) Schematic of SASW test

The SASW method is used in evaluation of material properties of both pavement and soil sites. The method includes three stages. The first stage includes generation of surface seismic waves due to an applied impact load on the pavement surface. These seismic waves are detected by two or more receivers on the surface under different configurations ([Nazarian and Stokoe, 1986](#)). The receiver configurations include Common Receivers Midpoint Geometry (CRMP) and Common Source Geometry (CSR). In both configurations, the distance between the source and near receiver is equal to the

distance between two receivers. CSR is commonly used in pavement evaluation; the schematics of the two geometries are shown in Figure (3-8).



(a)



(b)

Figure (3- 8) SASW receiver configurations (a) CRMP (b) CSR ([Nazarian and Stokoe, 1985](#))

The second stage of the SASW test includes determining of the experimental dispersion curve, which represents the relationship between the wavelength and phase

velocity (apparent Raleigh wave velocity) by following a dispersion curve evaluation process ([Nazarian and Stokoe, 1986](#)). Finally, the third stage is the inversion of the experimental dispersion curve to obtain the shear wave velocity, or shear modulus profile. More details about the dispersion curve evaluation and inversion processes are provided in the next sections.

A later, more advanced version of the SASW test is Multi-Channel Analysis of Surface Waves (MASW) method. This method was first reported in the late 1990s ([Xia, Miller and Park, 1998](#)). It has a similar analysis procedure as the SASW test, but the number of receivers is significantly higher (arrays of 12-48 sensors), which enables detection or identification of different surface wave modes. The disadvantage of the MASW method for pavement evaluation stems from a slower sensor array deployment and, as a result, higher cost. Figure (3-9) presents an example of MASW time histories and analysis results for an asphalt pavement ([Ryden et al, 2004](#)).

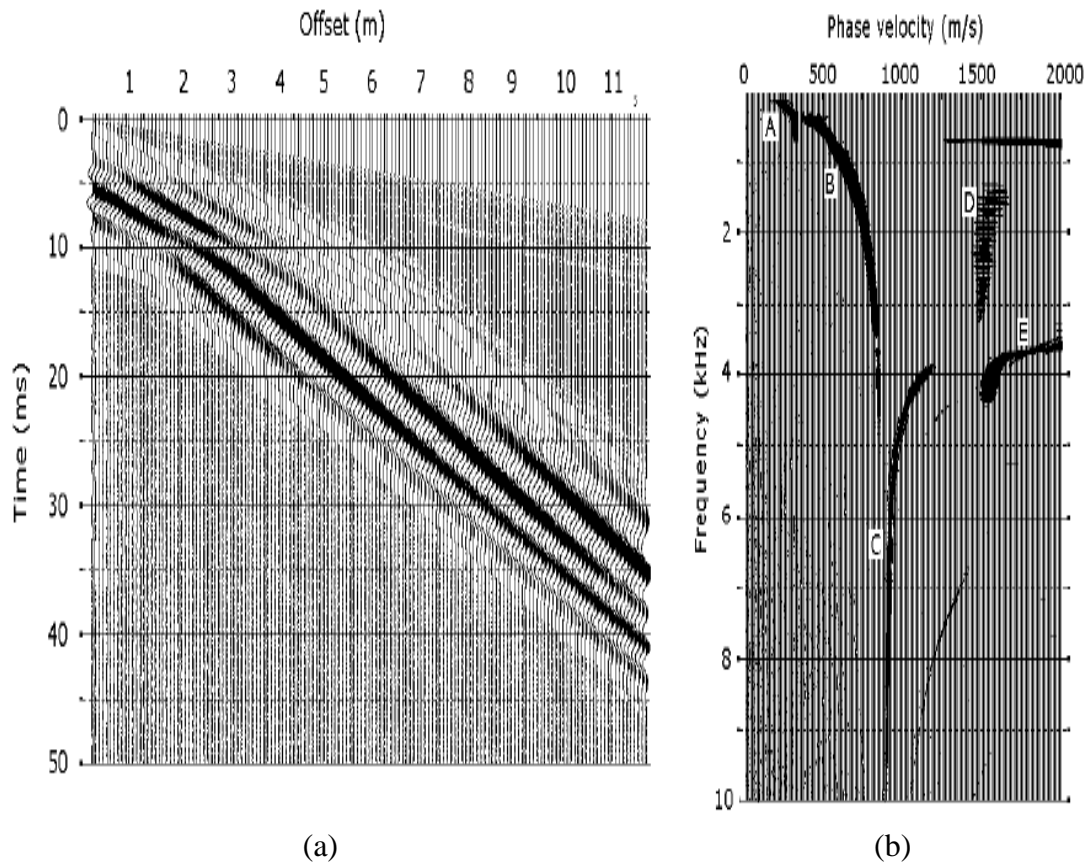


Figure (3- 9) (a) Multi-channel records and (b) MASW analysis results for an asphalt pavement ([Ryden et al, 2004](#))

3-6 Non-Contact NDT

In order to accelerate NDT techniques, efforts have focused on the usage of non-contact techniques since early 1970's (Castings and Hosten, 2001). One of the ways how to conduct non-contact or air-coupled testing is using optical detection with a laser. In this case waves propagating in a solid are detected by providing a sensitive measurement of motion at a point on the surface of a tested object ([Zhu and Popovics, 2002](#)). Another non-contact approach stems from the use of microphones. Air-coupled sensing using

microphones has been used widely to accelerate different NDT methods, such as SASW testing ([Kee, 2011](#)), MASW testing ([Ryden et. al., 2009](#)) and IE testing ([Zhu and Popovics, 2008](#)). The fundamental concept of non-contact or air-coupled sensing is based on detection of radiation of surface waves (leaky Rayleigh waves), or other waves, generated from the vibration of surface particles during wave propagation.

3-6-1 Air-Coupled SASW

The air-coupled SASW represents modification of the conventional SASW method, where surface waves, instead of being detected by ground-coupled sensors, are detected by non-contact sensors (i.e. microphones). The typical test configuration is shown in Figure (3-10). Clearly, eliminating the need to couple the sensors will accelerate the data collection process ([Zhu and Popovics, 2004](#); [Lu et.al., 2015](#)) .

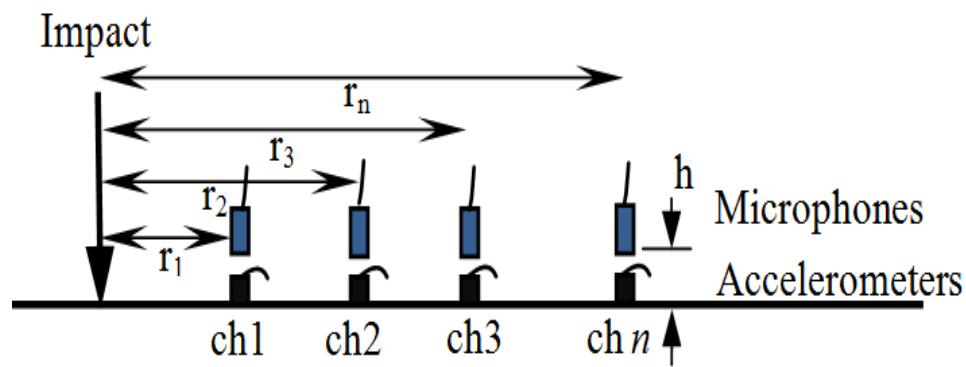


Figure (3- 10) Schematic of contact and non-contact SASW test ([Lu et.al., 2015](#))

During the SASW test, a vertical impact point load is applied on the surface (refer to section 3.3). The impact will generate body waves, P- and S-waves, and surface waves (Rayleigh waves). The propagating surface waves will cause ground vibrations, so that each surface particle will become an acoustic source that will radiate acoustic waves in the air, called leaky surface waves. These waves contain the same information about the surface wave propagation, including dispersion, as the ground surface waves. Figure (3-11) illustrates the direct acoustic, and surface and leaky surface waves.

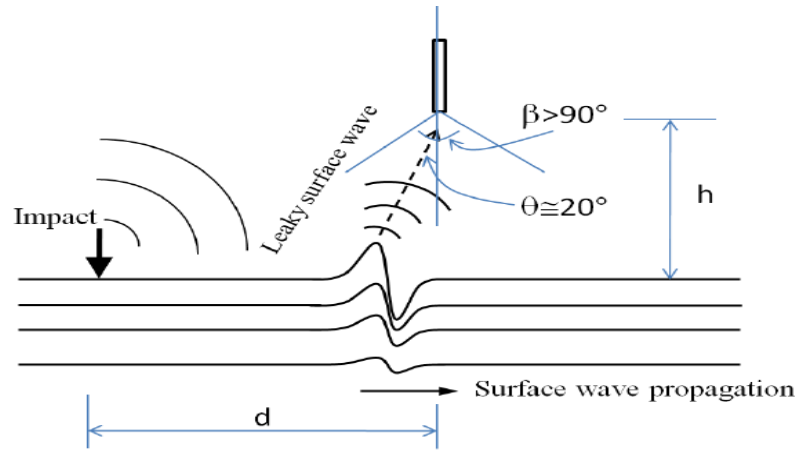


Figure (3- 11) The direct and leaky surface waves ([Lu et al., 2015](#))

By applying the Snell's laws, the leaky angle (θ) shown in the previous Figure (3-10) is calculated by applying Equation (3.3)

$$\sin(\theta) = \frac{C_{air}}{C_{LR}} \quad (3.3)$$

where: C_{air} is the air velocity (about 340 m/s) and C_{LR} is the surface wave (Rayleigh wave) velocity. The air-coupled sensors will detect both the direct acoustic and radiation (leaky) surface waves. To eliminate the direct acoustic waves and extract the leaky

surface waves, an appropriate time window has to be applied. This is done by calculating the expected arrival times for leaky surface and direct acoustic waves using Equation (3.4) and (3.5) ([Zhu and Popovics, 2008](#)):

$$t_{LR} = \frac{r}{c_{LR}} + \sqrt{\frac{1}{c_{air}^2} + \frac{1}{c_{LR}^2}} \quad (3.4)$$

$$t_{air} = \frac{\sqrt{r^2 + h^2}}{c_{air}} \quad (3.5)$$

where t_{LR} and t_{air} are the expected arrival times for leaky surface and direct acoustic waves, respectively.

Atypical height of the air-coupled sensors has to be enough to avoid placement of the sensors within a zone known as 'shadow' or 'blind zone'. The shadow zone is defined as a space nearby the air-coupled sensor region, and has a size equal to $(h \tan(\theta))$, where θ is the received angle of the leaky surface wave as shown in Figure (3-12) ([Zhu and Popovics, 2008](#)). In this zone no leaky surface waves can be detected.

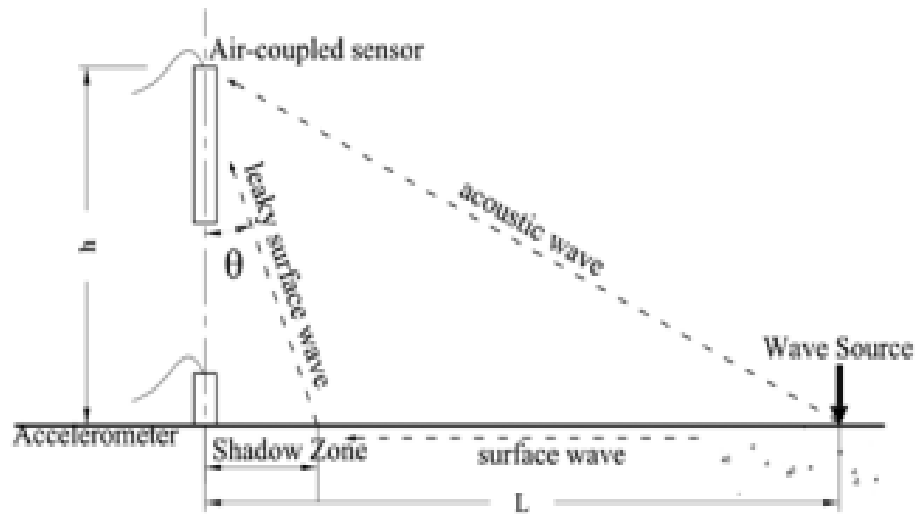


Figure (3-12) Shadow zone location ([Zhu and Popovics, 2008](#))

Minimizing the sensor height from the surface will reduce this zone. Therefore, the larger the distance between the source and the air-coupled sensor, and the lower the height of the sensor during the test will reduce the undesirable effects of the acoustic waves and the shadow zone; respectively ([Zhu and Popovics, 2008](#)). Those elements were considered in this research while implementing the tests in the field, as discussed in Chapter 6.

3-7 Dispersion Curve Calculation

The dispersion curve calculation steps, which are called the "dispersion process", include several steps. The first step is transferring the time histories for each detected signal from the time-domain to the frequency-domain by applying the Fast Fourier Transform (FFT). Then, the phase relationships between two signals, which may have been caused by time delays, propagation delays, or varying wave paths between receivers, are determined by using the phase of the cross power spectrum function ([Heisey et.al, 1982](#)). The cross power spectrum can be defined as a Fourier transform of the cross-correlation function between two different signals $x(t)$ and $y(t)$, as illustrated in Equation (3.6) ([Nazarian and Desai, 1993](#)).

$$S_{r1,r2}(f) = \frac{1}{n} \sum_{i=1}^n \{ [R_1(f)]_i \cdot [R_2^*(f)]_i \} \quad (3.6)$$

where: $R_1(f)$ and $R_2(f)$ are the Fourier transforms of time records from two receivers located a distance D apart; $S_{r1,r2}(f)$ is the frequency-domain average of several records; $R_2^*(f)$ is the complex conjugate of the second signal.

Only the signals of good quality can be used in the dispersion curve calculation. The signal quality is determined by calculating the coherence function. It can be defined as a statistical measurement of quality of correlation between two signals. In other words, it indicates how well the first signal x corresponds to the second signal y at each specified frequency. Equation (3.7) defines the coherence function ([Nazarian and Desai, 1993](#)):

$$\gamma^2(f) = \frac{|S_{r1,r2}(f)|^2}{A_{r1}(f) \cdot A_{r2}(f)} \quad (3.7)$$

where: $A_{r1}(f)$ and $A_{r2}(f)$ correspond to the averaged auto power spectra of multiple records from receiver 1 and receiver 2, respectively. More details are provided in Chapter 6. The wrapped phase represents the phase of the cross-power spectrum. The wrapped phase is defined as the phase difference between two signals, and it is ranging from -180 to +180. The unwrapped phase is obtained from the wrapped phase by adding $360 \cdot n$, where n is a positive integer including zero ([Heisey et.al, 1982](#)). Figure (3-13) provides an example of wrapped and unwrapped phase plots.

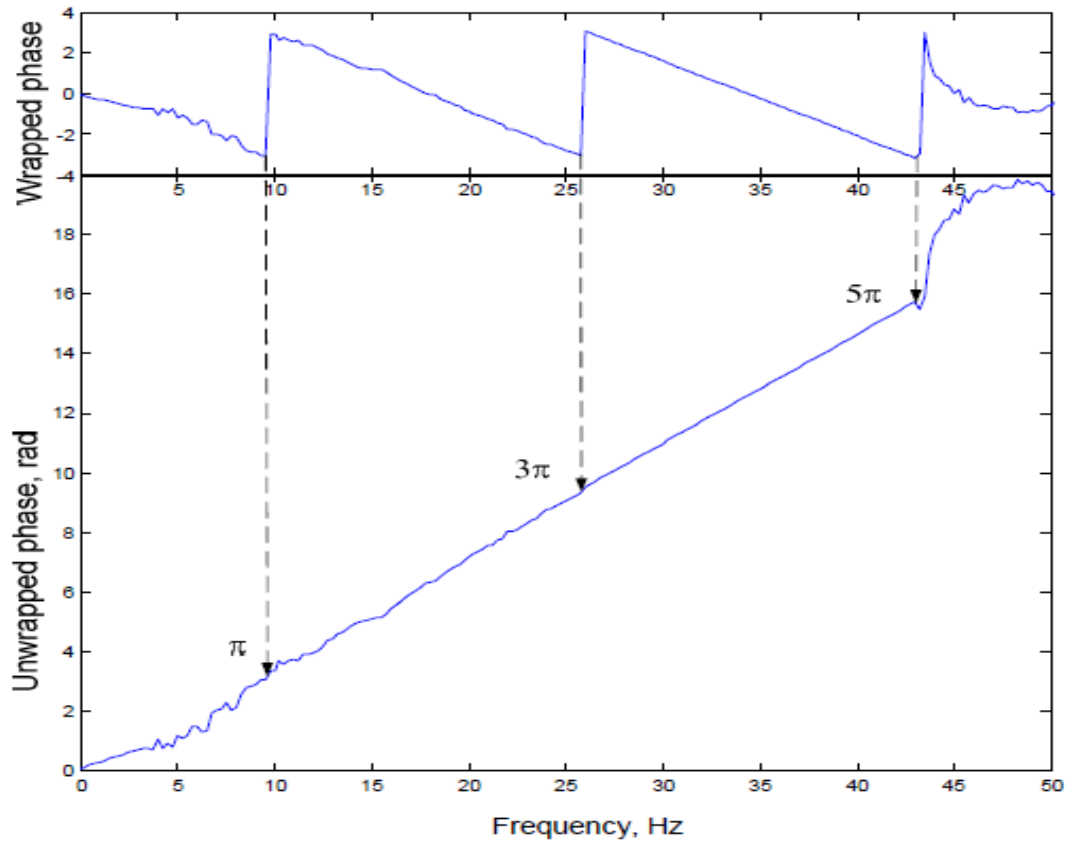


Figure (3-13) Wrapped and unwrapped phase example

The surface wave (phase) velocity (V_{ph}) and the wavelength (λ) are then calculated using Equations (3.8 - 3.11) to determine the dispersion curve:

$$\Phi(f) = \tan^{-1} \frac{\text{Imag}[S_{r1,r2}(f)]}{\text{Real}[S_{r1,r2}(f)]} \quad (3.8)$$

$$t(f) = \frac{\Phi(f)}{360f} \quad (3.9)$$

$$V_{ph}(f) = \frac{D}{t(f)} \quad (3.10)$$

$$\lambda(f) = \frac{V_{ph}(f)}{f} \quad (3.11)$$

Where Φ is phase difference in degrees for a given frequency, $t(f)$ travel time for a surface wave to travel between two receivers for a given frequency, and D is the distance between the two receivers.

By repeating the procedure defined by Equations (3.8) through (3.11) for every frequency, the surface wave velocity corresponding to each wavelength is evaluated and the dispersion curve is determined.

In this study, the dispersion curves were calculated using time histories for acceleration and air-pressure extracted from a database developed using numerical simulations of SASW test for contact and air-coupled sensors, respectively. The numerical simulation, as in the actual SASW testing, considers the fact that the dispersion curve is a result of the overall wave propagation (i.e. it represents a superposition of both body and surface waves of a number of modes). The detailed description of the finite element parameters that were considered in building the numerical models in this research can be found in the next chapter.

The code for dispersion analysis was prepared in MATLAB software. The developed code includes all previously described dispersion calculation steps, as well as the average dispersion curve calculation, as described by [Nazarian and Stokoe](#) (1983). The average dispersion curve represents an average of dispersion curves obtained for several receiver spacings. Each dispersion curve is filtered using a specific filtering criterion. The available filtering criteria are discussed in the next section. Four different receiver spacings of 0.1, 0.2, 0.4 and 0.8 m were considered for both simulated accelerometer and air-coupled (microphone) sensors. In all cases, the source to near

receiver spacing was kept equal to the receiver spacing. Figure (3-14) provides an example of acceleration time histories for different receiver locations/positions.

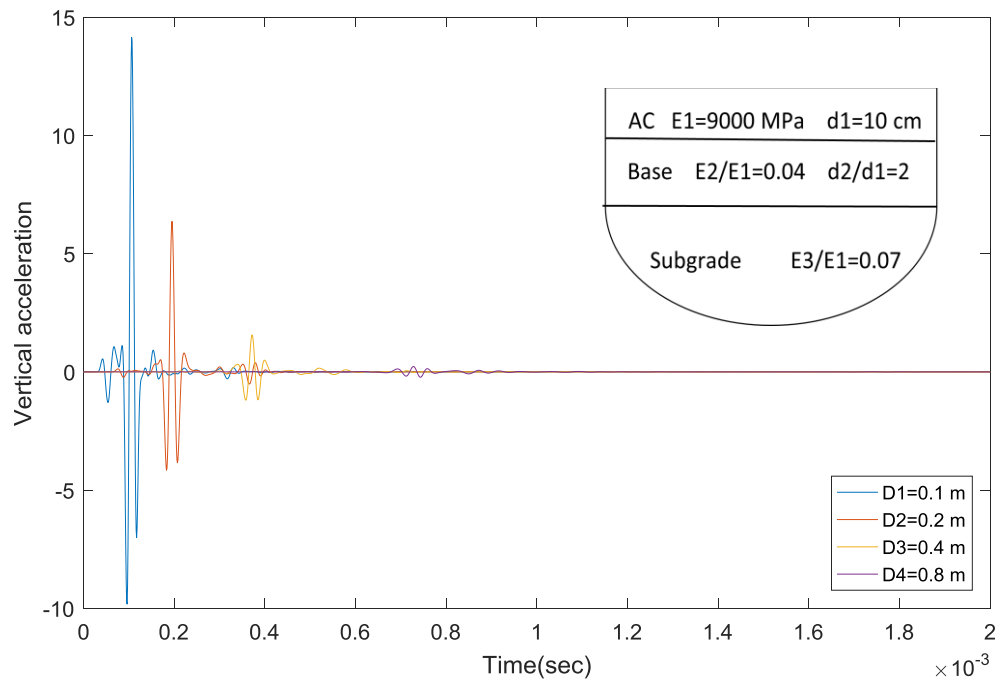


Figure (3- 14) Acceleration time histories from a FEM model for different receiver locations

Figure (3-15) provides the phase angle of a cross-power spectrum. The corresponding filtered dispersion curves, described in terms of phase velocity vs. wavelength, and phase velocity vs. frequency, are shown in Figure (3-16).

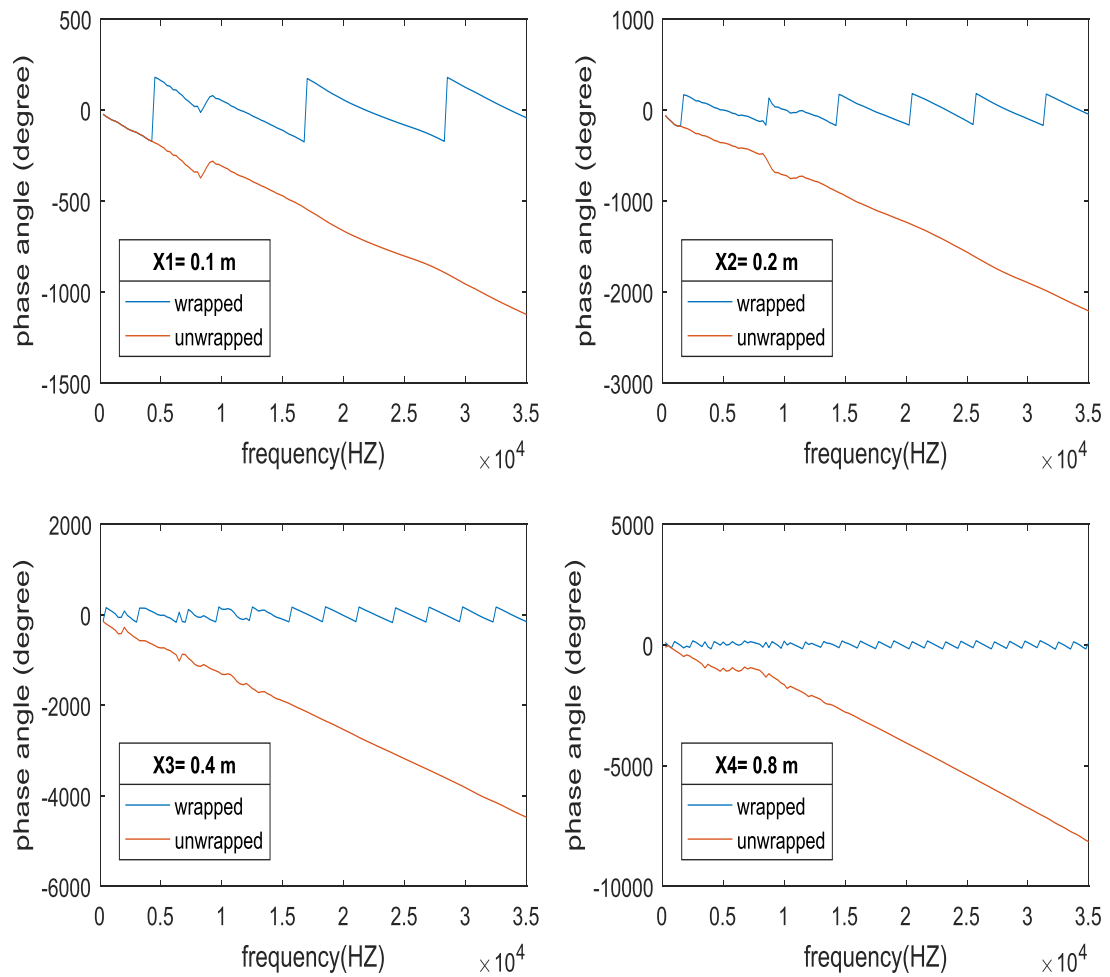
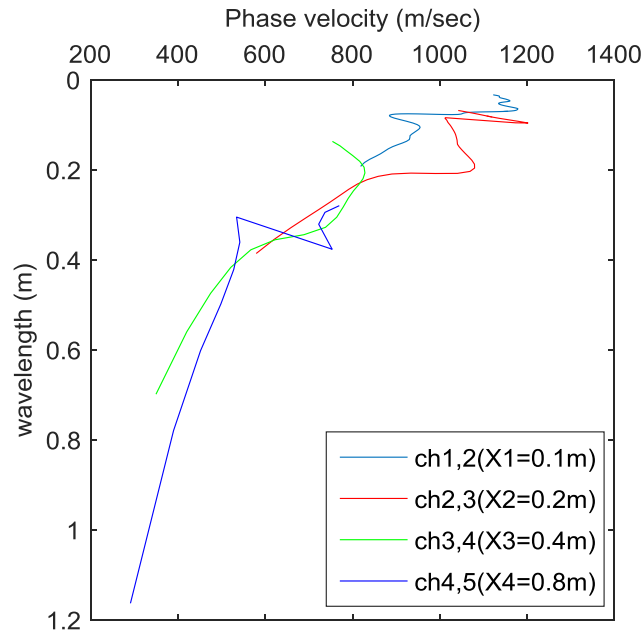
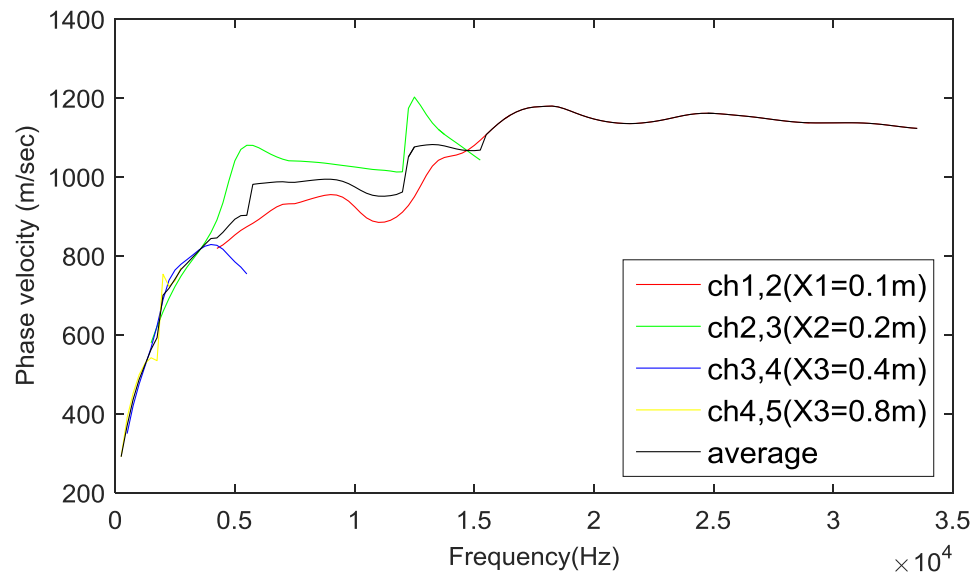


Figure (3- 15) Phase angle of cross-power spectra for four accelerometer spacings



(a)



(b)

Figure (3- 16) Filtered dispersion curves based on acceleration time histories: (a) phase velocity vs. wavelength, and (b) phase velocity vs. frequency.

In the final step, the average dispersion curve was normalized with respect to the surface layer shear wave velocity, as shown in Figure (3-17). The normalization process will be discussed later in Chapter 6. The normalized average dispersion curve will be used in the next step, the inversion process, to obtain the pavement modulus profile.

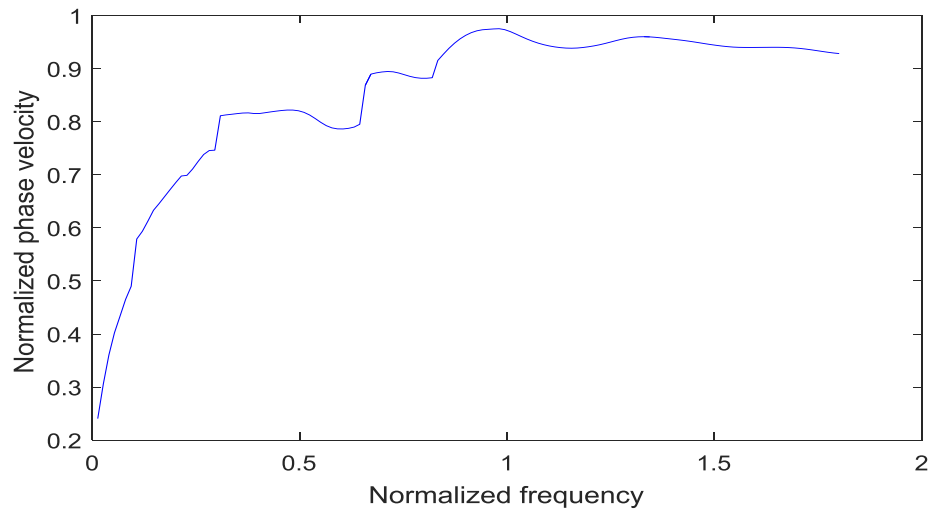


Figure (3- 17) Normalized average dispersion curve

The same processing steps were applied to the time histories for the simulated air-pressure (microphone) sensors, but with one extra step. The extra step included the application of an appropriate time window to eliminate the direct acoustic waves and to extract the leaky surface waves, as discussed previously in Chapter 3. Figure (3-18) provides an example of the windowed air-pressure history at a location 0.1 m away from the impact source, and 3 cm above the pavement surface.

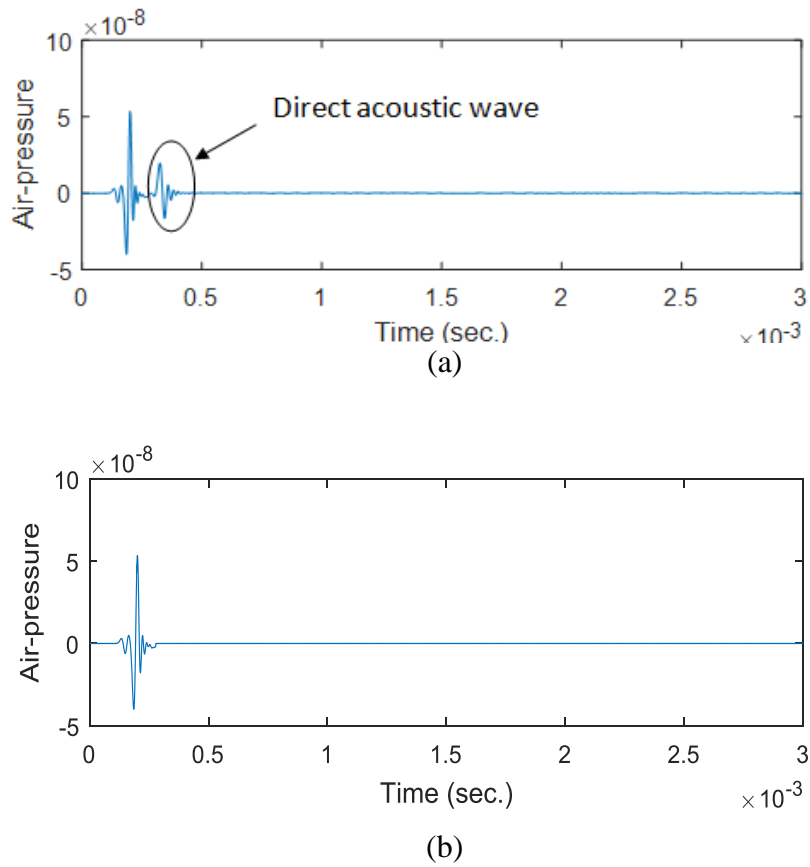


Figure (3- 18) Air-coupled sensor records: (a) raw, and (b) windowed data.

Figure (3-19) illustrates the time histories of air-pressure at receivers positioned at different distances from the impact source and 3cm above the pavement surface. The corresponding dispersion analysis results are shown in Figures (3-20 and 3-21).

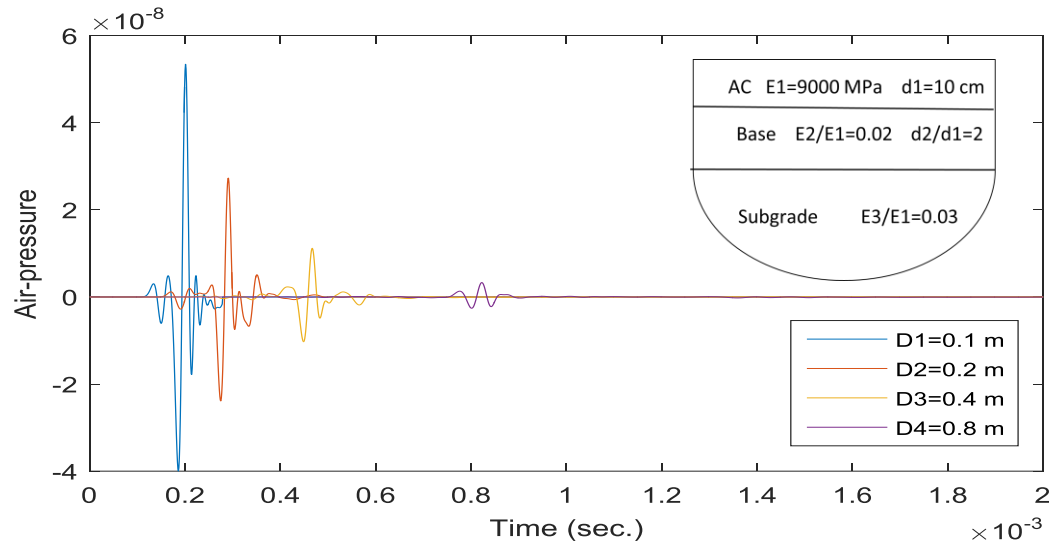


Figure (3- 19) Windowed air-pressure time histories for four receiver locations

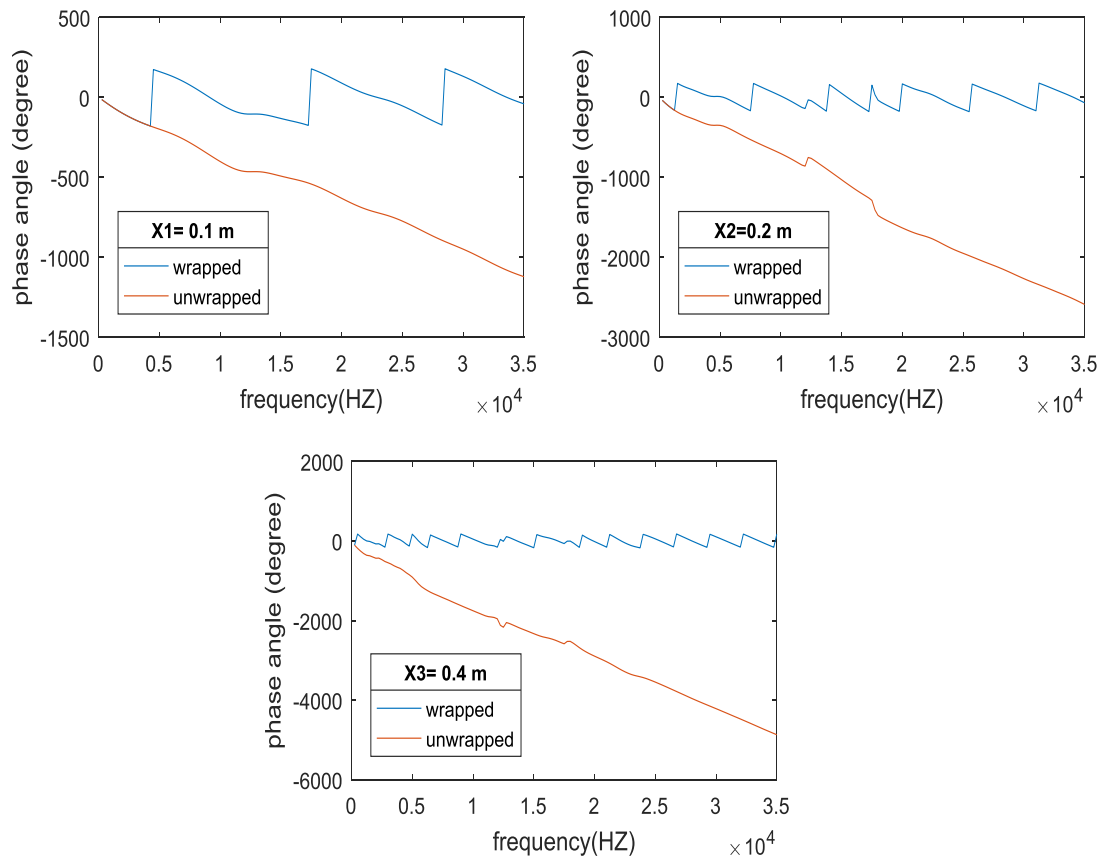
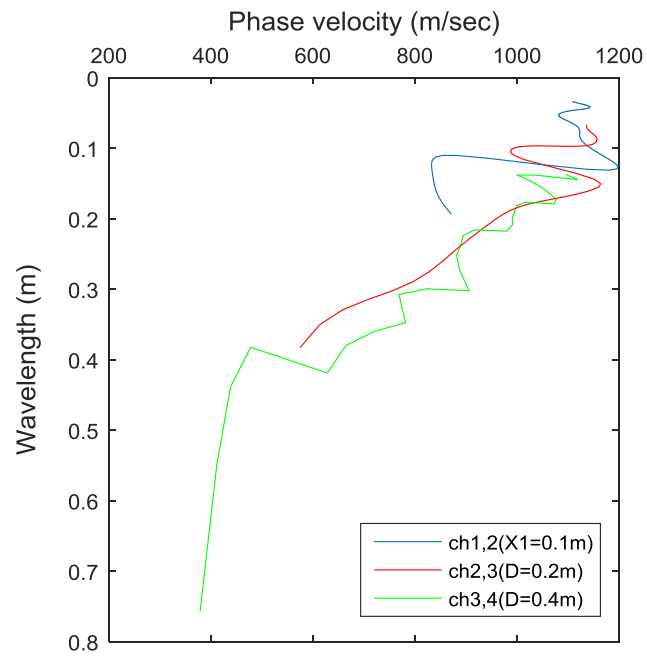
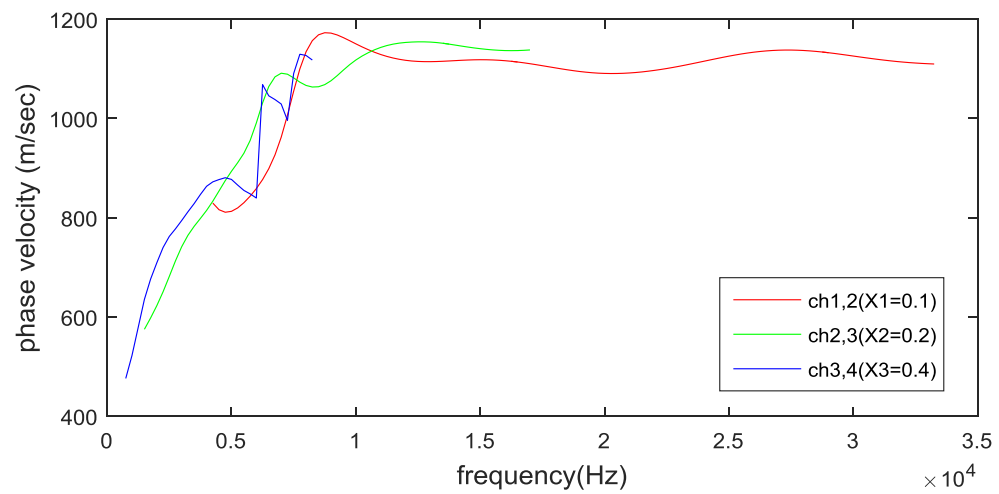


Figure (3- 20) Phase of cross-power spectrum for three air-coupled spacings



(a)



(b)

Figure (3- 21) Filtered dispersion curves based on air-pressure time histories: (a) phase velocity vs. wavelength, and (b) phase velocity vs. frequency.

A comparison of the dispersion curves for acceleration and air-pressure sensors for the same synthetic pavement profile is shown in Figure (3-22). The comparison also illustrates a typical level of agreement between results from the two sensors types, which is generally high. The level of agreement between two sensor approaches is also illustrated by the results for another synthetic pavement profile in Figure (3-23). As can be observed, there is high agreement in the high frequency range, while there is significant disagreement in the lower frequency range. The disagreement is attributed to the lower shear wave velocity of base and subgrade layers, reaching the speed of acoustic waves in the air. Therefore, it is recommended to isolate receivers from the direct acoustic waves, especially those farther away from the source. In that case, the air-coupled sensors will detect the leaky surface waves, while the effect of the direct acoustic waves will be reduced.

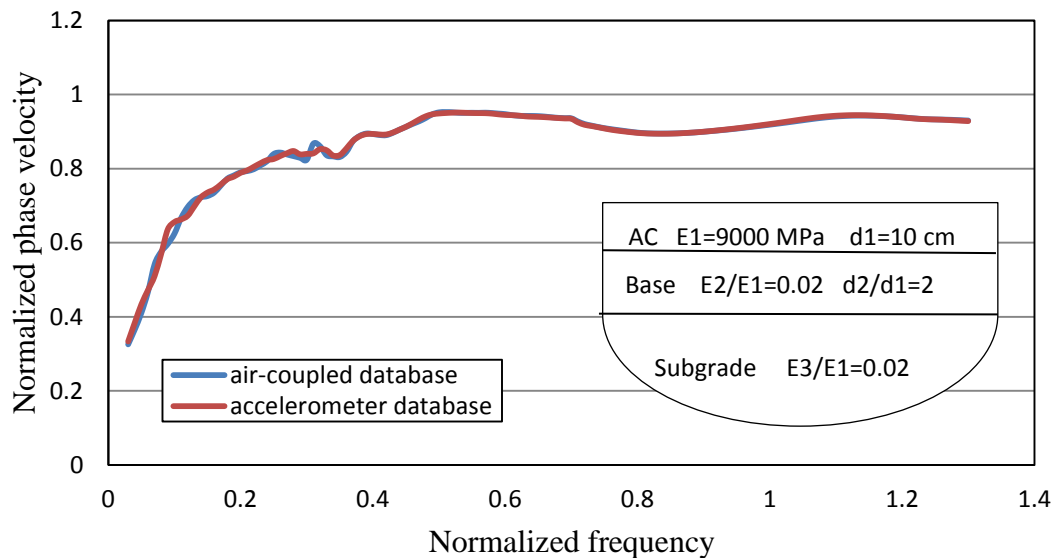


Figure (3- 22) Comparison between the dispersion curves for acceleration and air-pressure sensors (example1)

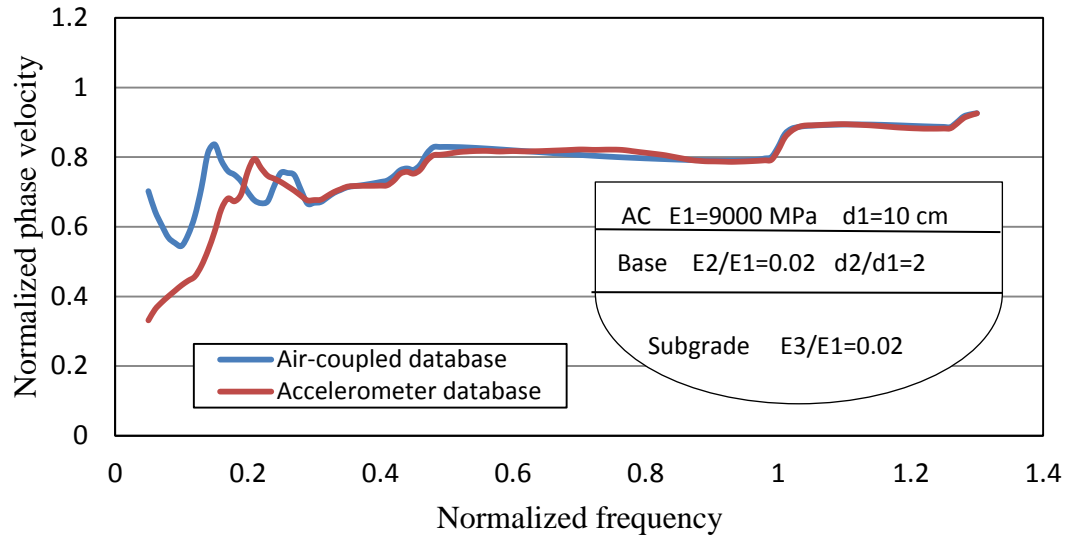


Figure (3- 23) Comparison between the dispersion curves for acceleration and air-pressure sensors (example2)

3-8 Filtering Criteria

There are two filtering criteria, with respect to the surface wavelengths, applied in the filtering of dispersion curves to ensure that these curves truly represent the dispersion characteristics of the tested profile. These criteria are a function of receiver spacing, x , which is affected by many factors: velocity of material to be tested, depth of investigation, range of frequency, attenuation properties of the structure, and sensitivity of the instrumentation to measure the phase difference between signals ([Heisey, 1981](#); [Nazarian, 1984](#)). Based on several previous studies, different filtering criteria were recommended, as shown in Table (3-1).

Table (3-1) Recommended filtering criteria ([Ganji and Gucunski, 1998](#)).

Reference	(d ₁) criteria	(D) criteria
Lysmer (1966)	$2.5\lambda < d_1$	-
Heisey et al. (1982)	$d_1 = D$	$0.3333\lambda < D < 2\lambda$
Sanchez-Salinerio et al. (1987)	$d_1 = D$	$2\lambda < D$
Roeset et al. (1989)	$0.5\lambda < d_1 < 2\lambda$	$0.5d_1 < D < d_1$
Gucunski and Woods (1992)	-	$0.5\lambda < D < 4\lambda$
Tokimatsu et al. (1991)	$0.25\lambda < d_1 + (D/2)$	$0.0625\lambda < D < \lambda$

*d₁ is the distance between the impact load and first receiver, and D is the spacing between two receivers.

Practically, it is more convenient to test with various distances between the receivers in the field, and then evaluate the range of wavelengths over which reliable measurements were made for a particular spacing ([Heisey et al., 1981](#)). The minimum receiver spacing should be sufficient to generate the surface waves between two receivers, while the maximum receiver spacing imposed to avoid excessive attenuation of the response between two receivers ([Gucunski et. al, 1996](#)).

Since the synthetic dispersion curves are obtained using the same steps as those in an actual SASW test, filtering criteria have to be applied. A new filtering criterion for dispersion curves obtained from air-pressure sensing was investigated. It was defined after many trials and errors by applying different receiver spacing with kept the distance between the near receiver and the applied source fixed. The results have shown that the minimum acceptable wavelength that can give reliable results, and eliminate the scattering points on the dispersion curves, should be greater than a third of the receiver spacing to reduce the effect of body waves. In contrast, the maximum acceptable wavelength should be less than the double receiver spacing to provide the required wavelength to investigate the desired depth, Figure (3-24) provides an example for applying the investigated filtering criteria on dispersion curves based on air pressure time

histories. The proposed air-coupled sensor filtering criteria is given in the following equation:

$$x/3 \leq \lambda \leq 2x \quad (3.12)$$

where x is the receiver spacing and λ is the wavelength.

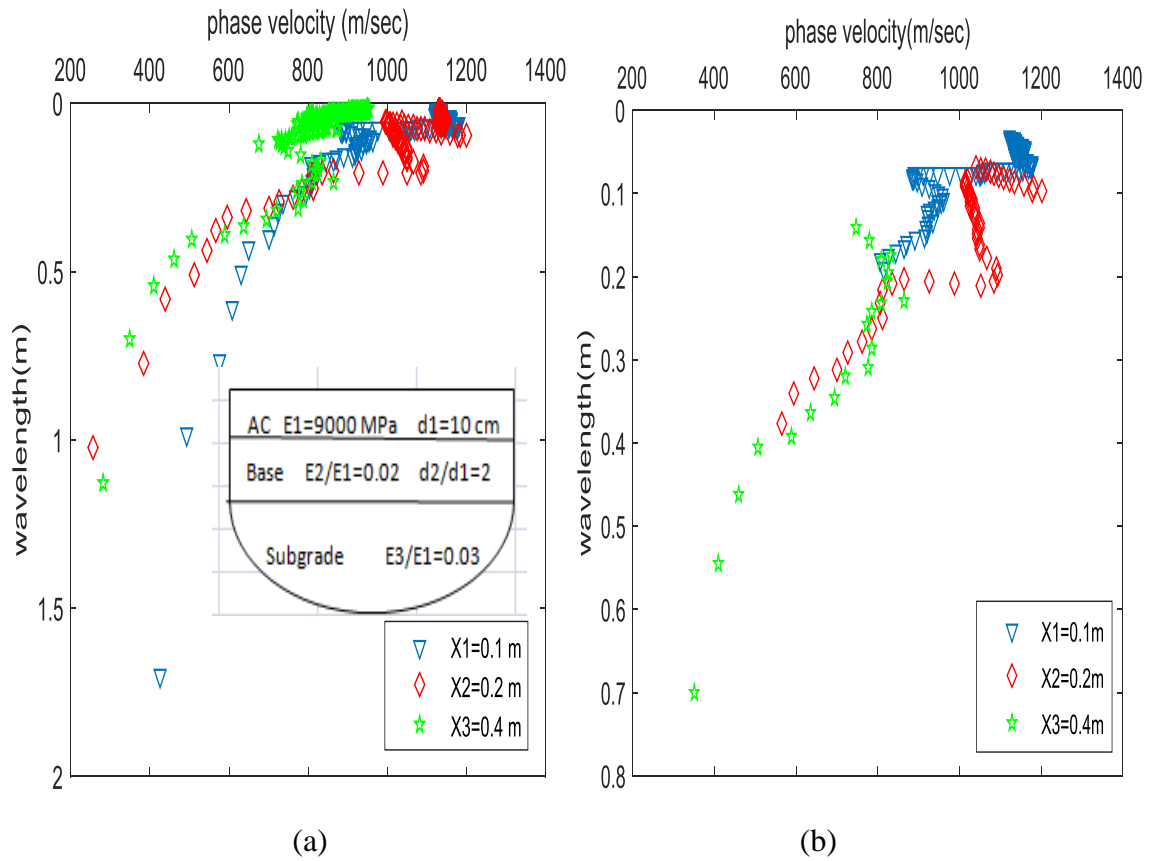


Figure (3- 24) Dispersion curves based on air pressure time histories (a) before, and (b) after filtering

3-9 Inversion Methods

Different inversion methods are used in solving the nonlinear inverse problem of the SASW test. These methods can be categorized into two groups: empirical and theoretical inversion methods ([Tarantola, 1987](#); [Menke, 1989](#)). The empirical inversion methods, also called 'wavelength' methods, are considered the simplest way to extract the shear wave velocity profile from the dispersion curve. This method depends on scaling of the dispersion curve, where the phase velocity is multiplied by a factor of 1.1 to obtain the shear wave velocity, while the depth is obtained by factoring the wavelength axis by one-third ([Tokimatsu, 1997](#)). This method fits well on continuously inhomogeneous soil profiles with gradually increasing velocity with depth, which is called a normally dispersive profile.

In contrast, the theoretical inversion method includes two approaches: local and global search procedures. In general, local search procedures are iterative procedures that start at some estimate of the model parameters, and with regression methods minimize the error the initial guess. Otherwise, the global search procedures attempt to search over the entire solution space to find the global minimum for the error function. More details can be found in these references ([Tarantola, 1987](#); [Menke, 1989](#); [Tarantola, 1987](#); [Orozco, 2003](#)).

All previous inversion procedures are considered time consuming, since they depend on trial and error procedure to find the correct profile. Therefore, many studies have been focused on finding an inversion alternative to accelerate its process ([Gucunski and Wood, 1992](#); [Yuan and Nazarian, 1993](#); [Ganji et.al, 1997](#)). One of these inversion alternatives is by using Artificial Neural Networks (ANNs), which have been used

successfully in a wide range of engineering applications. ANNs have proven that they can accelerate the inversion process, including for surface wave testing of pavement systems. However, in the case of pavement systems, the modulus predictions from ANNs for the base layer were weak ([Nazarian et.al, 2004](#)), and further improvements of ANNs are needed. More details about the ANNs based inversion method are provided in Chapter 5.

CHAPTER FOUR

Numerical Simulation of Air-Coupled SASW Test by FEA

4-1 Introduction

Numerical simulation is considered to be an important research tool, especially in those cases that are difficult to examine experimentally, such as when it is needed to investigate under many different testing conditions. Therefore, the numerical analysis will be a cost and time effective alternative. In the pavement analysis, the numerical simulation is widely applied. In particular, there is no analytical solution for the Rayleigh-Lamb equation (i.e. interaction of propagating waves within a flexible pavement). Therefore, the solutions are sought by applying the stiffness matrix method or performing a finite-element analysis (FEA) for numerical estimation ([Sansalone, 1987](#)).

In this study, Finite Element Analysis (FEA), also called the Finite Element Method (FEM), was used to simulate the spectral analysis of surface waves conducted on the synthetic pavement profiles. In general, the FEA is a numerical procedure for obtaining an approximate solution for a physical problem. The continuum is first divided into a finite number of discrete parts-finite parts; representing a finite-element model (mesh). A variety of stress or displacement distributions within each element of the model (mesh) is described by an assumed set of functions called shape functions. In contrast, force-displacement equations are formulated using energy principles. All these previous elemental equations are then combined to construct global equations, which describe the behavior of the entire model. An approximate displacement or stress at any

point (node) within the model is obtained by solving these global equations ([Cook R. D., 2002](#); [Sansalone et.al, 1987](#)).

Since the finite element analysis gives approximate results, compared to the exact solution, it is very important to assess the accuracy of numerical solutions by performing a preliminary FEA on a simple model, and to compare its results to the existing analytical or experimental results. Based on that comparison, the numerical model can be enhanced, for example by decreasing the element size to achieve the sufficient level of accuracy. When the FEA is applied to obtain the solution of a dynamic problem involving wave propagation, many analytical parameters will have to be selected very carefully ([Sansalone M. C., 1987](#); [Sansalone et.al, 1987](#); [Ganji et.al, 1997](#); [Bathe, 1996](#); [Zerwer, 2002](#)). Some of these parameters include the element size, time step, the overall dimensions, and many more other parameters that will be discussed in more details in the following sections.

This study includes numerical simulation of the spectral analysis of surface waves (SASW) test using commercially available ABAQUS Standard, CAE and Explicit ([ABAQUS, 2016](#)). The Explicit scheme, which is also known as the forward Euler or central difference algorithm, was adopted in the analysis, because it is suitable for high-speed dynamic events, such as stress wave propagation in elastic media. In order to evaluate the pavement profile and generating a database of dispersion curves that will be used in the development of artificial neural networks models to estimate the shear wave velocity profile, a number of two-dimensional (2D) finite-element axisymmetric models representing hypothetical pavement profiles were generated. Those were generated, instead of three-dimensional (3D) models to save computing time, since a huge number

of flexible pavement profiles were investigated. Moreover, the 2D finite-element model provides a sufficiently accurate way to investigate wave propagation in in-plane cases ([Sansalone et.al, 1987](#)).

This chapter includes a detailed description of the finite element parameters considered in building the numerical models in this research.

4-2 FE Model Description

A large number of synthetic pavement profiles were generated using a finite element program ABAQUS to simulate the SASW test on a pavement system. The FE model used in simulation of the SASW test is described as a 2D axisymmetric problem, with infinite elements on the sides and the bottom. A fixed impact source was defined at the surface of the FE model. Two pavement system cases were considered. In the first case, a three layer pavement system consisted of a single course surface layer, a base layer and a subgrade. In the second case, a four layer pavement system was considered, consisting of a two-course surface layer, and base and subgrade layers. For the two cases, the subgrade layer was considered to be a half-space. Two adjacent layers were assumed to be perfectly bonded. Moreover, air layer was added above the surface layer. The air layer represented a fluid layer to enable simulation of non-contact (air-coupled) SASW testing, as shown in Figure (4-1).

For each of these two cases, a large number of pavement profiles were modeled using three types of finite elements provided in ABAQUS. Four-node axisymmetric elements (CAX4R) were selected for modeling the pavement layers. Four-node linear

reduced integration with hourglass control (ACAX4R) acoustic elements were selected to model the air layer. Finally, 4-node linear, axisymmetric one-way infinite elements (CINAX4) were assigned at the model boundary, at the far edge of the solid zone, to simulate an infinite energy-absorbing boundary (also referred to as silent boundaries). In order to connect the fluid (air) and solid half space (pavement) surfaces, the contact pair (e.g. the master and slave surfaces) have to be defined in ABAQUS/Standard. Generally, a more rigid surface between two contact surfaces is defined as the master surface. Therefore, in this study the non-deformable pavement surface is defined as the master surface, while the air is defined as a slave surface. There are two approaches that one may follow to model the pair connection: node-to-surface or surface-to-surface connection. For a given mesh refinement, the surface-to-surface approach tends to provide more accurate stresses ([Wang, 2011](#); [ABAQUS, 2017](#)). The two approaches were examined, and it was found that the surface-to-surface approach produces more effective connection between the two surfaces, and without impeding the surface wave propagation.

The factors that affected the accuracy of the FE analysis, including the overall dimensions of the model, the element size, time step, and others are discussed later in the chapter.

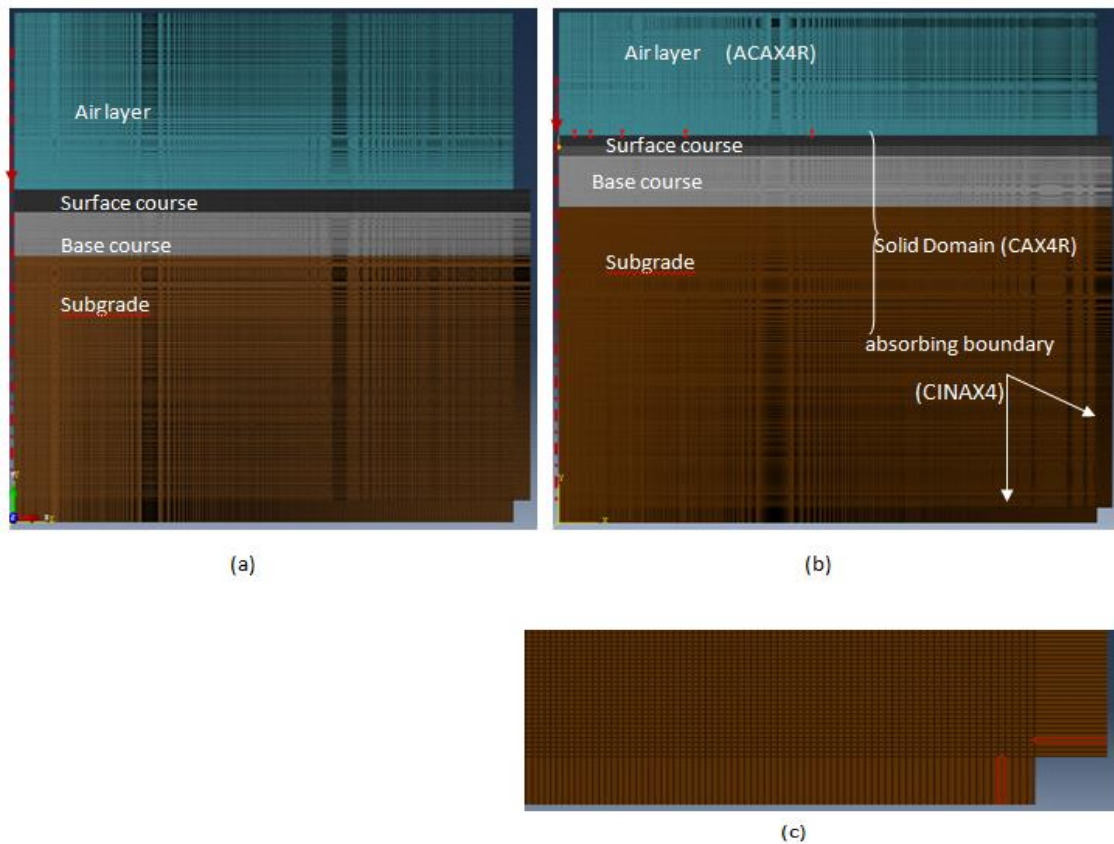


Figure (4-1) Finite element mesh for a 2D axisymmetric model. (a) Three pavement layer system. (b) Four pavement layer system. (c) Absorbing boundary.

4-3 Material Properties

The pavement materials are assumed to be homogeneous and of linearly elastic behavior, since the strain levels during SASW testing are very low, less than 0.001%. The stresses and strains during the SASW test are caused by a very short duration contact load, as will be discussed in the next sections. The gravity field was ignored in the numerical simulation. The air layer was modeled as an acoustic material behavior that permits wave propagation through it. Two material parameters have to be identified to

model the acoustic media in ABAQUS software: the bulk modulus and mass density. Those were set as 423 MPa and 1.2041 kg/m^3 , respectively.

Different layer thicknesses and moduli of elasticity were applied to each of the layers to generate the synthetic dispersion curve database; details about the dispersion curve calculation will be explained later in Chapter 5. The mass density and Poisson's ratio for each layer were assumed to be constant for all modeled pavement profiles. Nazarian and Stokoe (1984) have shown numerically that the effects of these parameters on the dispersion characteristics of surface waves are small, less than 5%. The mass density and Poisson's ratio for the surface asphalt-concrete (AC) layer were assumed to be 2200 kg/m^3 and 0.4, respectively, while for the base and subgrade layers 1700 kg/m^3 and 0.3, respectively. In the case of a single course surface layer (case A) the AC layer thickness (d_1) and Young's modulus (E_1) were taken as 0.1 m and 9000 MPa, respectively. In contrast, the surface layer thickness was assumed to be 0.065m for the two-course AC surface layer (case B). Using those defined parameters, the shear-wave velocity (V_s), compression wave velocity (V_p) and Rayleigh wave velocity (V_R) of the first pavement layer can be calculated using the following relationships, respectively:

$$V_s = \sqrt{\frac{E}{2(1+\nu)\rho}} = 1209 \text{ m/sec} \quad (4.1)$$

$$V_R = \frac{0.862+1.14\nu}{1+\nu} C_s = 1138 \text{ m/sec} \quad (4.2)$$

$$V_p = \sqrt{\frac{E(1-\nu)}{(1+\nu)(1-2\nu)\rho}} = 2960 \text{ m/sec} \quad (4.3)$$

The material damping in the ABAQUS model was defined using the Rayleigh damping coefficients, which defines the damping matrix as a combination of a mass- and stiffness-proportional damping matrices, as shown in Equation (4.4).

$$[C] = \alpha_R[M] + \beta_R[K] \quad (4.4)$$

The stiffness (α) and mass matrix (β) coefficients were set to 0.4 and 0, respectively, for all layers ([Wu et.al, 2014](#)). Table (4.1) shows the values of the parameters used in the generation of synthetic dispersion curves, expressed in terms layer thickness and modulus ratios, with respect to the surface layer.

Table (4-1) Values of parameters used in generation of FE pavement profiles for two study cases.

(a) Three pavement layer system

d_2/d_1	E_2/E_1	E_3/E_1
2	0.02	0.01
2.5	0.04	0.03
3	0.06	0.05
3.5	1.2	0.07
4		
4.5		

(b) Four pavement layer system

d_2/d_1	d_3/d_1	E_2/E_1	E_3/E_1	E_4/E_1
1	5	0.4	0.02	0.01
1.5	5	0.6	0.04	0.02
2	5	1.2	0.06	0.04
2.5	5		0.08	0.08
3	5			

* E_1, E_2, E_3 , and E_4 :stand for first, second, third and fourth layer Young's modulus, respectively.

* d_1, d_2, d_3, d_4 :stand for first, second, third and fourth layer's thicknesses, respectively.

4-4 General Criteria Implemented in FEA

To achieve the needed accuracy of the numerical results, a number of parameters had to be selected carefully during the generation of the finite element models. These parameters are discussed in the following sections.

4-4-1 Overall Dimensions of the Model

There are two factors controlling the overall model dimensions. The first one minimizes potential for wave reflections at the boundaries. To achieve it, the model should be large enough to minimize influence of reflected waves from the edges at desired locations during the analysis. These factors can be calculated from the following equations:

$$t_{max} < \frac{\min(2d-x)}{V_R} \quad (4.5)$$

$$d > \frac{1}{2}(V_R t_{max} + x_{max}) \quad (4.6)$$

where t_{max} is duration of the time record, d the shortest distance between the impact source and the artificial boundary of the model, x the distance between the impact source and any receiving transducer, x_{max} the distance between the impact source and the farthest receiving transducer. These parameters are shown in the Figure (4-2).

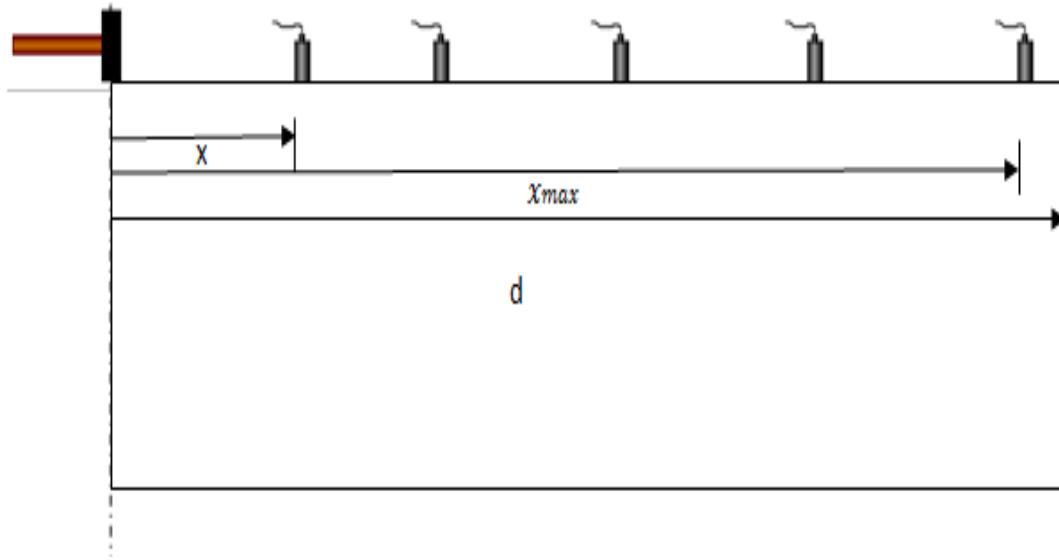


Figure (4-2) The source and sensor arrangement.

In order to select the desired combination for both the model length and recorded time duration, many different pavement structure model lengths were examined within the specific recorded time duration. The investigation included three different lengths (2.5, 3.5 and 4.5 m), while the analysis time was set to 0.004 sec. Based on the obtained results, there were no significant differences stemming from the reflected waves for these three different lengths. The 3.5m length was selected as an optimum length, and satisfies equation (4.6):

$$1/2 * (1138 * 0.004 + 1.6) = 3.076 \text{ m} < d = 3.5 \text{ m}$$

The pavement model depth was set as 2.5 m to provide a sufficient depth for propagation of surface waves of interest, and to minimize the effects of reflected waves from the bottom model edge. The longer wavelength was used to investigate the deeper region, as illustrated in Figure (4-3). The maximum depth of interest includes the subgrade zone with depth equal to 2-3 times the total thickness of the layers above. The receiver's spacing gives an indication about the maximum wave length that could be provided, where the maximum wavelength approximately equal to twice the adjacent receivers spacing.

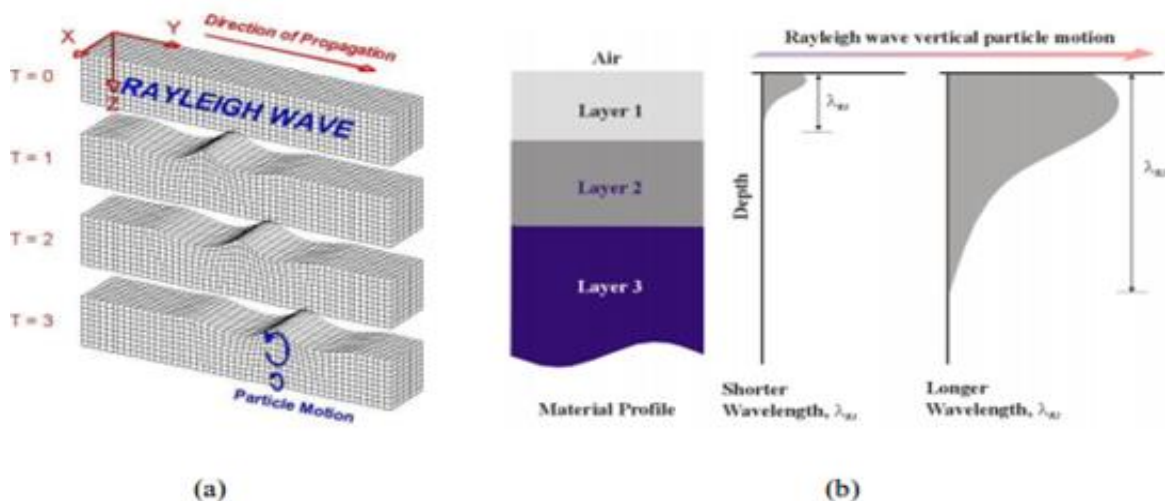


Figure (4-3) (a) The particle motion and direction of Rayleigh wave propagation in a homogeneous medium (b) Variation of vertical particle motion for Rayleigh waves of different wavelengths. ([Ismail et al, 2012](#)).

The SASW test with a common source/receiver (CSR) configuration was simulated for four different single spacing between two sensors: 10, 20, 40, and 80 cm. The distance between the source and the second (far) receiver is twice the distance

between the source and the first (near) receiver, as recommended by Heisey et al. (1982) and as shown previously in chapter three in Figure (3-3).

The air layer thickness was selected after evaluating many trial models. Different layer thickness was investigated to obtain one that reduces the effect of reflected leaked Rayleigh waves from the air layer boundary at the locations of interest during the analysis. Ultimately, the air layer thickness was set to 80cm, which is a sufficient thickness to capture the incident waves of interest, before the reflected waves arrive at a particular location of the air sensor. Figure (4-4) provides an example of the time history recorded by a simulated air-coupled sensor 40cm away from the impact source, and 3 cm above the pavement surface. The obtained results will be discussed in the next chapter.

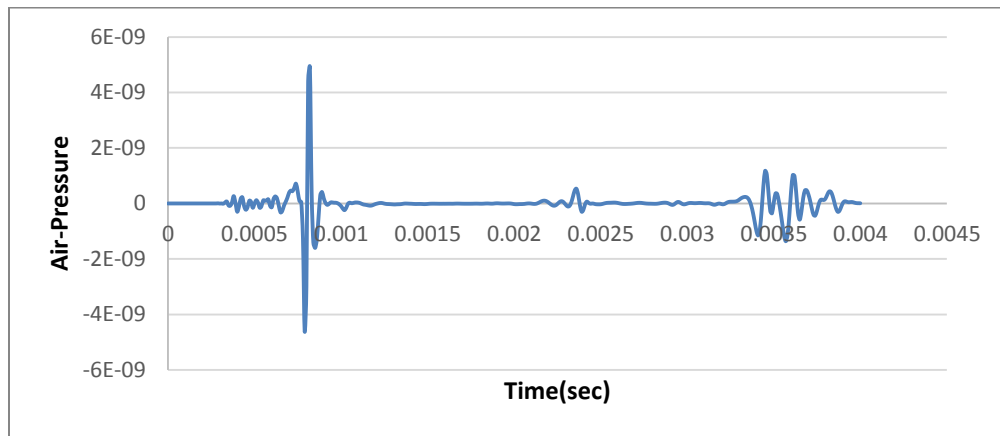


Figure (4-4) Air-pressure time history

4-4-2 Element Size

For the FE wave propagation simulation, the element size selection is considered to be a critical issue, since with the analysis commonly involves propagation of waves of different wavelengths. Very large elements filter higher frequency components, while

very small elements increase the computational time and introduce numerical instability. Thus, in this application, the element size depends on the highest frequency of interest and the lowest wave velocity (V_R) (i.e. the shortest wavelength propagation in the medium). To approximate the element size, the following relationships were suggested by [Zerwer \(2002\)](#):

$$g \leq \chi \lambda_{\min} \quad (4.7)$$

$$\lambda_{\min} = \frac{V_R}{f_{\max}} \quad (4.8)$$

where, (χ) must be less than 0.5, because of the Nyquil limit, and could be taken as 0.25 or 0.2. However, this article adopts the value suggested by [Moser et al. \(1999\)](#), which is the most conservative resolution, by utilizing 20 elements to describe the minimum wavelength.

The decisions in element size selection for wave propagation applications become more complicated when the numerical model includes different materials, like in pavement systems. Therefore, elements of different sizes were used in the model to determine the optimum one that could be used within all pavement layers without any osculation in the analysis results. In this study, the maximum frequency of interest, $f_{\max}=35000\text{Hz}$, and by considering the minimum surface-wave components,. Thus, the surface layer shear and surface wave velocities, $V_s=1209\text{m/sec}$ and $V_R=1138\text{m/sec}$, were considered to calculate the minimum wave length:

$$\lambda_{\min} = 1138/35000 = 0.03\text{m}.$$

Ultimately, the element size was defined as 1mm to satisfy the following condition:

$$\text{Element size} \leq 30/20 = 1.5\text{mm}$$

In order to minimize the computational time, a gradual mesh size of 1 to 20 mm was used. The element size increases gradually in both vertical and horizontal directions without causing any numerical instability, as shown in Figure (4-5).

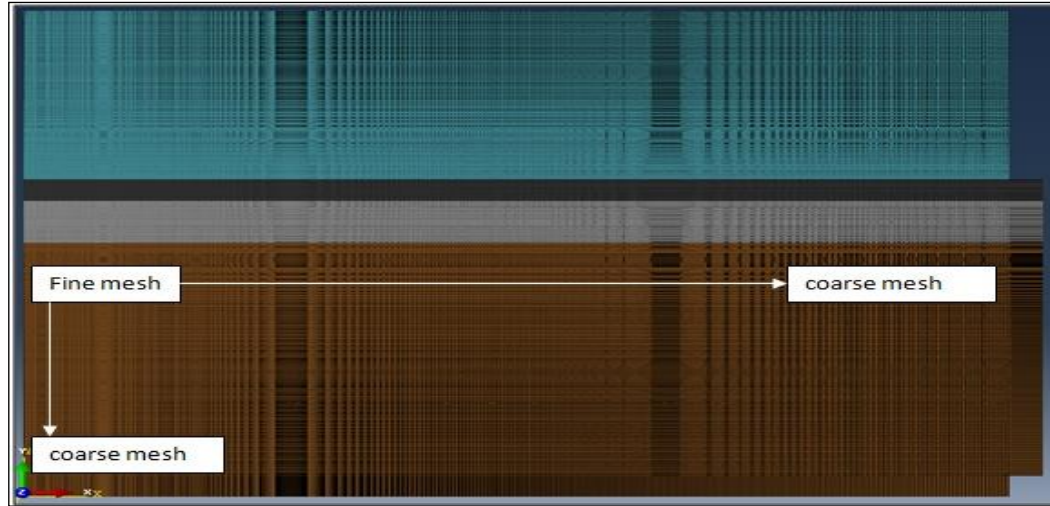


Figure (4-5) Gradual finite element mesh

4-4-3 Time Step

The time step should be selected in way to be small enough to permit the fastest compression waves to pass through all elements within the model, and to prevent the compression waves from "jumping over" the smallest ones. On the other hand, selecting a very small time step will cause a numerical instability and cause oscillations resulting in "Gibb's phenomenon". The time step selection depends on the effective element length ([Zerwer, 2002](#)) as described in the following equation:

$$\Delta t \leq \frac{L_e}{V_p} \quad (4.8)$$

In this study, the time step was set as 0.1μs, based on the compressive wave velocity of the surface layer, and by trial and error within the criteria limitation. This time step is satisfying Equation (4.8), where the highest compressive wave velocity considered

in this study is equal to 2960 m/sec, and the effective element length is 0.001m. Consequently:

$$t=0.001/2960=3*10^{-7} \text{ sec}$$

4-4-4 Impact Duration

The impact source for the SASW test should be able to generate surface waves within abroad frequency range. To simulate the test in FEM, the impact load can be defined by different mathematical functions, such as Dirac delta excitation input function ([Lu and et.al. , 2010](#)), Ricker wavelet ([Ryden et.al., 2002](#)), and a half-sine function ([Hughes, 1987](#); [Kim JH, 2008](#)). In this study, the impulse load was approximated using a half-sine curve, as illustrated by equations 4.9 and 4.10.

$$f(t) = a \sin^n \left(\frac{\pi t}{T} \right) \quad 0 \leq t \leq T \quad (4.9)$$

$$f(t) = 0 \quad t > T \quad (4.10)$$

Generally, use of this function to induce the impulse load is dependent on the appropriate selection of contact time (T) between the point load source and the model surface. In addition, the amplitude (a) and the power of sine function (n) should be defined. To determine the suitable contact time and power of sin function that provides the required range of frequencies, as well as to avoid Gibbs phenomenon, different sine shape functions to induce the pulse load were simulated in ABAQUS. The maximum amplitude of the load was assumed 1N. To investigate the effect of the total contact time on the received signal, the power of the sine function was assumed to be of the 3rd order where this order is the minimum order required to be used if acceleration is the desired response

(Kim and Kwak, 2008). Pulses of unit amplitude for three different contact times were investigated: 10, 30 and 40 μ s, as shown in Figure (4-6).

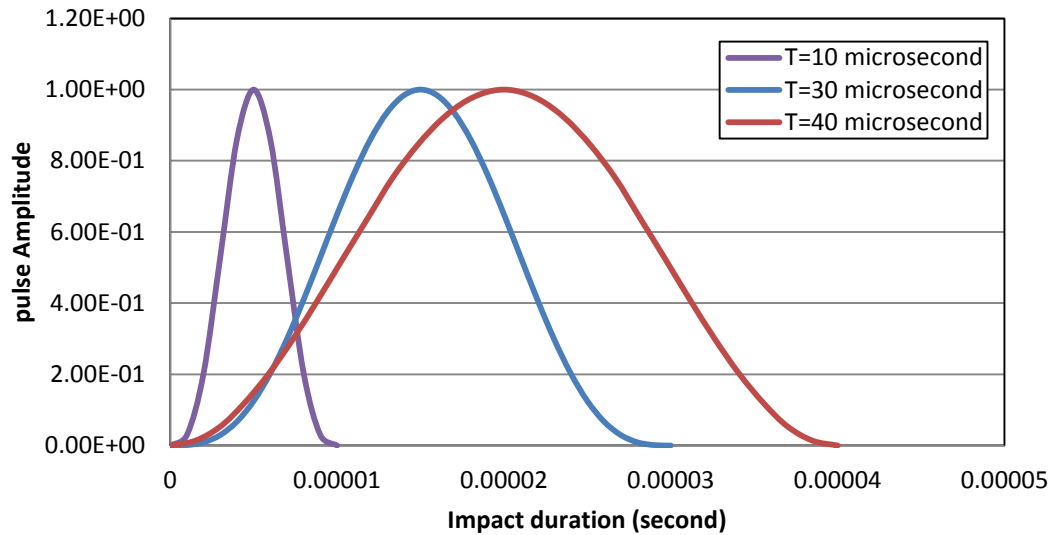


Figure (4-6) Half-sine load functions for different contact times

The load was simulated as a point load located at the upper left corner of the pavement surface (at the axis of symmetry), as shown previously in Fig. (4-1). The results of the analysis are presented in terms of obtained time histories at a distance 40 cm from the source for both contact and air-coupled sensors. Using a total contact time of 10 μ s will cause numerical instability and result in oscillations, as shown in Figure (4-7). Illustrated in the figure are the time histories for vertical velocity, displacement, acceleration and air-pressure at a 40 cm distance from the impact source, and 3 cm above the pavement surface for the simulated air-coupled sensor.

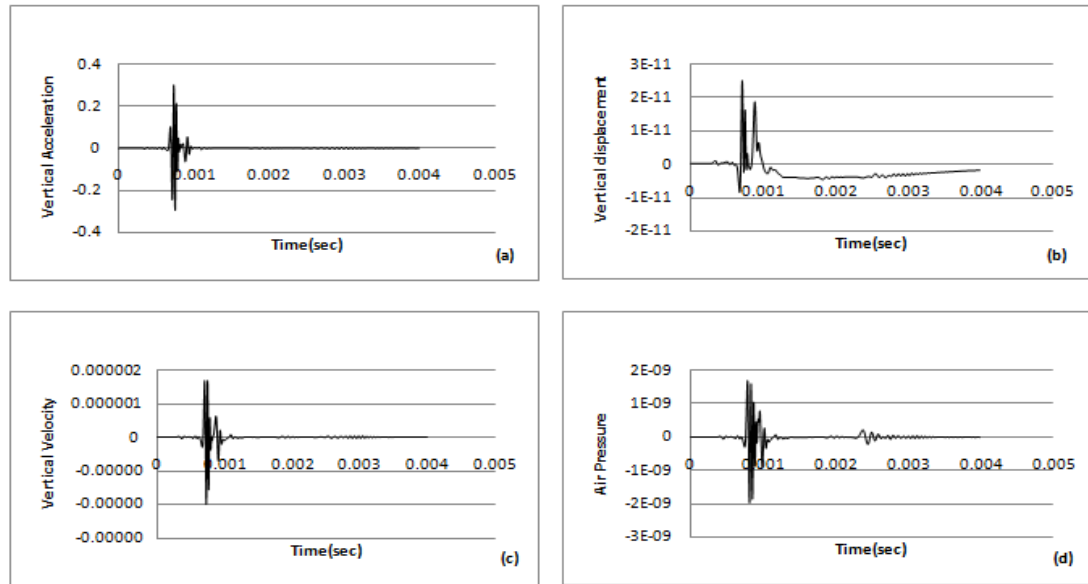


Figure (4-7) Time histories at a 40 cm distance from the impact source for an impact with a $10\mu\text{s}$ contact time: (a) acceleration, (b) displacement, (c) velocity, and (d) air-pressure.

The total impact duration of $30\mu\text{s}$ was found to be suitable for generating the needed energy in the frequency range of interest. Sample response time histories are shown in Figure (4-8).

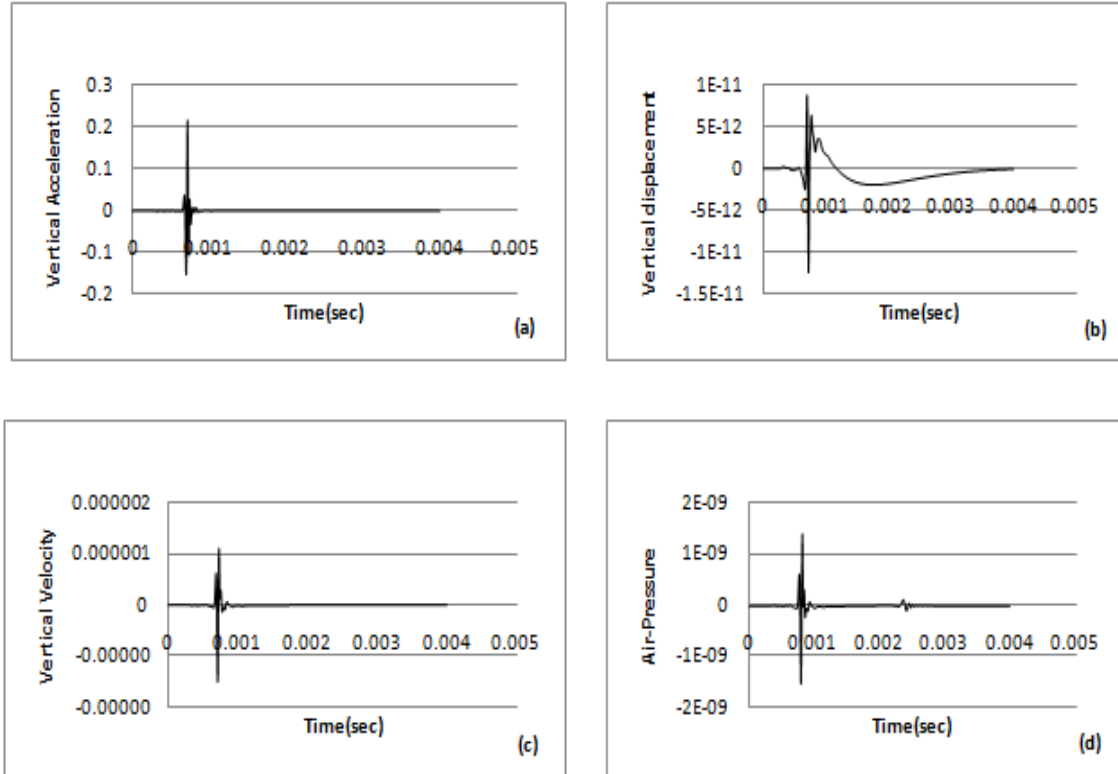


Figure (4-8) Time histories at a 40 cm distance from the impact source for an impact with a 30 μ s contact time: (a) acceleration, (b) displacement, (c) velocity, and (d) air-pressure.

Furthermore, the power of the sine function was also investigated to decide the minimum order needed for this study. Three different sine power coefficients (n) were applied: 1, 2 and 3, in the half-sine function. The functions with a contact time of 30 μ s are shown in the Figure (4-9). It was found that using a higher order shape function is the most suitable selection to generate a broad range of frequencies.

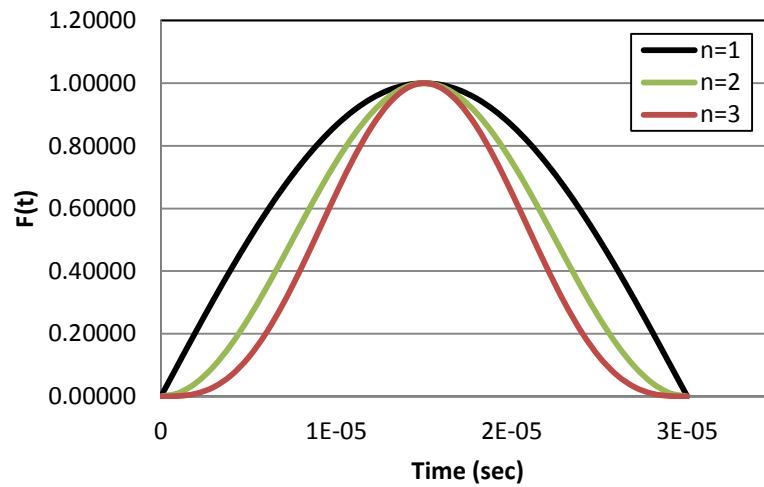


Figure (4-3) Half-sine function shapes as a result of change of the sine power coefficient.

The frequency spectrum of a half-sine function for the selected impact duration and sine power is plotted in Figure (4.10). The plots show that using the total contact time of 30 μ s and 3rd sine power for the half-sine function will provide sufficient energy in the range of frequencies of interest for this study.

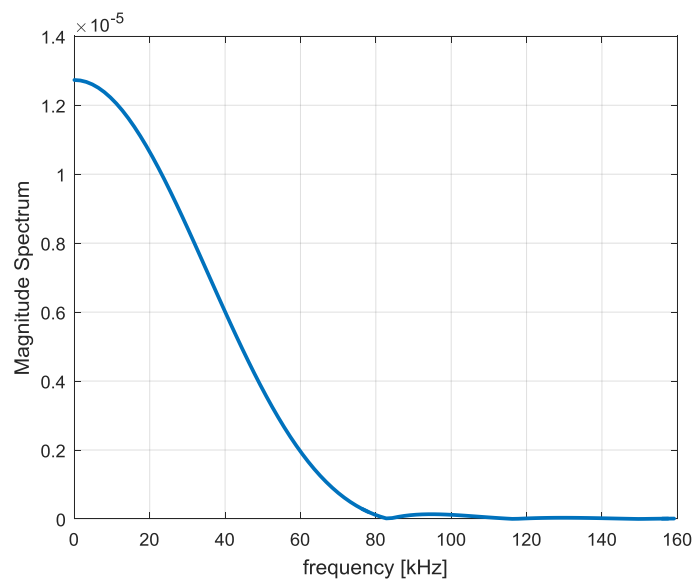


Figure (4-4) Spectral magnitude for the selected pulse load

4-5 Receiver locations

Five receiver locations were identified to simulate SASW tests for four different receiver spacings. Each receiver was numerically simulated by time histories for a node located at the pavement surface providing for further calculation of dispersion curves for the corresponding receiver spacing. After that, the four dispersion curves were combined to obtain the average dispersion curve. The detail of this process will be discussed later in Chapter 5.

Moreover, five non-contact sensors (i.e. air-coupled sensors or microphones) for detecting the leaky Rayleigh waves were simulated by air-pressure histories at nodes located within the air layer at the same distance from the impact source. Four different non-contact sensor heights from the pavement surface were investigated: 1, 2, 3 and 5 cm. The goal of this investigation was to avoid placement of the sensors in the shadow zone, where no leaky surface waves could be detected, and consequently to avoid its negative effect of a complicated data analysis ([Zhu and Popovics, 2007](#)).

As described previously in section 3.5, and according to the shadow zone calculation equation, the shadow zone height was checked for 30, 60, 90, and 150 cm distance from the source, and for each considered height distance. The leaky angle is determined by Snell's law as:

$$\sin(\theta) = C_{\text{air}}/C_{\text{LR}} \quad (4.10)$$

where C_{air} is acoustic wave velocity in the air (343 m/s).

C_{LR} is leaky Rayleigh wave velocity in the surface layer (1138 m/sec). Thus, the leaky wave angle is equal to 17.38° , and the shadow zone distance can be calculated as $h \cdot \tan(\theta)$, where (h) is the height. Therefore, a larger distance between the impact source and a

higher positioned sensor is recommended to reduce the negative effect of the direct acoustic waves and shadow zone. Ultimately, simulated air-couple sensors were located at a 3 cm height from the pavement surface as shown in Figure (4-5).

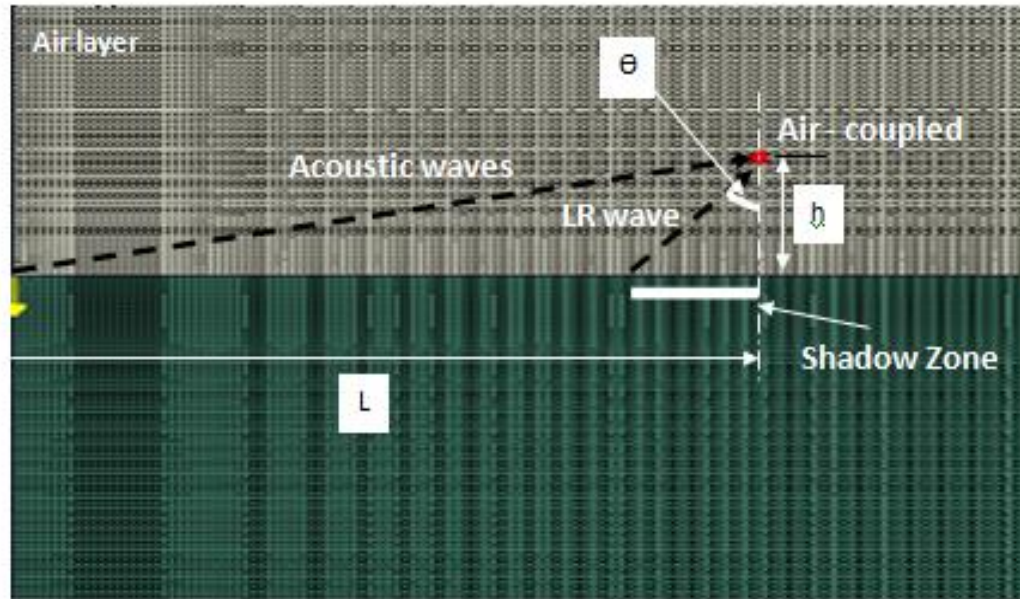


Figure (4-5) Air-coupled sensors' location

4-6 Verification of Wave Development through the Fluid Solid Half Space System

ABAQUS software provides visualization of any of the requested parameters (i.e. snapshots of the computed results). This tool enables one to verify the wave field development in both solid and fluid spaces. Figure (4-12) provides a snapshot of the air-pressure output parameter (POR) requested for the fluid finite elements. The two main wave fronts were developed by the impulse load through the fluid medium: the acoustic radiation from the surface wave (Leaky Rayleigh wave (LR)) and the direct acoustic wave. The LR wave can be described as a plane wave with the Rayleigh angle calculated using the previously described Equation (4.10). Otherwise, the acoustic wave is a

spherical wave generated by the impact monopole source. The Rayleigh angle obtained from the simulation result was 18° , which is very close to the theoretical angle of 17.38° calculated using equation (4.10). The difference might be due to the consideration of the top layer as a homogeneous half-space. A similar validation was given by [Zhu et al. \(2002\)](#) and [Lu et al. \(2015\)](#).

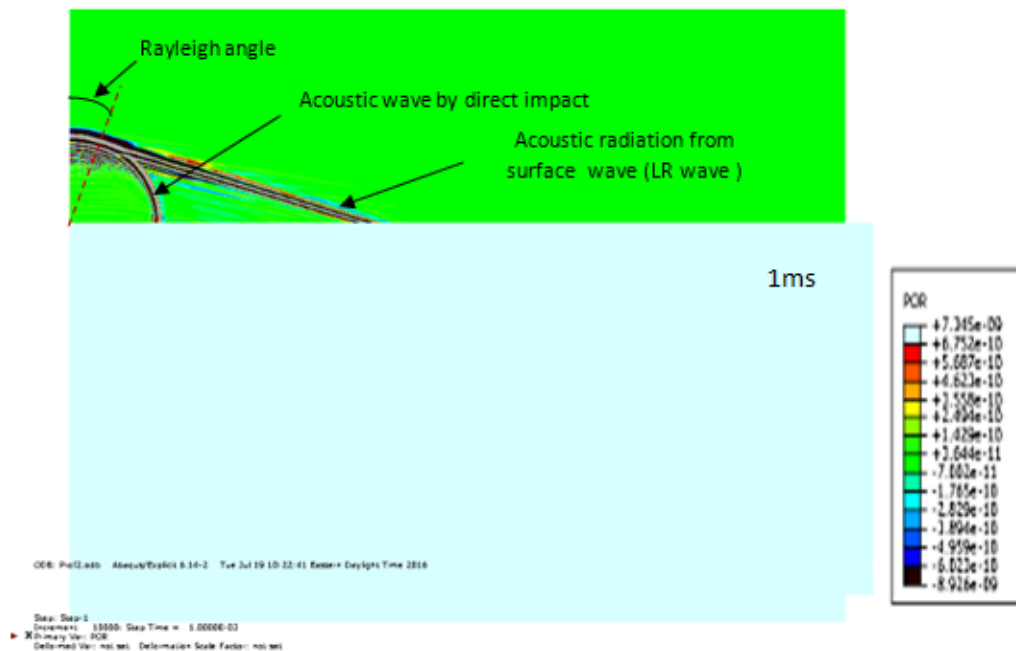
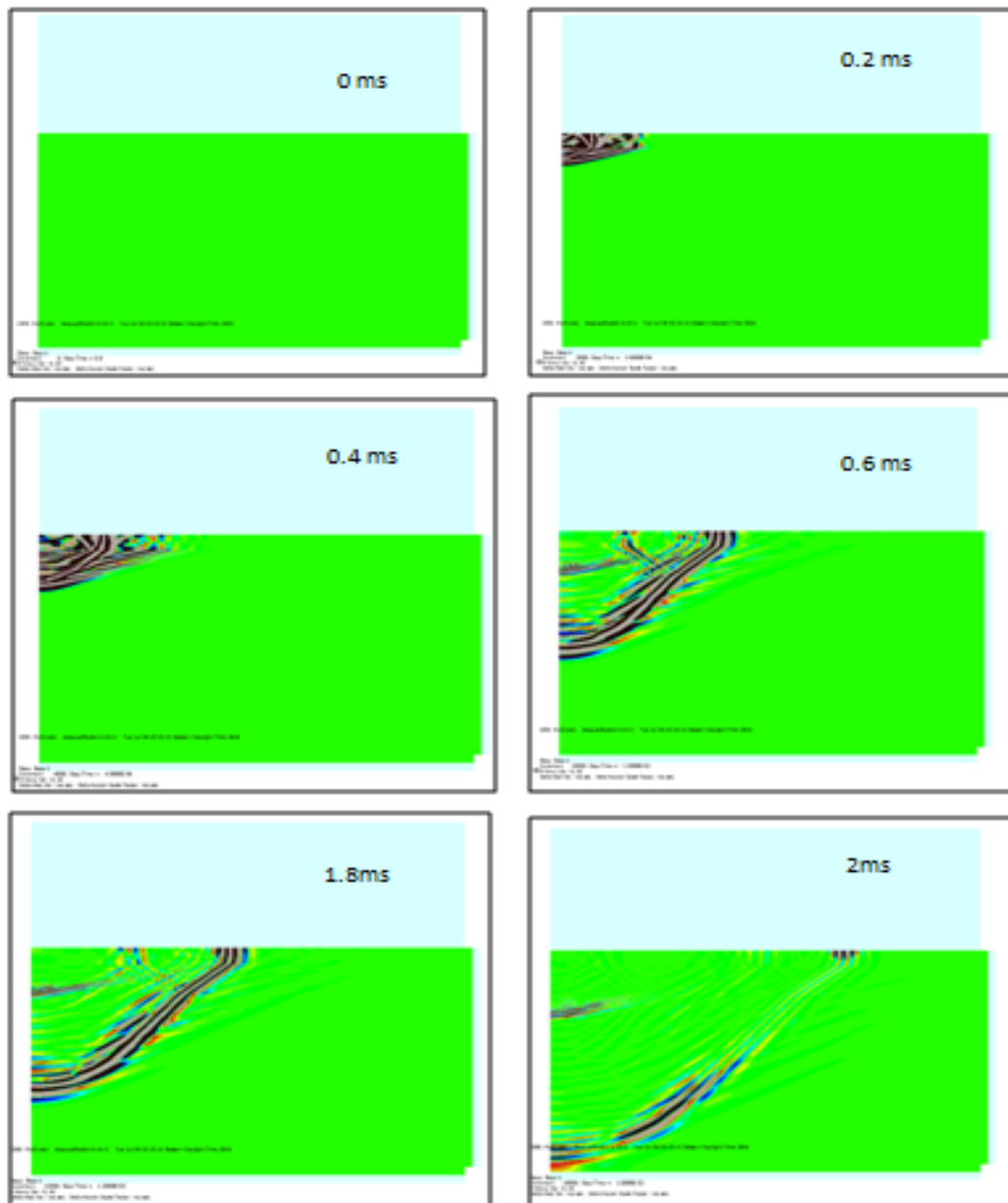


Figure (4-6) The air pressure wave at time 1ms.

Figure (4-13) shows progressive snapshots of the vertical acceleration in the solid medium (pavement layer FEM model). The wave front is propagating through all the pavement layers as expected, with presence of weak reflections at the boundary of two adjacent layers.



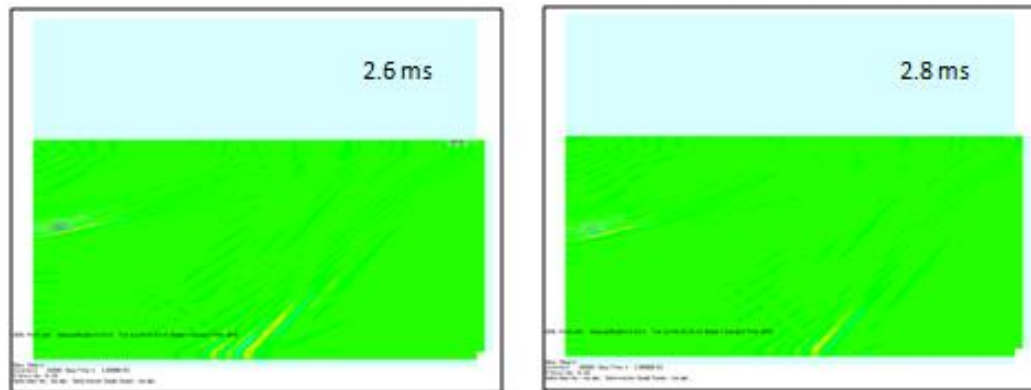


Figure (4-7) Snapshot of the vertical acceleration field.

(The step time is shown on each snapshot)

The snapshot at step time 2.6 and 2.8 m show that the wave fronts fade away as they reach the side and bottom boundary without any reflection. As illustrated, such visualization helps ensuring that the selected model length is adequate, and that the absorbing boundaries are preventing the reflection to occur.

CHAPTER FIVE

Inversion Analysis of Air-Coupled SASW Test by ANN

5-1 Introduction

In general, to evaluate the modulus profile, there are two problems have to be solved. The first one is forward problem which includes predicting the results of measurements based on some general principle and a set of specific conditions (model parameters) ([Orozco, 2003](#)).

The second problem is the inversion problem which addresses the reverse issue: estimating the model parameters based on measured data and a general principle. For the SASW test, these two problems can be solved by initially guessing profile based on the experimental dispersion curve (i.e. inversion process). Then, the theoretical dispersion curve for each specific initially guessing profile is calculated using the wave propagation theory (i.e. forward modeling) ([Hadidi and Gucunski, 2003](#); [Tarantola, 2005](#); [Shirazi et.al, 2009](#)). Figure (5-1) shows the main concept of the forward and inversion problem.

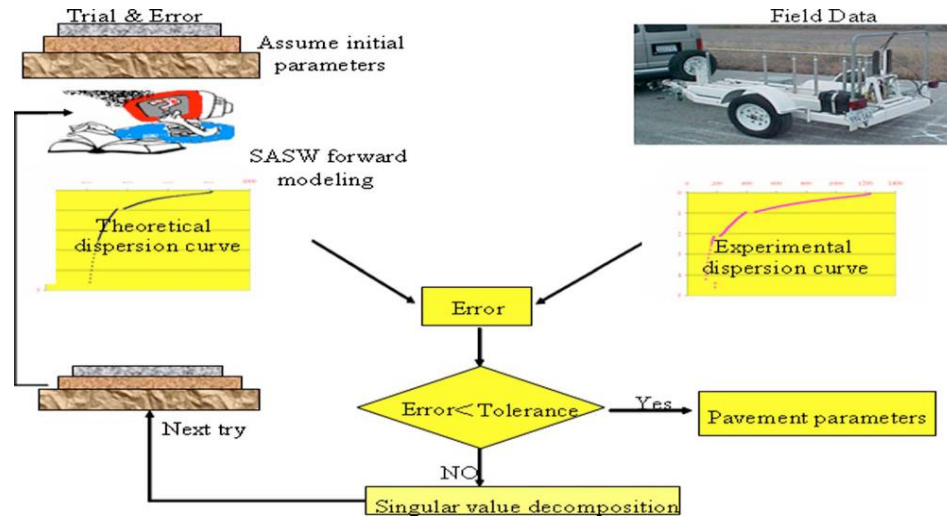


Figure (5-1) Main concept of forward and inversion problem ([Shirazi et.al, 2009](#)).

The theoretical dispersion curve is compared with the experimental one by applying an appropriate error function. If the two dispersion curves do not match, the initial profile is adjusted, and another theoretical dispersion curve is calculated. After several iterations, if the two curves match sufficiently, the associated assumed profile is considered to be the correct one ([Nazarian and Stokoe II, 1984](#); [Gucunski and Woods, 1991](#); [Joh, 1996](#)).

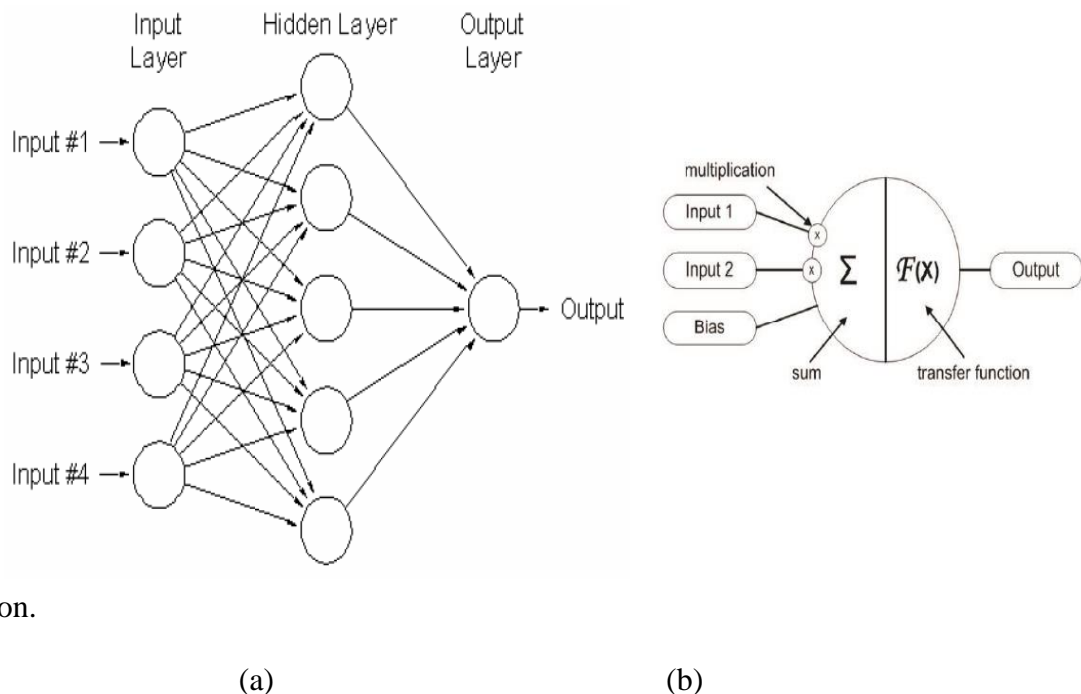
In this chapter the fundamental concepts of the inversion methods are explained; focusing on the Artificial Neural Networks (ANNs) approach, which was adopted in this research for the inversion analysis.

5-2 Overview of Artificial Neural Networks (ANNs)

ANNs represent mathematical non-linear models, which try to mimic the structure and functionality of a real biological neural network to solve a wide variety of problems

([Hecht-Nielsen, 1989](#)). They are composed of a set of parallel and distributed processing units called the 'artificial neurons' or 'nodes'. Each of them is a mathematical function, which has three sets of calculations: multiplication, summation and activation.

Usually, these neurons are organized in layers: an input layer, one or more hidden layer(s), and an output layer. The information flows from the input layer to the hidden layer, and then to the output layer. The layers are connected and have to have associated connection strengths (weights) represented by w_{i1} , w_{i2} , w_{i3} , etc. Each unit performs a weighted sum on the inputs and uses a transfer function to compute its output. These layers represent the architecture of the ANNs ([Hecht-Nielsen, 1989](#); [Villacorta et.al, 2017](#)). Figure (5-2) shows schematic views of a typical ANN architecture and an artificial



neuron.

Figure (5-2) (a) Schematic view of typical ANN architecture (b) Artificial neuron ([Hecht-Nielsen, 1989](#))

The architecture of the network (number of hidden layer and number of neurons in each layer) control the type of calculation performed by the neural network. The most common architecture used for mapping, classification and forecasting are the multilayer, feed-forward network and back-propagation network. In the forward network, the neuron's output is never dependent on the output of subsequent neurons. Signals only go forward through the network with no loops. In contrast, the signals in back-propagation network could be transferred backward to adjust its weight and get the minimum error between the input and the target.

5-3 Transfer Function

The transfer functions transform the weighted sum of inputs for each artificial neuron to its computed output. The transfer functions usually have a sigmoid shape, but they may also take the form of the non-linear functions, piecewise linear functions, or step functions ([Wilby et al., 1998](#)). The three most commonly used transfer functions are explained below and shown in Figure (5-3):

- **Log-sigmoid transfer function (LOGSIG):** This is considered one of the most commonly used functions in multilayer networks that are trained using the back-propagation algorithm because this function is differentiable. LOGSIG function takes the input that may have any value between plus and minus infinity and squashes the output into the range 0 to 1.
- **Hyperbolic tangent transfer function (TANSIG):** This function has an output in the range of -1 to +1. This function is equivalent to \tanh , but it is considered faster

in the run than tanh. This function is a good tradeoff for neural networks, where the speed is more important than the exact shape of the transfer function.

- **Purelin transfer function**: This is perfectly used with the models that have input/output close enough to linear characteristics and in back-propagation networks.

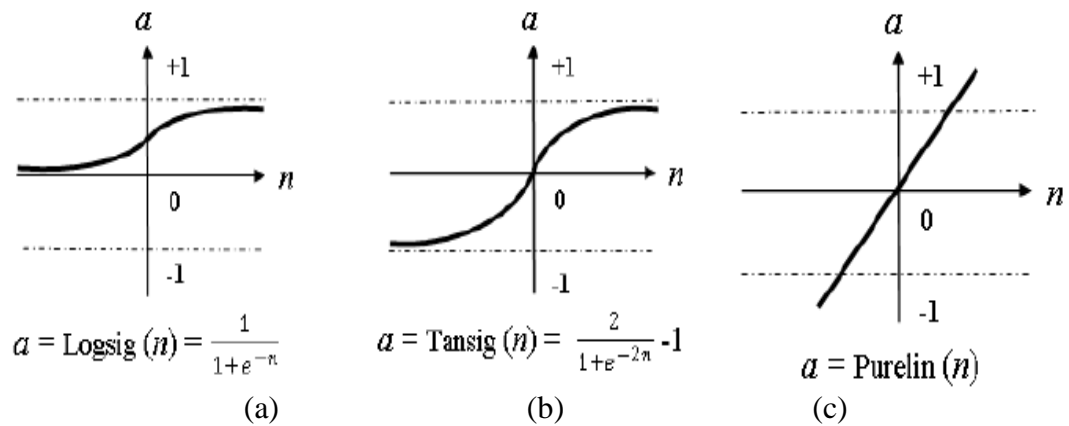


Figure (5-3) Transfer Functions (a) LOGSIG (b) TANSIG (c) Purelin ([Hecht-Nielsen, 1989](#))

5-4 ANN Models' Development

In this research, the neural networks were developed using MATLAB software.

The ANNmodels' development included the following steps:

5-4-1Development of Training and Testing Sets

The input data sets are represented by the synthetic dispersion curves obtained from the numerical simulation of the SASW test. These synthetic curves were calculated from the acceleration and air pressure time histories captured by the accelerometers and

air coupled sensors; respectively; for three- and four-layer pavement profiles, as discussed previously in Chapter 3 and 4. The samples sets were divided into four groups:

- **Group1** included ninety-six synthetic dispersion curve cases for contact sensors (accelerometers) for three-layer pavement systems. This group was split into two sets: a training set of eighty-one, and a testing set of the remaining fifteen cases.
- **Group2** included eighty-five synthetic dispersion curve cases for non-contact (air-coupled) sensors for three-layer pavement systems. This group was split into two sets: a training set of seventy-two, and a testing set of the remaining thirteen cases.
- **Group3** included two hundred and twenty one synthetic dispersion curve cases for contact sensors (accelerometers) for four-layer pavement systems. This group was split into two sets. A training set of one hundred eighty-eight cases, and a testing set of the remaining thirty-three cases.
- **Group4** included two hundred synthetic dispersion curve cases for non-contact (air-coupled) sensors for four-layer pavement systems. This group was split into two sets: a training set of one hundred and seventy cases, and a testing set of the remaining thirteen cases.

The synthetic dispersion curves in the training sets for each group were defined in terms of dimensionless velocity versus dimensionless frequency to enable application of the database to much wider range of pavement profile, where the dimensionless velocity, V_{nor} (nor stands for normalization) is given as shown in equation (5.1):

$$V_{nor} = V_{ph} / V_{s1} \quad (5.1)$$

where V_{s1} is the shear wave velocity of the surface course and V_{ph} is the phase velocity.

The dimensionless frequency f_{nor} is given by the following equation (5.2):

$$f_{nor} = f \cdot d_1 / V_{s1} \quad (5.2)$$

where f is the frequency and d_1 is the surface layer thickness.

Each of Group1 and Group2 cases was with 123 inputs. All the curves in these two groups were defined for the same set of 123 dimensionless frequencies in the range from 0.07-1.3 with a step of 0.01. For Group3 and Group4, all the curves were defined for the same set of 174 dimensionless frequencies in the range from 0.05-1.8 with a same frequency step of 0.01, as shown in Figure (5-4).

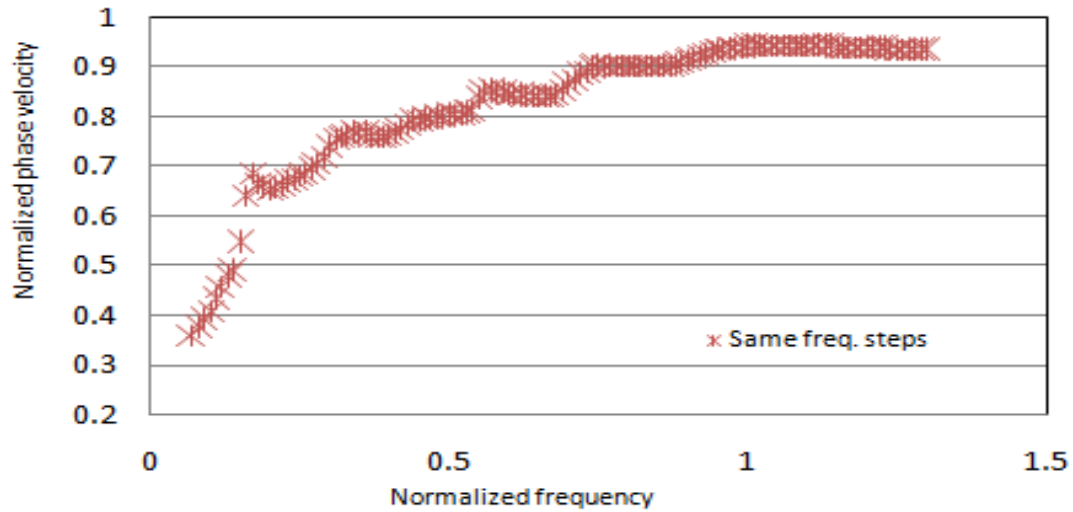


Figure (5-4) Normalized dispersion curves defined by same frequency step.

To better identify the dispersion curve for each pavement profile, and to improve the ability of the automated system to evaluate the deepest pavement layers, the input points for each dispersion curve for the previous four training groups were defined for

two different frequency steps. Small or narrow step of 0.005 was assigned for the low dimensionless frequency (or long wavelength) range from 0.04-0.99. A larger step of 0.01 was assigned for the high dimensionless frequency (short wavelengths) range from 1-1.8, as shown in Figure (5-5).

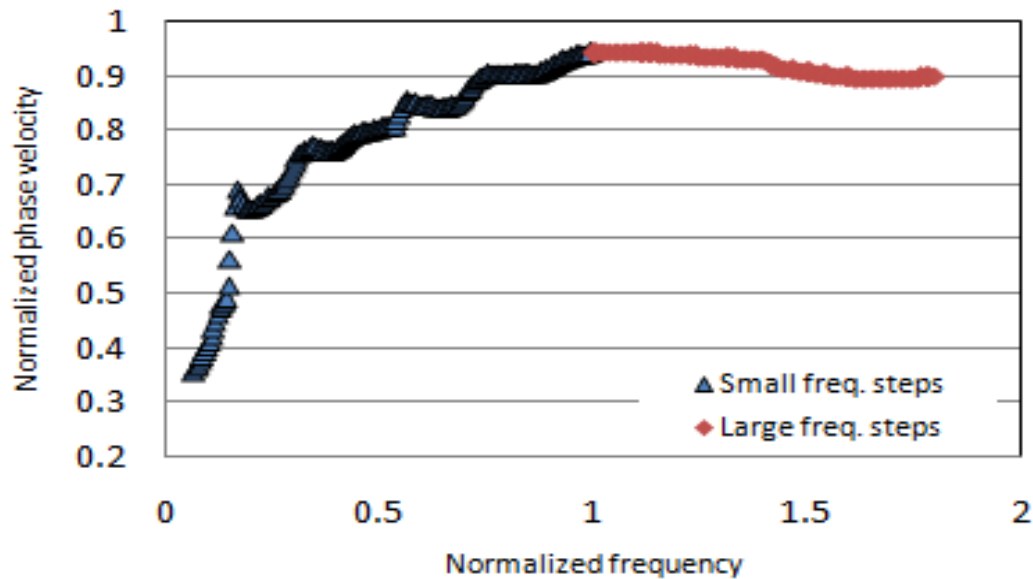
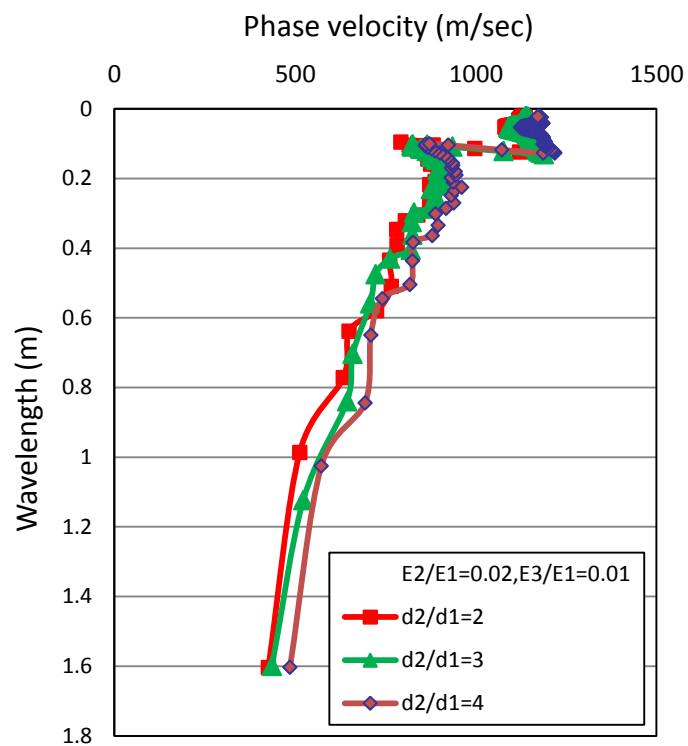
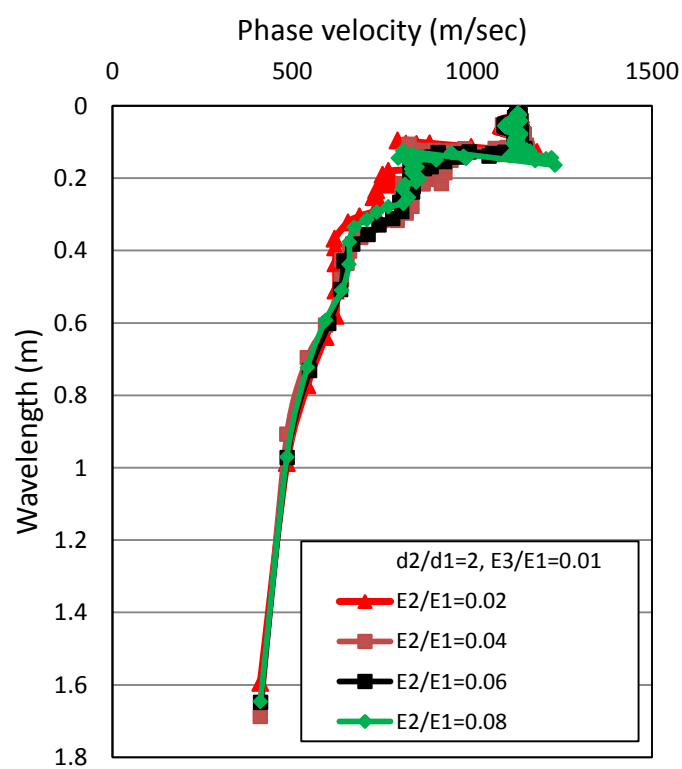


Figure (5-5) Normalized dispersion curve defined by two different frequency steps.

The output of each training case is a pavement profile, which is described by the thickness ratio (d_i/d_1) and the modulus of elasticity ratio (E_i/E_1), where i refers to the pavement layer index. Figure (5-5) provides examples for the effect of each output parameter on the shape of randomly selected synthetic dispersion curves. It is provided in terms of the phase velocity vs. wavelength, and based on the air pressure time histories from the air-coupled sensors.



(a)



(b)

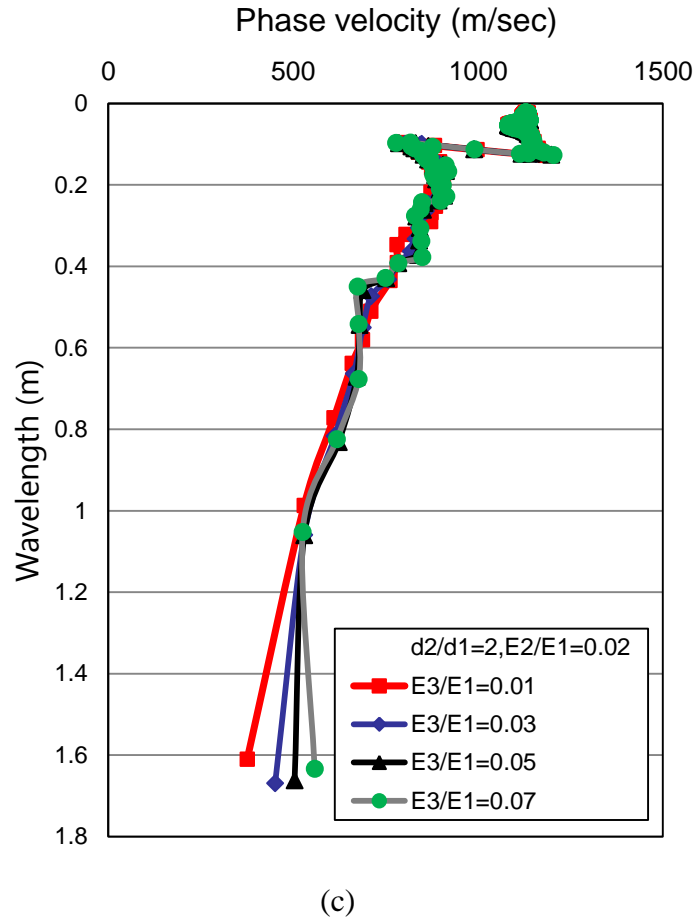


Figure (5-6) Effect of the output parameters (a) d_2/d_1 (b) E_2/E_1 (c) E_3/E_1 on the dispersion curve's shape based on air pressure time histories

5-4-2 ANN Training Process

The ANN training is the process where the ANN gains knowledge stored as the connection strengths. In general, there are three types of ANNs learning: learning with supervision, learning without supervision and reinforcement learning. Learning with supervision includes a selection of training data (i.e. 'teaching data') from the database collected previously, and they are assigned to input layer after being multiplied by initial weights. The neuron then sums the weights of all inputs and bias. At the exit of the

artificial neuron, the sum is passed through an activation function, or what is also called a 'transfer function'. After that, the ANN outputs are compared with the sets of data called 'target data'. To adjust the connection strengths so as to minimize the differences between the calculated and target outputs, a learning algorithm is employed. Therefore, a set of input/output values are required for this learning mode ([Bishop, 1995](#)).

In contrast, in unsupervised learning, the targets are unknown and learning must now be accomplished based on observation of responses to inputs for which marginal or no knowledge exists. In this mode of learning, the network must discover for itself any possibility of existing patterns. The third form of learning, the reinforcement learning, is the one in which information is supplied, whether the network outputs are good or bad, but again no actual designed values are given ([Bishop, 1995](#)). In this research, the supervised mode was considered for learning the ANN models.

To start the training stage, there are many elements that have to be decided to create an adequate network, a network that provides a reasonable output. These elements include the number of hidden layers, total number of nodes in hidden layers, selection of the network algorithm, and which type of learning function has to be applied. Besides, it includes a selection of the correct transfer function, since it is considered to be an important element that affects the network output.

MATLAB ANN toolbox provides several options for all of the mentioned elements. Different combinations were investigated in this research. The most optimized network, one with the least error rate and iteration number for convergence, was selected and tested for certainty. Backpropagation algorithm was used in developing all the ANN models, since it is suitable for the complex nonlinear behavior of the SASW inversion

process ([Williams and Gucunski, 1995](#); [Gucunski et al, 1995](#); [Nazarian et. al, 2004](#)).

Three and five hidden layers were used for developing ANN models for three- and four-layer pavement systems, respectively.

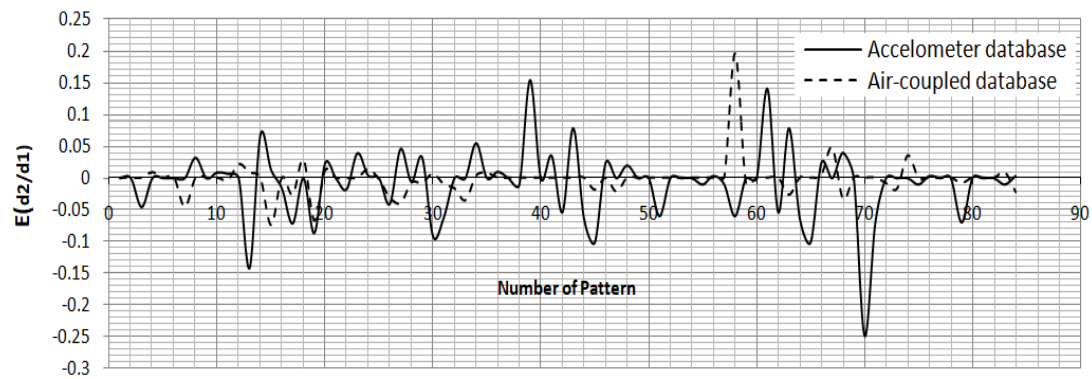
To improve matching with a lower mean squared error between the networks' outputs and the actual data, four different numbers of neurons in hidden layers: 6, 12, 24, and 48, were investigated. The best results were obtained for a total number of 12 neurons in hidden layers when the ANN models were trained using Group1 and Group2 sample sets. In contrast, five different total numbers of neurons in hidden layers 24,48,60,72 and 75 were investigated, when the ANNs models were trained using Group3 and Group4 sample sets. In this case, the total number of 60 neurons in the hidden layers was selected. That indicated that it is unconditional by increasing the number of neuron could give a better estimation of the required outputs.

The mean squared error (MSE) was calculated by using the following equation (5.3):

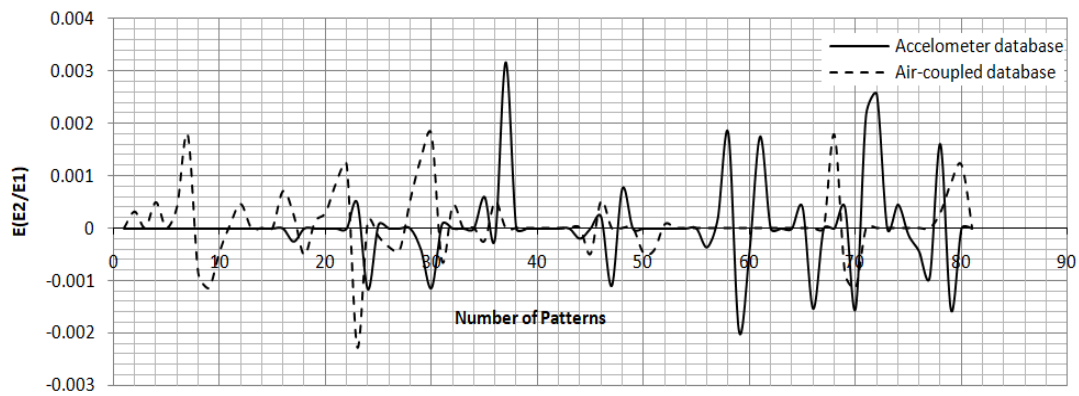
$$MSE = [\sum(A - P)^2]/n \quad (5.3)$$

where: A is the actual output value, P is the value output by the neural network and n is the number of cases in the training set.

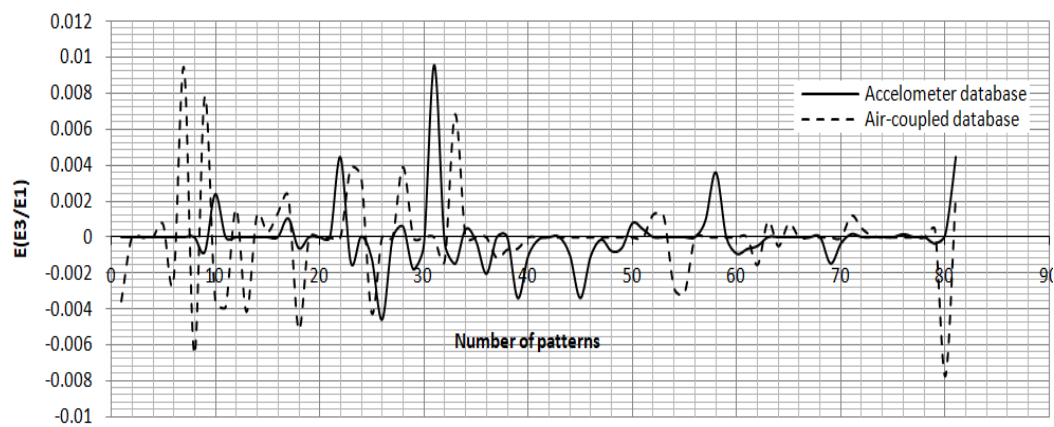
Figure (5-7) provides an example of the comparison of errors computed from the difference between the predicted and the actual output parameters, when the networks were trained using Group1 and Group2 sets. In those graphs, it can be seen that by increasing the number of patterns (i.e. number of input data); the computed error based on accelerometers and air-coupled database varies randomly. However, this variation was within a close range to each other for each predicted output parameter.



(a)



(b)



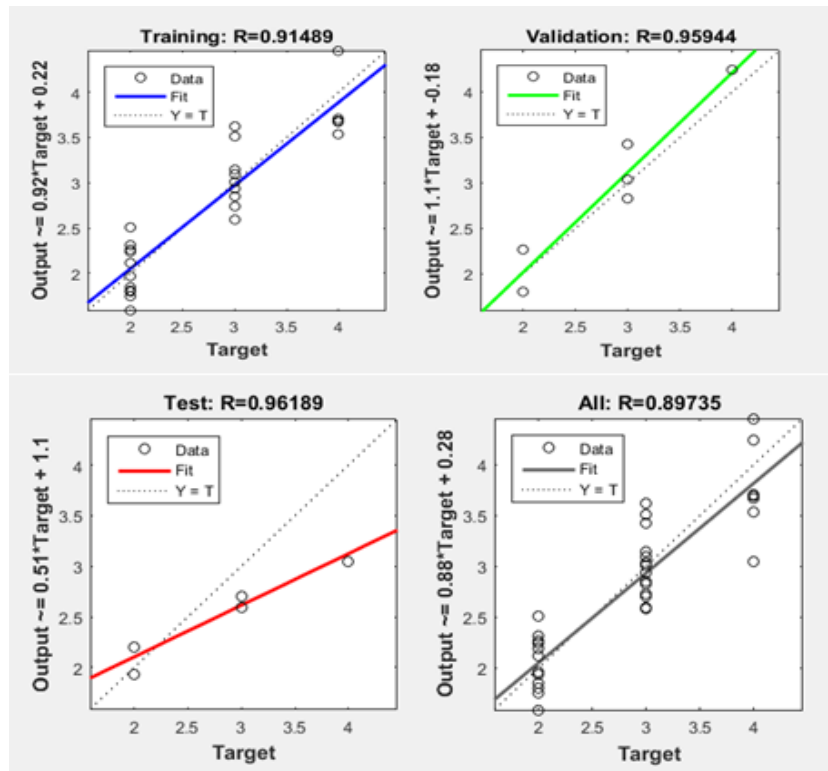
(c)

Figure (5-7) Comparison in the computed error of the output parameters (a) d_2/d_1 ; (b) E_2/E_1 and (c) E_3/E_1

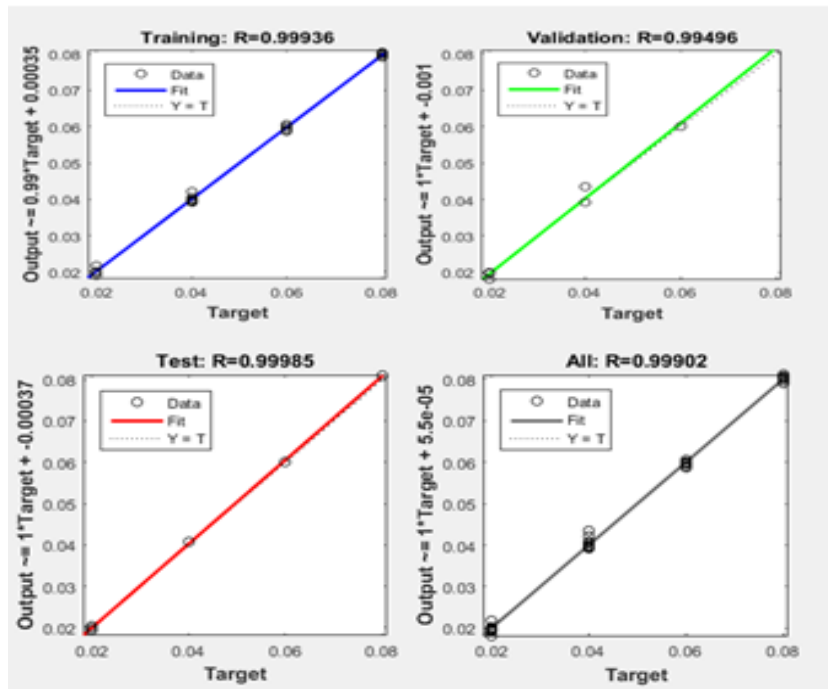
All previous investigations were done under two training strategies. The first one was by training the networks to predict the overall output simultaneously. On the other hand, the second training strategy included development of one model for each required output parameter, so that the model's accuracy and architecture will be influenced by only one output variable. The second training strategy was followed in this research since it gave a lower mean squared error.

Monitoring the training process is very important, especially when the regression plot is accessible during this process. That will enable the one to predict whether or not the training should be terminated. When the regression constant R is close to one in the plot presented by MATLAB ANN toolbox, this means that the training process is going as desired ([Beal et.al,2018](#)). Figure (5-8) shows an example of this plot during the ANN development process for each of the output parameters.

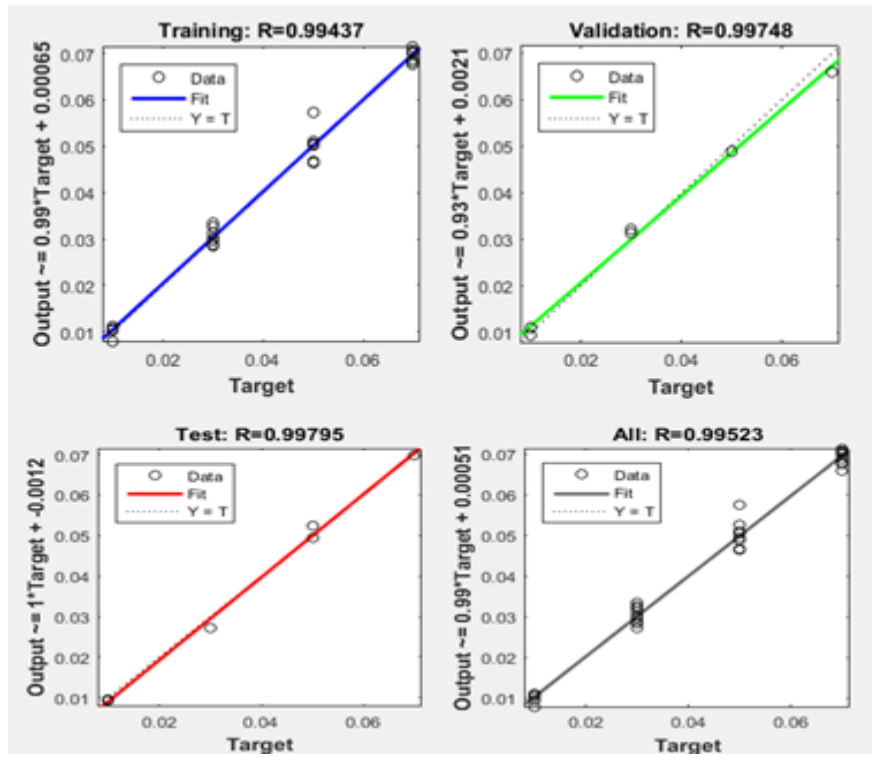
According to previous figure, the training data for each output parameter indicates a good fit. The validation and test results also show high R-values. The scatter plot is helpful in showing that certain data points have a poor fit. Such is the data point in the test set of d_2/d_1 output parameter, for the illustrated example, whose network output is less than the corresponding target. Therefore, this data point was further investigated and it was found out that additional training data should be used to improve the estimate output.



(a)



(b)



(c)

Figure (5-8) Regression plots for generated by MATLAB ANN toolbox for each output parameter (a) d_2/d_1 , (b) E_2/E_1 and (c) E_3/E_1 for three-layer pavement system

To enhance the ANN models' profile detection in the case of three-layer pavement systems, a further investigation was done. This investigation included using the database of dispersion curves for individual receiver spacings, instead of using the average dispersion curves, to train the ANN models. This was done since there is a difference in dispersion curves for various spacings due to different interferences of a number of body and surface wave components.

In order to deal with the missing data due to applying the filtering criteria on each individual dispersion curves for the same pavement profile, the MATLAB code was adjusted to replace the missing data in the dispersion curves with the average value

([Sharpe and Solly, 1995](#)). For comparison purposes, the MSE for all the developed ANNs are shown in Table (5.1), the bold numbers refer to the least obtained mean squared error.

Table (5-1) Mean squared error for each ANN models.

Training Group1										
Number of neurons in hidden layers	Training strategy									
	Individual output parameters						Overall output parameters			
	d2/d1 (MSE)		E2/E1 (MSE)		E3/E1 (MSE)		d2/d1 (MSE)		E2/E1 (MSE)	E3/E1 (MSE)
6	0.0119		5.2e-07		3e-06		0.1098		2 e-04	4e-04
12	0.004	0.0009*	1 e-06	1e-06*	5e-06	2e-06*	0.1649		4 e-05	1e-04
	0.00081**		1e-06**		1e-07**					
24	0.0324		1e-06		4e-06		0.0427		2e-04	7e-04
48	0.01		3.2e-04		2e-03		0.8		2.3e-2	5e-2
Training Group2										
Number of neurons in hidden layers	Training strategy									
	Individual output parameters									
	d2/d1 (MSE)				E2/E1 (MSE)			E3/E1 (MSE)		
6	0.018				5.2e-05			6e-06		
12	0.0018		0.00008*		6.4e-07		5e-07*		1.4e-05	1e-05*
	0.000072**				3e-07**			1e-02**		
24	0.00824				5e-05			4e-06		
48	0.03				3e-04			2e-03		
Training Group3										
Number of neurons in hidden layers	Training strategy									
	Individual output parameters									
	d2/d1 (MSE)		d3/d1 (MSE)		E2/E1 (MSE)		E3/E1 (MSE)		E4/E1 (MSE)	
24	0.009		0.05		0.03		0.009		0.008	
48	0.00303		0.021		0.008		1.4e-02		5e-3	
60	0.00224	0.0001*	0.0054	7e-05*	0.0019	8e-04*	6e-04	1e-04*	8 e-04	6e-04*
72	0.004		0.009		0.004		8e-04		1e-03	
75	0.0045		0.005		0.006		0.006		0.008	

Training Group4										
Number of neurons in hidden layers	Training strategy									
	Individual output parameters									
	d2/d1 (MSE)		d3/d1 (MSE)		E2/E1 (MSE)		E3/E1 (MSE)		E4/E1 (MSE)	
24	0.01		0.07		0.03		0.01		0.008	
48	0.008		0.021		0.004		1.4e-02		5e-3	
60	0.00129	0.0001*	6e-05	4e-05*	9.8e-04	1e-04*	1 e-04	5e-05*	5e-04	4e-04*
72	0.006		3e-03		6e-03		3e-03		5e-03	
75	0.0045		1.5e-03		4e-03		2e-03		2e-03	

*MSR for ANNs models using training set with two different frequency steps.

**MSR for ANNs models using individual dispersion curve database.

5-5 Validation of the ANN Performance Using Numerical Data

The performance of the developed ANN was validated numerically by using a new input data set, which was not used previously in the ANN training or testing steps. Four new tested cases and their required input data (i.e. dispersion curve) were generated using ABAQUS and MATLAB. The four testing cases, as shown in the Figure (5-9), included: pavements with a single surface course and the base and subgrade softer than the surface layer (Cases 1 and 2), a four-layer pavement with a two-course surface layer, with a stiffer upper course and the base layer trapped between two softer layers (Case3), and a four-layer pavement with a two-course surface layer, with a stiffer lower layer and the base layer trapped between two harder ones (Case4).

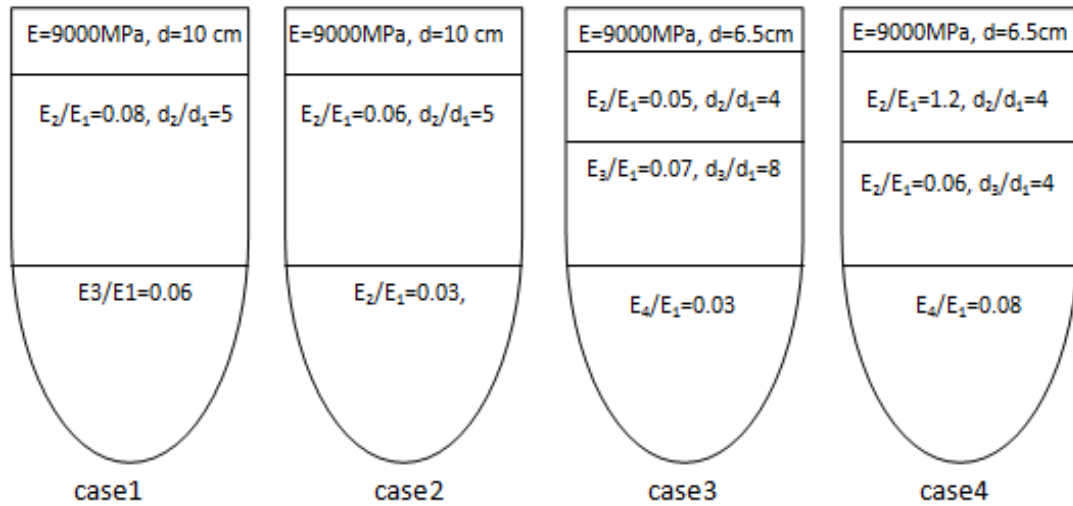
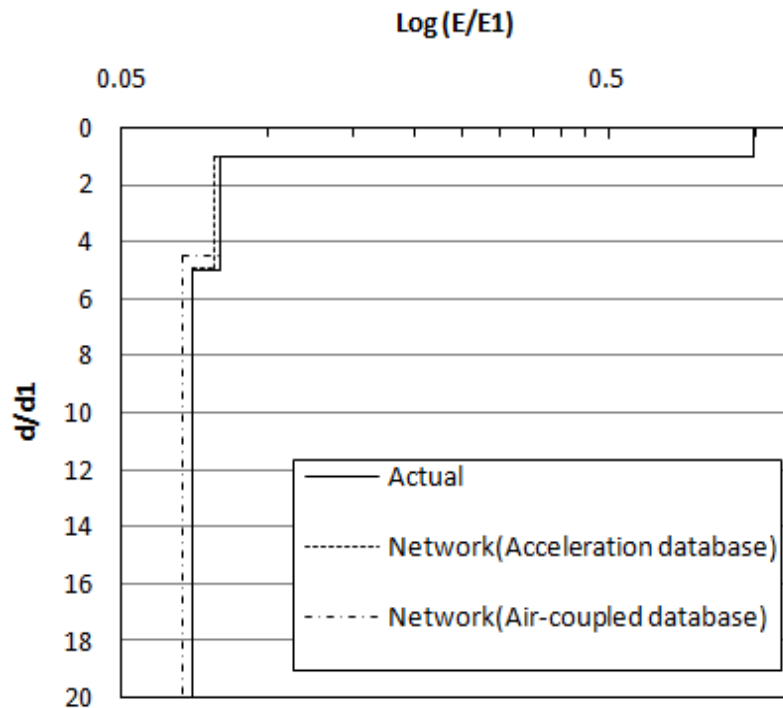
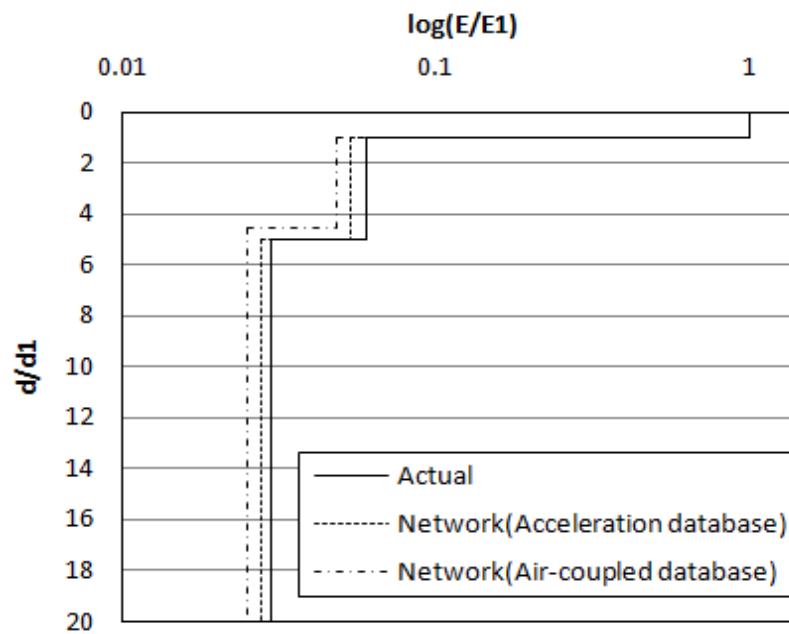


Figure (5-9) Four tested cases of pavement profiles

Figures (5-10) to (5-13) provide comparisons between the actual profiles and profiles backcalculated by ANNs for the four tested cases using different training strategies, as discussed earlier in sec.(5-6-1). Overall, these figures indicate that the ANN models varied in their ability to predict the pavement profile cases. The ANN models with the best prediction and give the closest match with the actual thicknesses (d_i/d_1) and the elastic moduli (E_i/E_1) parameter ratios is the one that trained based on individual dispersion curves identified by two frequency steps.

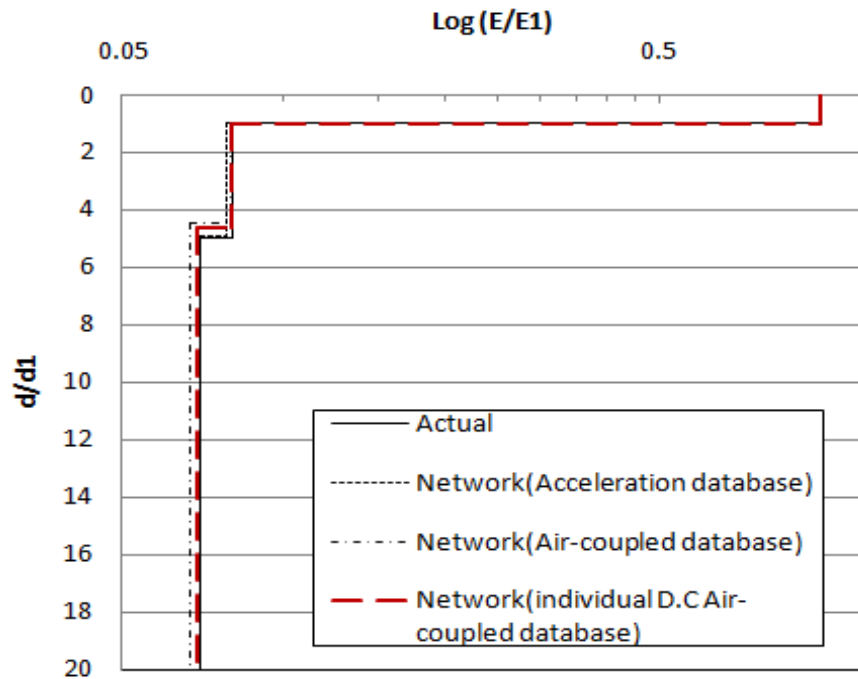


(a)

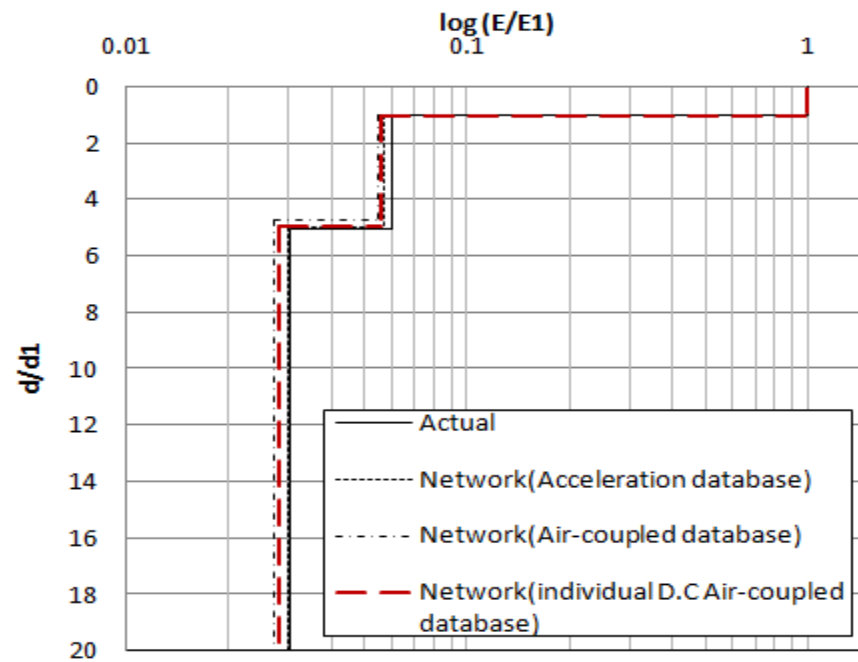


(b)

Figure (5-10) Comparison of actual profiles and output from ANN models for three-layer pavement profiles trained with fixed frequency steps: (a) test case1, (b) test case2



(a)



(b)

Figure (5-11) Comparison of ANNs Models output for three layers pavement profile trained with two different frequency steps: (a) test case1, (b) test case2

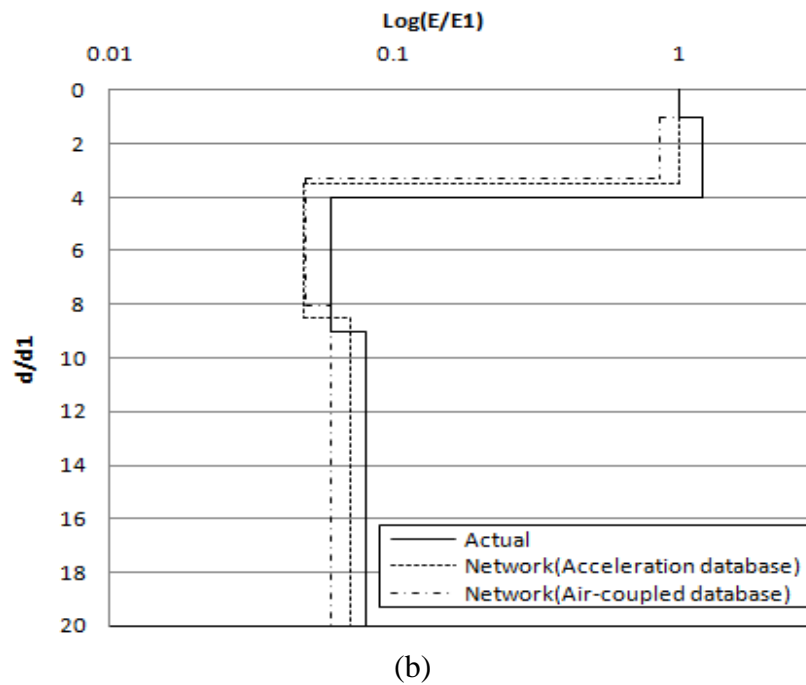
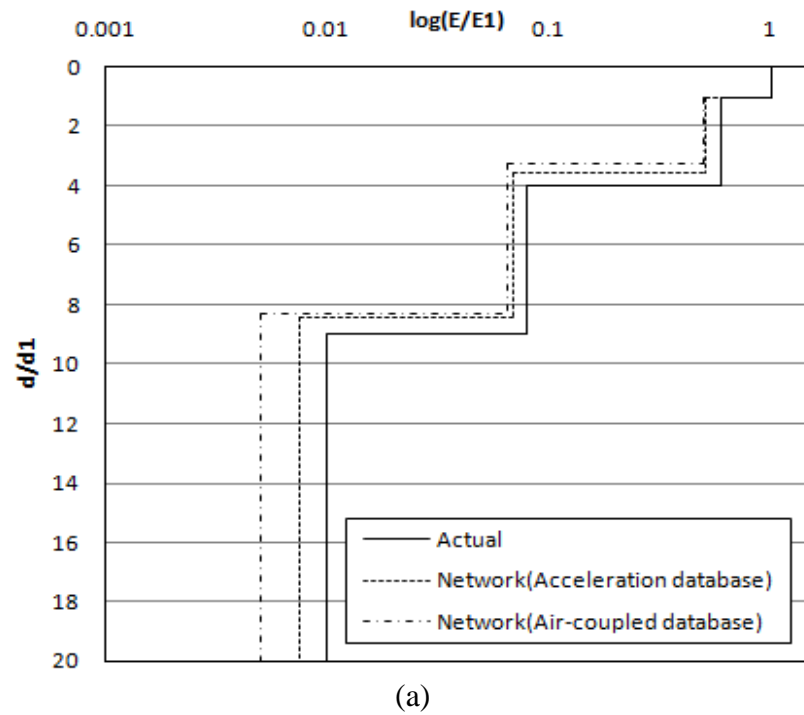
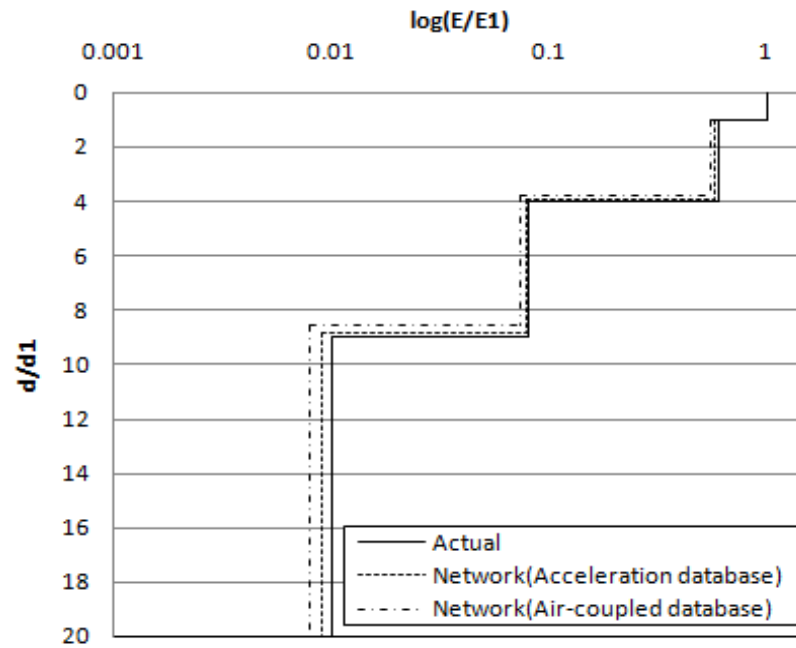
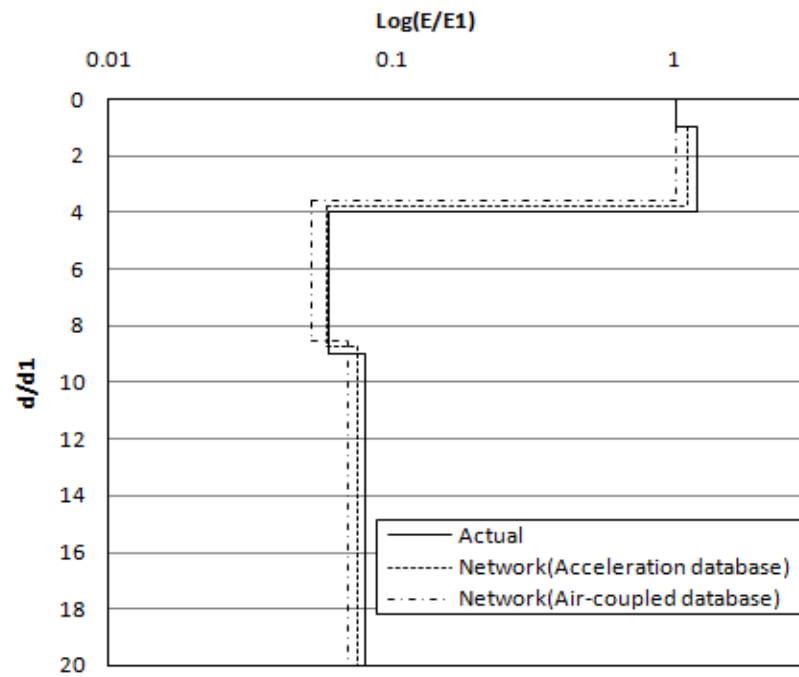


Figure (5-12) Comparison of ANNs Models output for four-layer pavement profiles trained with two different frequency steps: (a) test case3, (b) test case4



(a)



(b)

Figure (5-13) Comparison of ANNs Models output for four-layer pavement profiles trained by two different frequency steps: (a) test case3, (b) test case4

5-6 Conclusions

According to the numerical validation results, which were presented in previous figures, the recently developed ANN models based on air-coupled database gave a satisfactory accuracy and can predict pavement profile accurately enough for practical applications. However, some differences can be observed in cases when the shear wave velocity of base, and subgrade layers were low, reaching the speed of acoustic wave in the air.

Furthermore, the ANN models that were trained based on dispersion curve input points with two different frequency steps gave a perfect match between the actual and predicted pavement profile. Also, the ANN models based on the individual receiver spacing training approach enhanced the network model profile detection with respect to the average dispersion curve approach.

CHAPTER SIX

Field Implementation of Air-Coupled SASW Test

6-1 Introduction

The experimental phase of this research included implementation of the air-coupled SASW test. The test results were used to further evaluate and verify the developed ANN models. Four musical microphones were used to detect the leaky surface waves that propagate out of the pavement system surface. As demonstrated by Zhu and Popovics (2008), these microphones work very well in the field to develop the leaky surface wave dispersion curves. This chapter describes the field implementation of air-coupled SASW testing, including the test setup, data acquisition system, and the signal processing. Most importantly, it describes the verification of developed ANN models.

6-2 Air-coupled SASW Test System Description

The system used for the conduct of the SASW test includes two components: hardware and software platforms, as described below:

6-2-1 Hardware Platform Integration

Four air-coupled sensors (regular cardioids musical microphones) were used, which were the most cost-effective selection for this application. The properties of these microphones are: the polar pattern is a fixed cardioid, sensitivity is 10mV/Pa at-40dBV (re.1V/Pa), and frequency response range is 20 to 20 kHz. Detailed descriptions

regarding the field use of this type of microphone can be found in (Zhu and Popovics, 2008).

An aluminum 4-wheel cart was designed and built to hold the microphones. It was designed in a way so that the clearance between the microphones and the ground is adjustable. The spacing between the microphones is adjustable too. This enables the system to be adaptable to different ground surface profiles. Preliminarily, the four microphones were set at distances of 0.1, 0.2, 0.4 and 0.8 m from the source. A schematic view of the built air-coupled SASW testing system is shown in Figure (6-1). An automated, solenoid-type, impact hammer was designed to provide an impact force of a needed power within a required frequency range. The design of the automated impact hammer included an actuator to generate the force for the impact, an impact tip, a control circuit to drive the actuator, and a housing to protect and support the mentioned components.

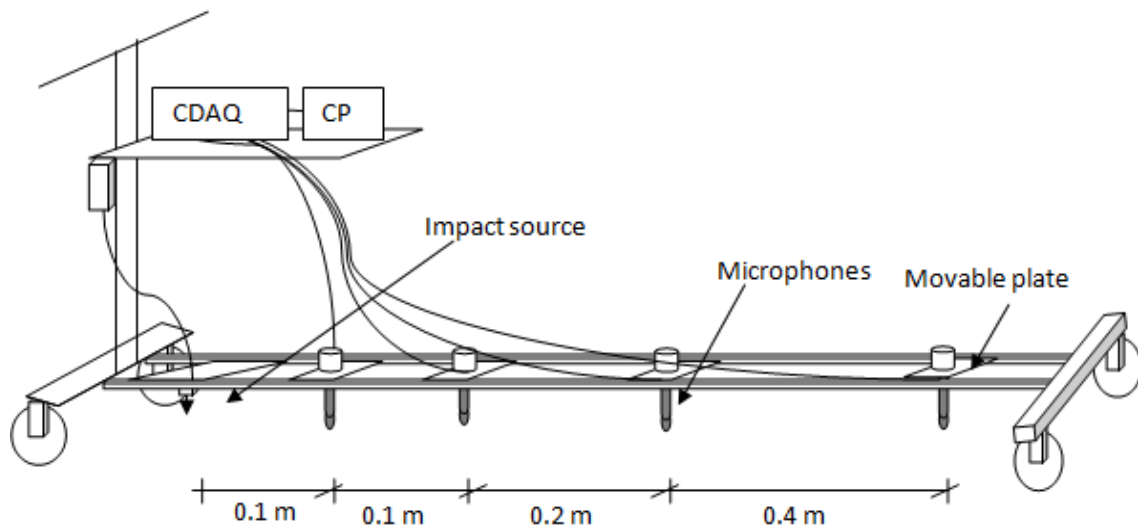


Figure (6-1) Schematic view of the built non-contact SASW testing system

For signal digitizing and acquisition, a Compact Data Acquisition System (cDAQ) was used. The cDAQ required parts were supplied by National Instruments (NI) Company. Those include Module BNC:NI 9234 (4 Input, 24-Bit, 51.2 kS/s) and Chassis cDAQ-9174 (4 slot USB), in addition to all other the system's accessories, such as NI PS-15 Power Supply (24 VDC, 5 A, 100-120/200-240 VAC input), USB cable with one locked screw and desktop DC power supplies for Compact DAQ Chassis. The non-contact SASW testing system is shown in Figure (6-2).

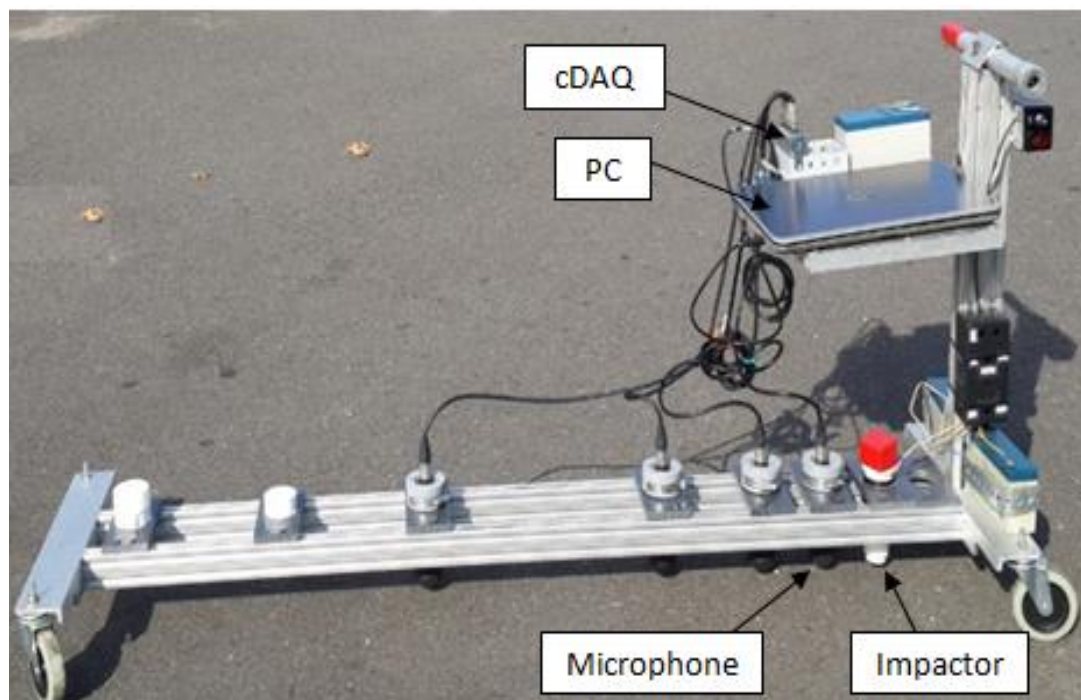


Figure (6-2) Air-coupled SASW testing system hardware components

6-2-2 Software Platform Integration

An NI LabVIEW-based computer program was developed for configuring the data acquisition parameters, such as the sampling rate, sampling length, trigger type, and trigger level. The program's introduction is shown in Figure (6-3). The acquired signals were analyzed under the developed MATLAB program framework. The obtained experimental dispersion curves were saved for further validation of the ANN developed models.

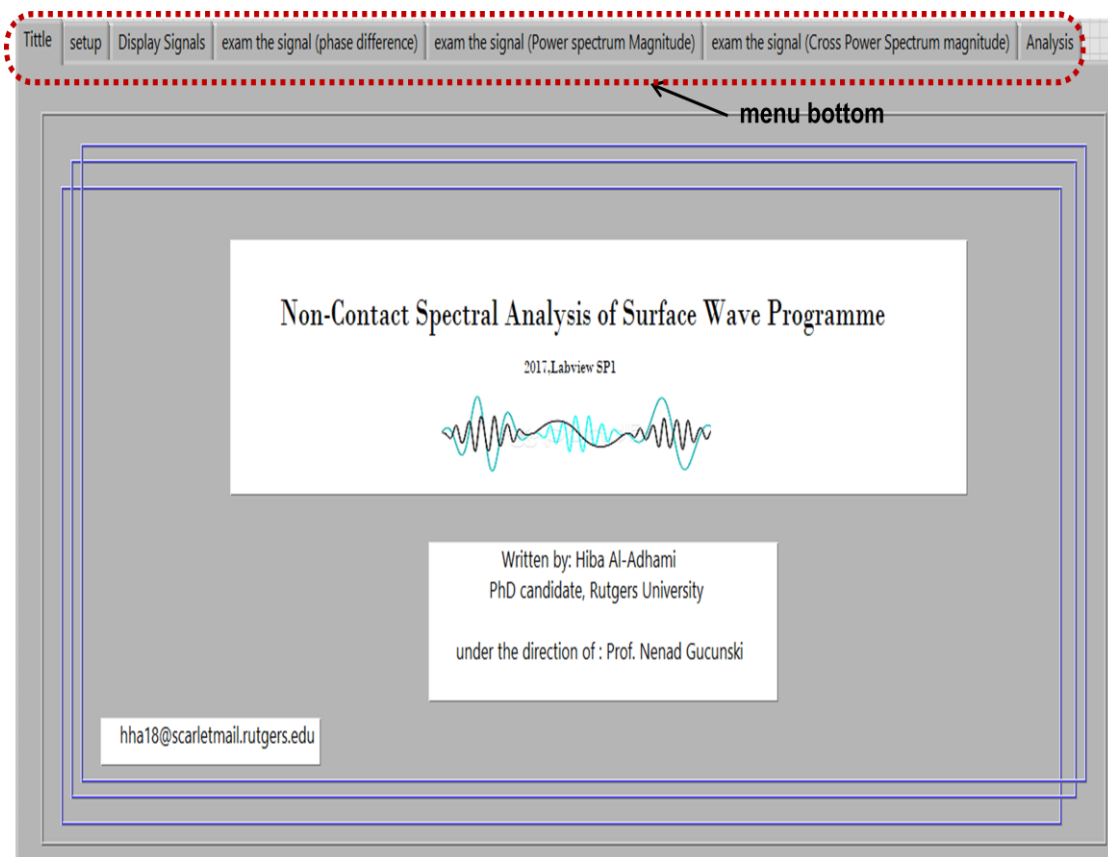


Figure (6-3) The intro page of the computer program for control of the non-contact SASW test

In general, the LabVIEW program includes four sections as explained below:

- (1) Setup section: includes the user interface to set the data acquisition parameters, such as the sampling rate, the sampling length, the analog input channel numbers and the trigger channel.
- (2) Display section: includes the interface for presentation of waveforms captured by the sensors in the time domain.
- (3) Examination section: includes tools for checking the consistency of the received signals, most importantly the signals' phase differences, the cross power spectra magnitude, and the coherence. The signals are examined using the tools and are either saved or discarded.
- (4) Analysis section: includes the dispersion curves calculation and presentation under the MATLAB program framework. In addition, the database (i.e. dispersion curve points) is extracted and saved in this section. Figure (6-4) provides screenshots for each of the four program sections during the preliminarily investigated test, while Table (6-1) provides descriptions for each input parameter in the signal measurement.

Title Setup Display Signals exam the signals (Phase Difference) exam the signals (Power Spectrum Magnitude) exam the signals (Cross Power Spectrum Magnitude) Analysis

A) Aqazition Setting:-

physical channels 1
 number of samples per channel 2
 Sampling Frequency, fs (Hz) 3

Condition 4
 Pretrigger Samples 5
 Window Amplitude / Hysteresis 6

Channel Name 7
 # Pretrigger Samples Acquired 8
 Elapsed Time 9
 Elapsed Time (s) - Loop 10

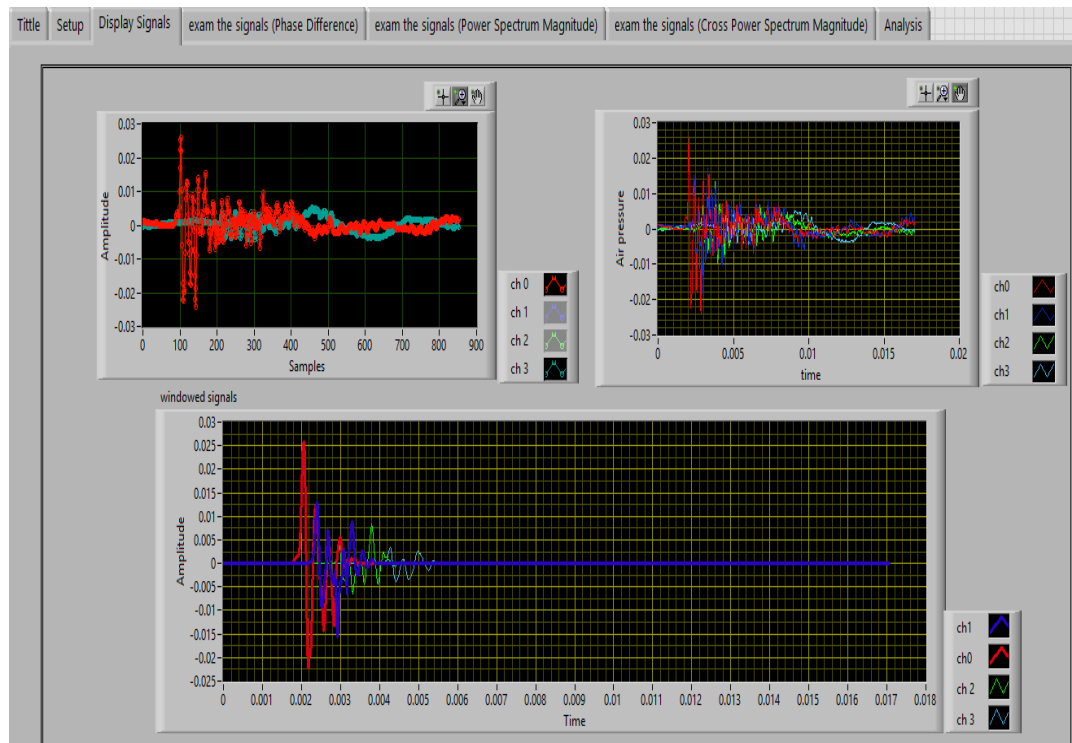
B) Configuration Settings:- 14

X0 11
 X1 12
 X2 13
 X3 13

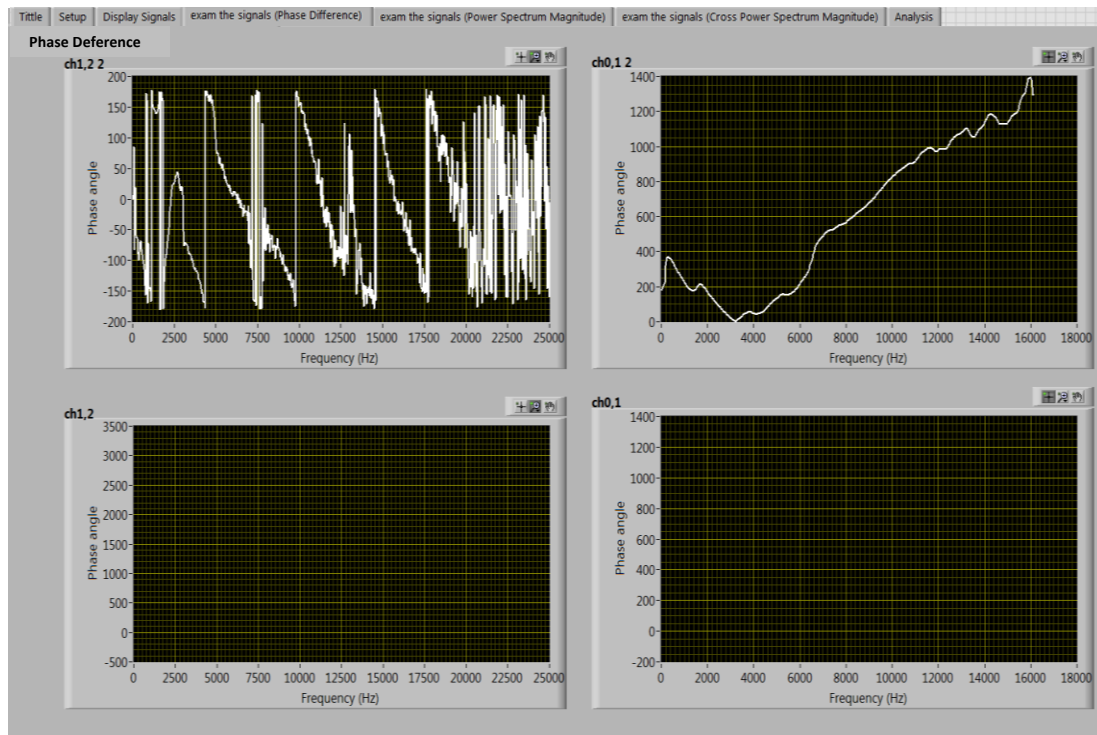
OK Button

15
 16 Error Indicator
 (Indicates if trigger occurs before pre-trigger samples were)

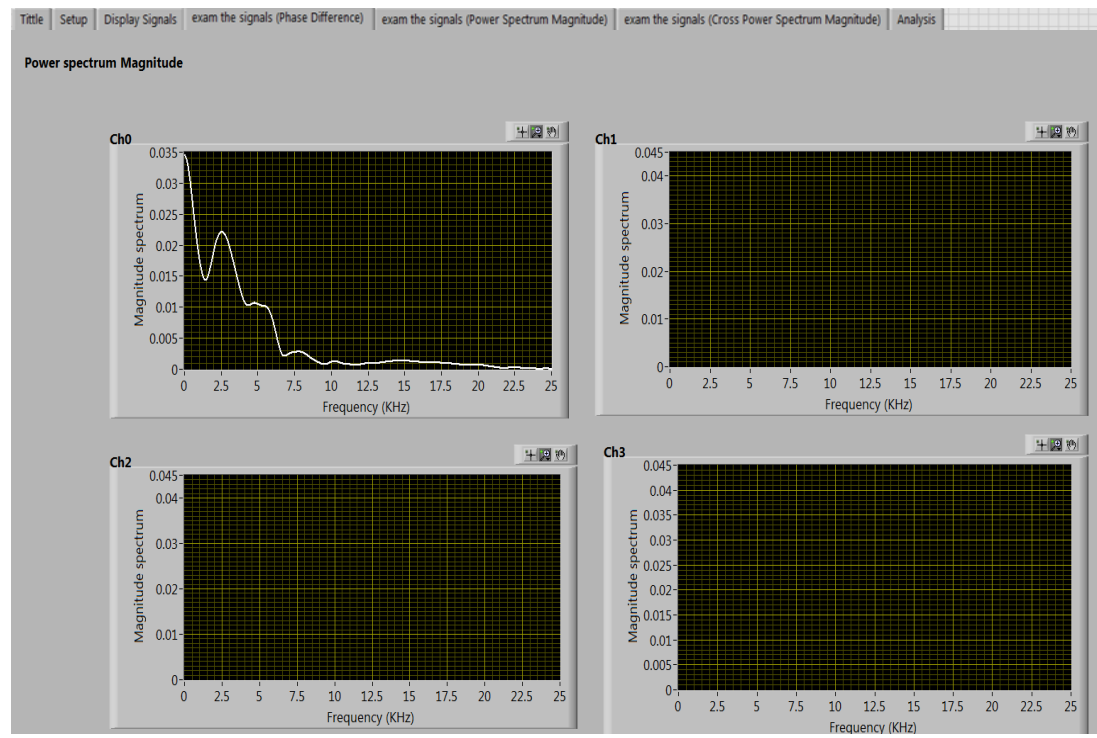
(a)



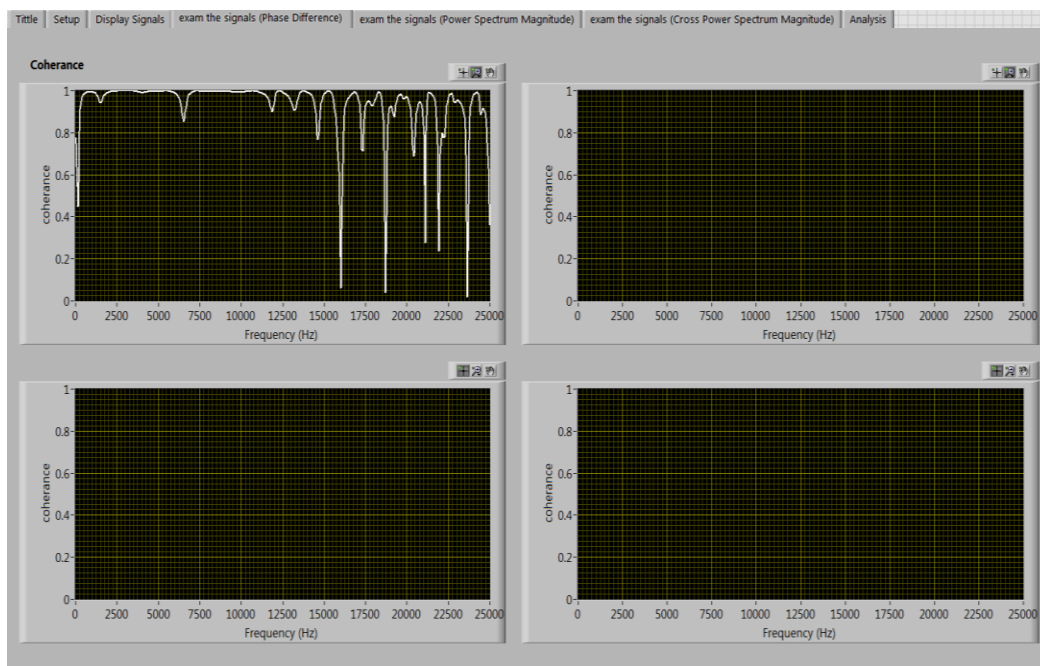
(b)



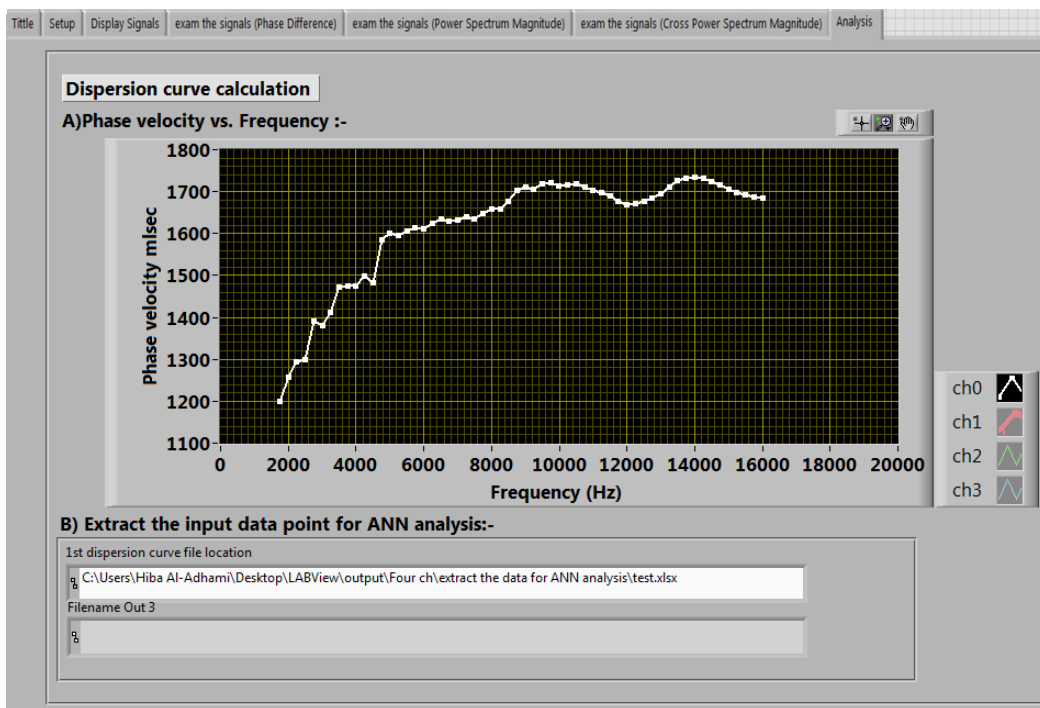
(c)



(d)



(e)



(f)

Figure (6-4) LabVIEW program's four sections (a) setup, (b) display, (c) examination of signal's phase difference, (d) examination of the auto power spectra magnitude, (e) examination of coherence and (f) analysis sections.

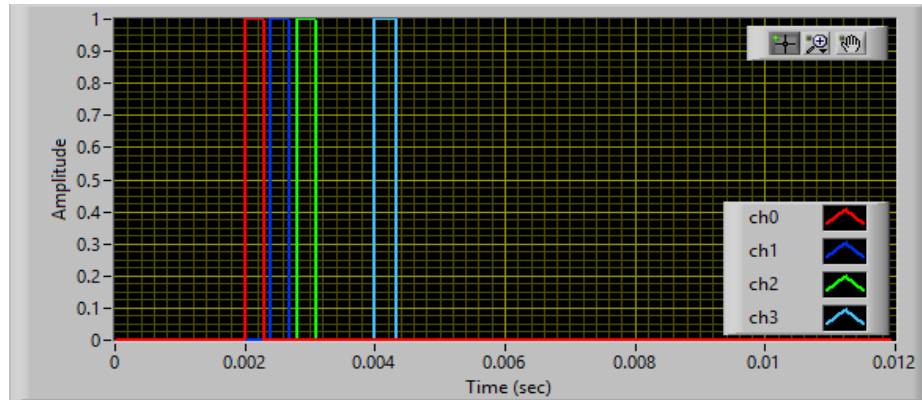
Table (6-1) Summary of input parameters for data collection

Setting Section	
A) Data Acquisition Settings	
(1)	Control of active channels
(2)	Number of samples per channel
(3)	Sampling frequency
(4)	Condition of acquiring the samples: above or below the threshold
(5)	Control of the number of samples of pre-trigger
(6)	Window amplitude
(7)	Control of the triggering channel
(8)	Indicator of the number of samples acquired
(9)	Indicator of the elapsed time
(10)	Indicator of the elapsed time in loop
(11)	Channel index
(12)	The threshold or level to start acquiring the data
(13)	Control of the time delay to start data acquisition
B) Sensor Configuration Settings	
(14)	Definition of distance between the four sensors and the impact source
(15)	Stop button to terminate the signal data acquiring process
(16)	Error indicator, if the sampling occurs before the sample pre-triggering

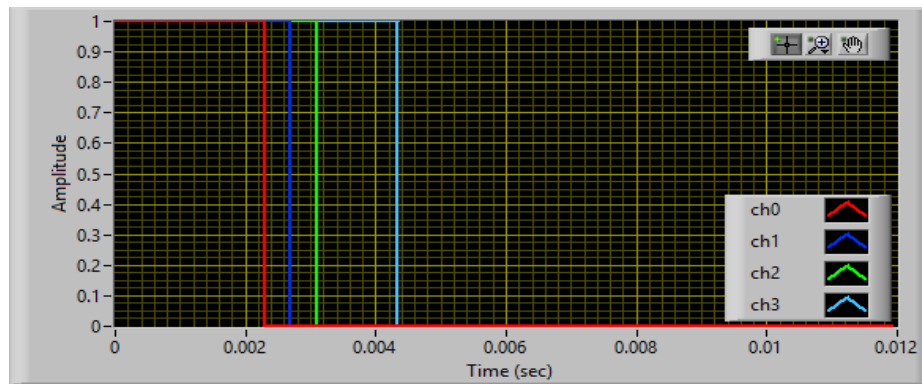
6-3 Extraction of Radiating Surface Wave Signals

As mentioned in Chapter 3 and 4, the non-contact sensors detect both radiating and direct waves. The radiating surface waves (i.e. leaky Rayleigh waves) can be extracted from the intact acoustic signal by applying an appropriate time-window. In this study, different designs of time-window were investigated to ensure quality of the extracted radiating signal for each microphone. The bin-band pass, the bin-low pass and the exponential time-window designs were considered in the investigation. Bin-band pass time-window allows time domain data between two specific time arrival ranges in the analysis and eliminates the data before and after this range. On the other hand, bin-low pass time-window allows time domain data before a specific time arrival value in the analysis, while the exponential one allows time domain data after a specific time arrival value in the data analysis with a gradual cut (exponential cut).

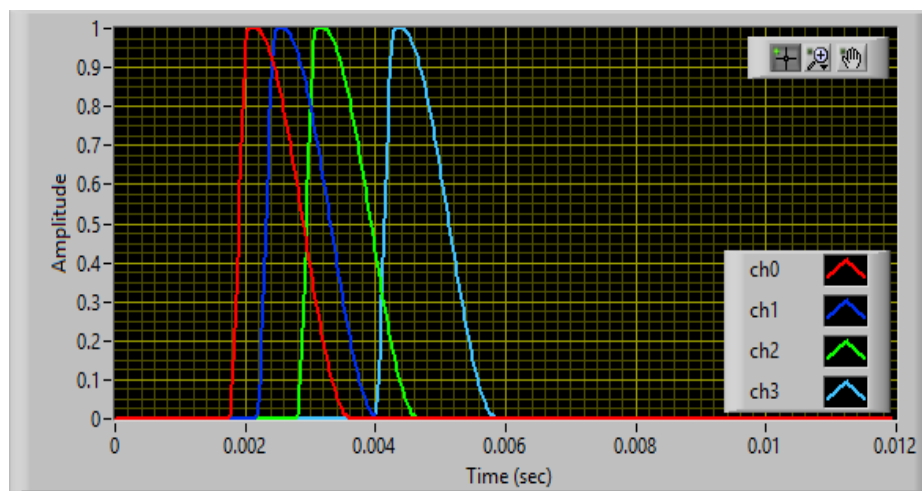
The window center was applied on the first peak that appears in the recorded acoustic data. This peak was identified as the arrival time of the radiating surface wave. The size of each window was considered equal to the arrival time difference from the radiating surface wave to the direct acoustic wave. The estimation of time arrival difference was discussed previously in Chapter 3. Each time-window was shifted according to the arrival time of each signal. Figure (6-5) illustrates the different time-windows that were investigated within the LabVIEW environment.



(a)



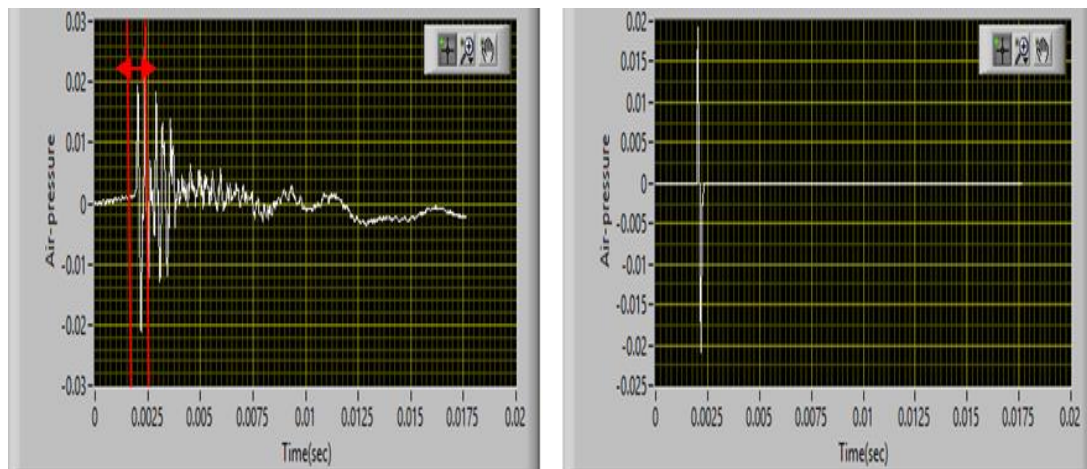
(b)



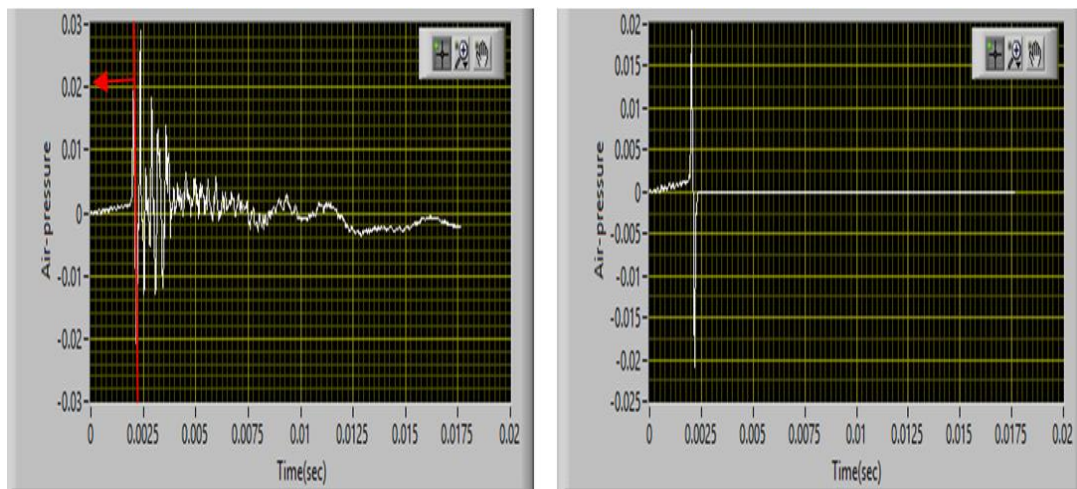
(c)

Figure (6-5) Different Time-window designs (a) bin-band pass, (b) bin-low pass and (c) exponential

Figure (6-6) illustrates an example of the raw and windowed signals by applying different time-window designs. It can be noticed from the illustration that the bin-band pass and the din-low pass apply sharp cuts to both ends of the waveform and will likely distort the frequency information and alter the phase information. Unlike that, the exponential time-window apply a gradual cut which allows extracting the leaky surface waves without missing any dispersion features of the tested pavement profile that these waves bring. Therefore, the exponential time-window was selected.



(a)



(b)

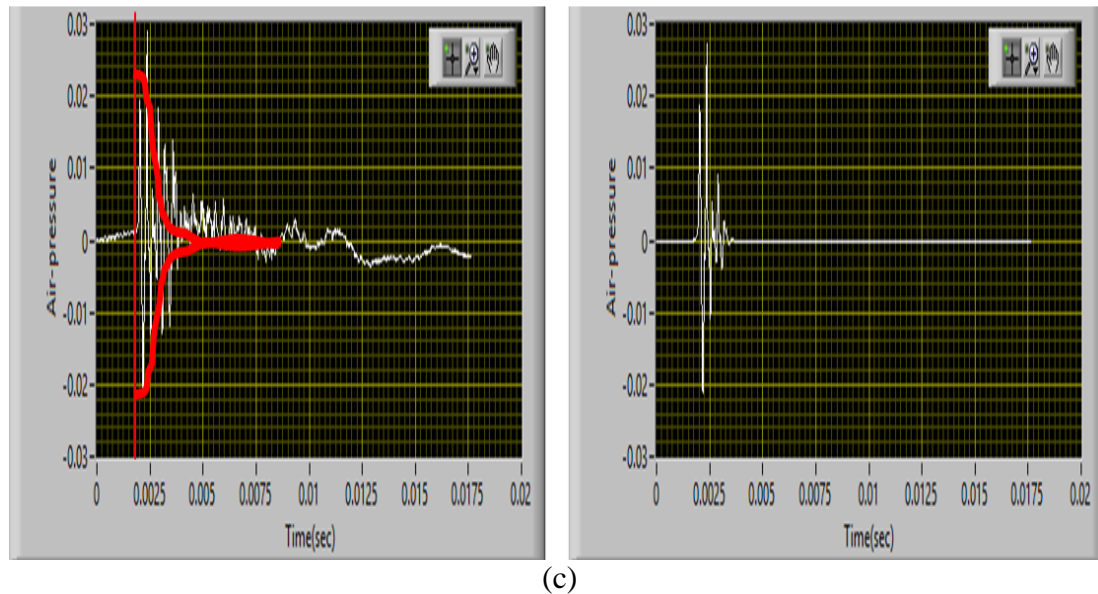


Figure (6-6) Leaky surface wave's extraction from the first receiver signal. Raw signal (right), windowed signal (left) by applying (a) bin-band pass, (b) bin-low pass and (c) exponential time-window.

6-5 Verification of Components of the Integrated System

A series of tests were done to verify performance of components of the integrated built-up system, with respect to the acquired signal quality. The investigation also included the assessment of performance of the impact source. Preliminarily, a special portable impactor was manufactured to eliminate possible transfer of vibrations from the cart, and further to the microphones. The impact, or the pulse load, was verified through the examination of the shape of time histories of the received signals. Only sharp impacts with a broadband excitation were accepted (i.e., sufficiently large amplitude frequency components are excited in the frequency range of interest).

To compare the obtained experimental dispersion curves based on the contact and non-contact sensors, two accelerometers with spacing $x=0.2\text{m}$ were placed beside the microphones, as shown in Figure (6-7). A very thin layer of glue was used to attach them.

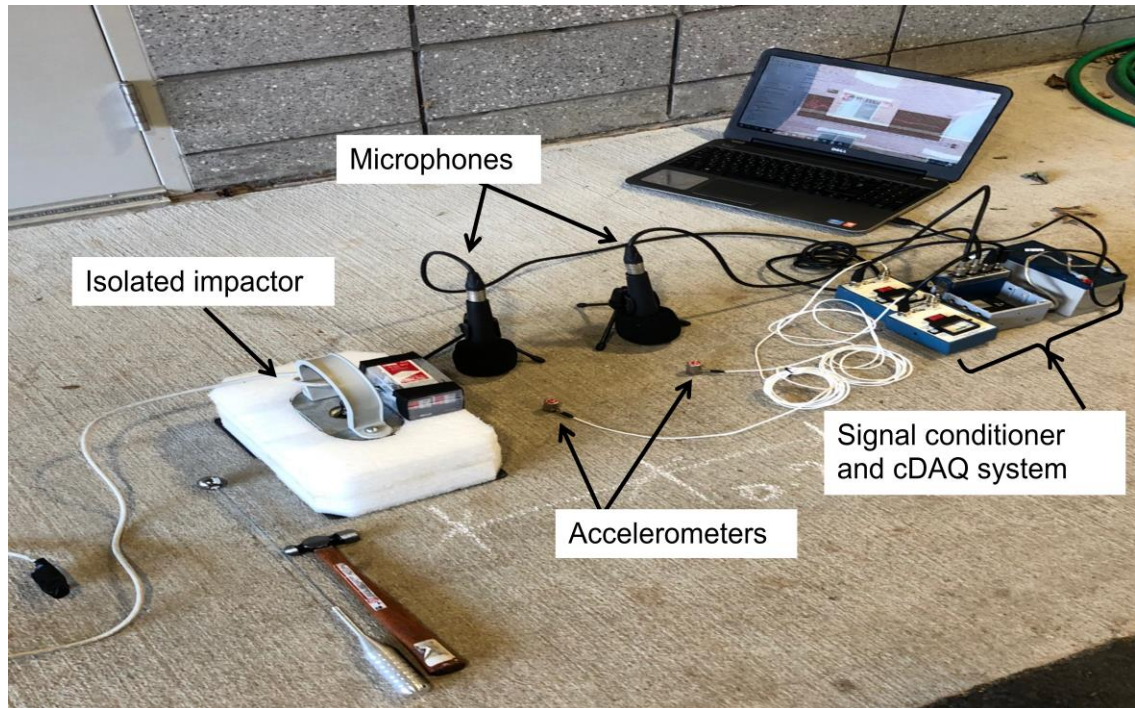


Figure (6-7) Implemented contact and non-contact SASW testing on a concrete floor

The properties of the accelerometers were: mass= 10 grams, nominal voltage acceleration sensitivity= $10 \text{ mV}/(\text{m/s}^2)$, frequency response range= 1-10000 Hz, resonant frequency $>36 \text{ kHz}$. A typical low-frequency response for the used contact accelerometers is shown in Figure (6-8). The test was done on a single-layer concrete floor (i.e. constant shear wave velocity profile, or non-dispersive profile) to ensure that only one material's information will be inverted.

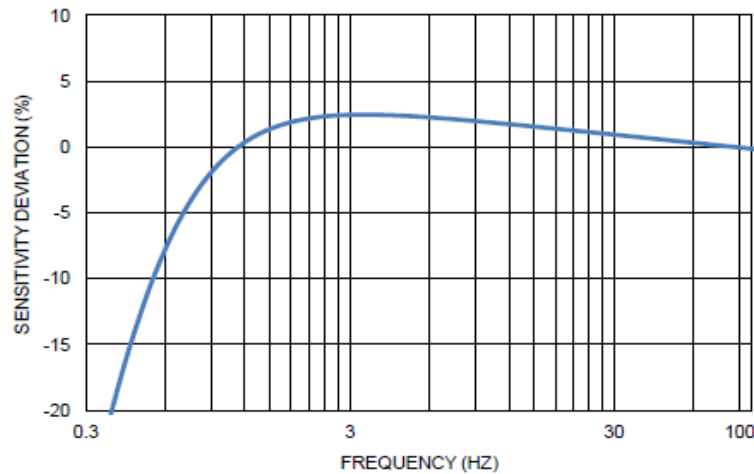


Figure (6-8) Low frequency response for the used contact accelerometers

Only the signals of good quality can be used in the dispersion curve calculation, as explained previously in Chapter3. An average of multiple records; no more than 5 measurements, were considered to calculate the coherence function. Additional measurements do not contribute to a better-quality measurement (Heisey et.al, 1982). The LabVIEW user interfaces to collect data using accelerometers and microphones are shown in Figures (6-9) and (6-10), respectively. The data acquisition parameters were set through the setup section as explained earlier, such as the number of sample per channel was 1024 S/ch, the sample frequency was 50 kS/ch/s and the receiver spacing was 0.2m for further analysis.

It can be noticed that the value of magnitude-squared coherence was between 0 and 1, where 1 indicates a perfect coherence, while less than 0.9 indicates a poor coherence. The poor coherence is caused by uncorrelated signals, poor resolution, system nonlinearities or noise ([Heisey et.al, 1982](#); [Opra et.al, 1996](#)). The signals or parts of signals, with poor coherence were filtered out of the dispersion curve calculation.

Title Setup Display Signals exam the signals (Phase Difference) exam the signals (Power Spectrum Magnitude) exam the signals (Cross Power Spectrum Magnitude) Analysis

A) Acquisition Setting:-

physical channels
 cDAQ1Mod1/ai0:1

number of samples per channel
 2048

Sampling Frequency, fs (Hz.)
 50000

Condition
 Above Level

Pretrigger Samples
 100

Window Amplitude / Hysteresis
 500.00m

Channel Name

Pretrigger Samples Acquired
 0

Elapsed Time
 0

Elapsed Time (s) - Loop
 0

B) Configuration Setting:-

X0 X1 X2 X3

X0 0.2
 X1 0.2
 X2 0
 X3 0

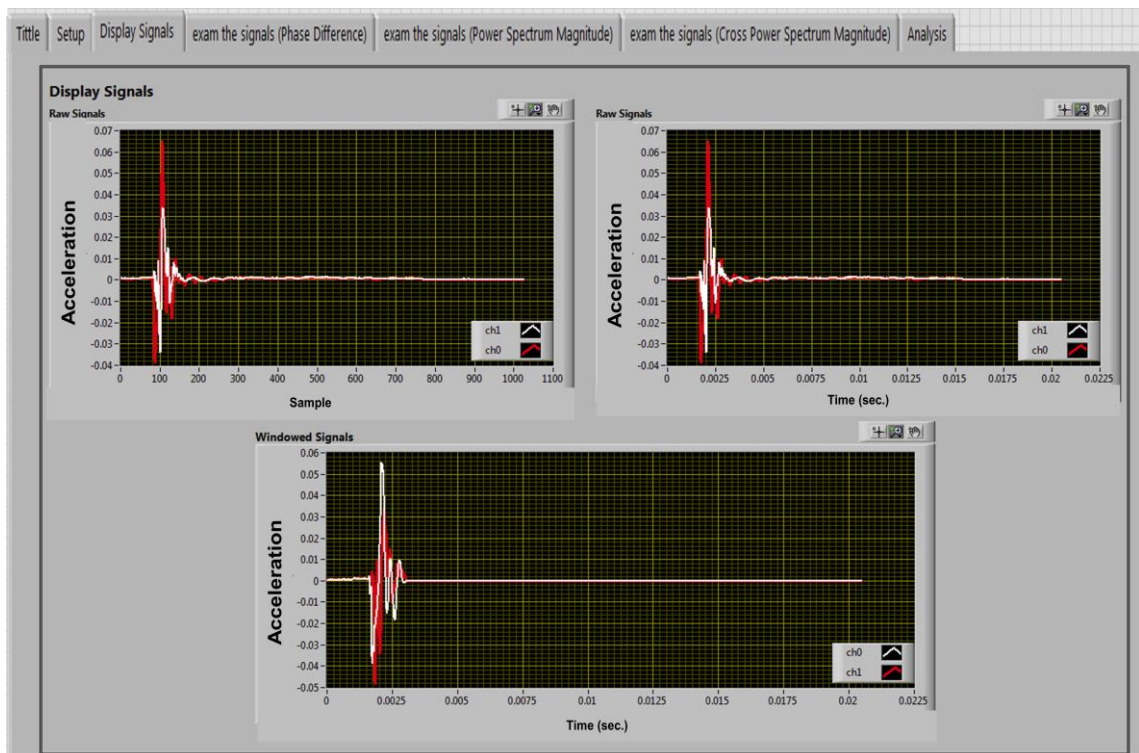
OK Button
 OK

STOP

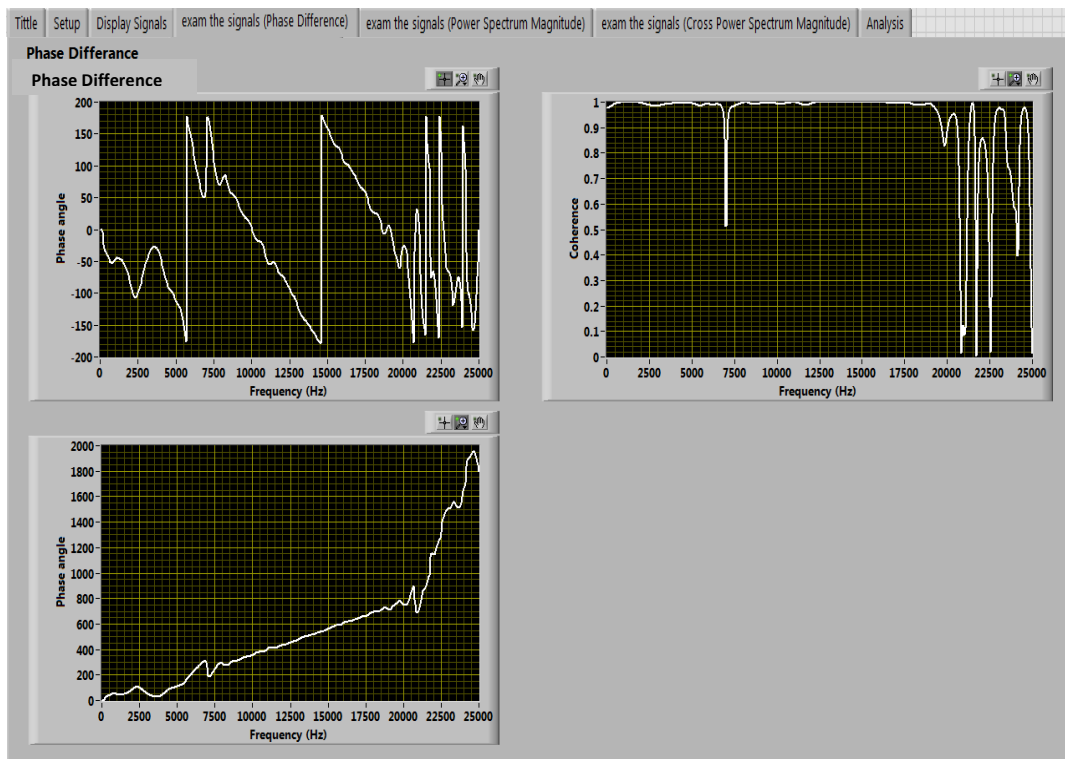
Error Indicator
 (Indicates if trigger occurs before pre-trigger samples were)

Ok

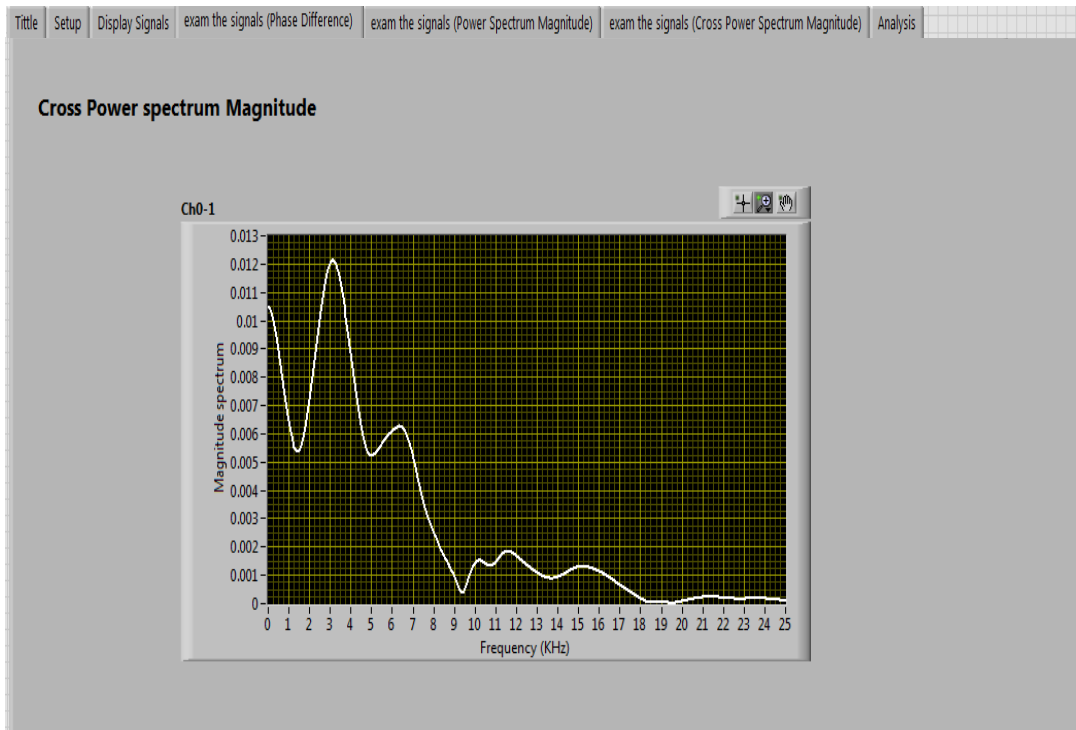
(a)



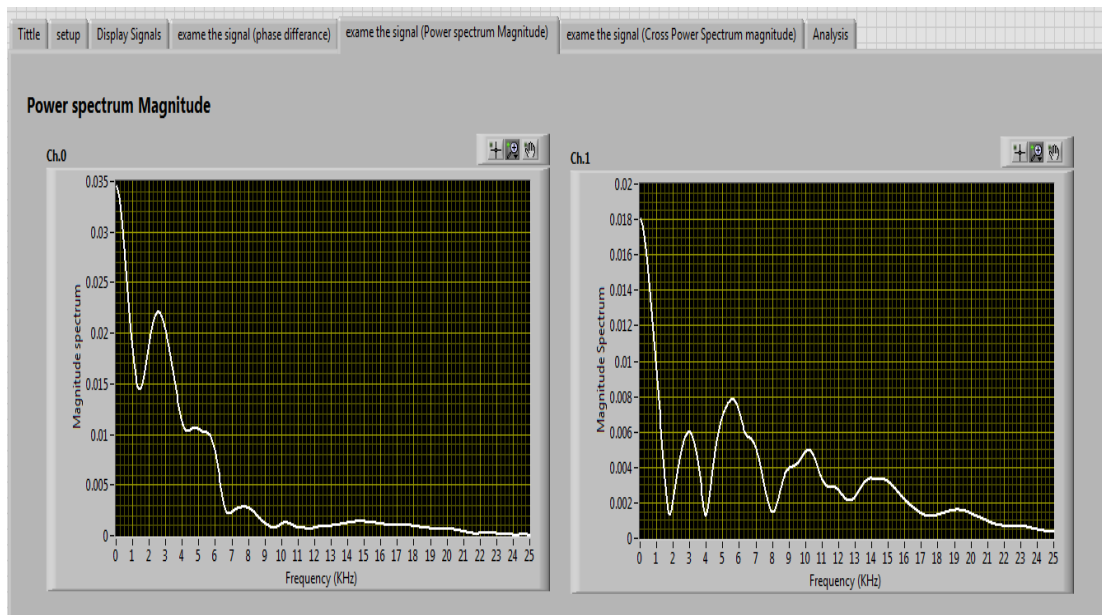
(b)



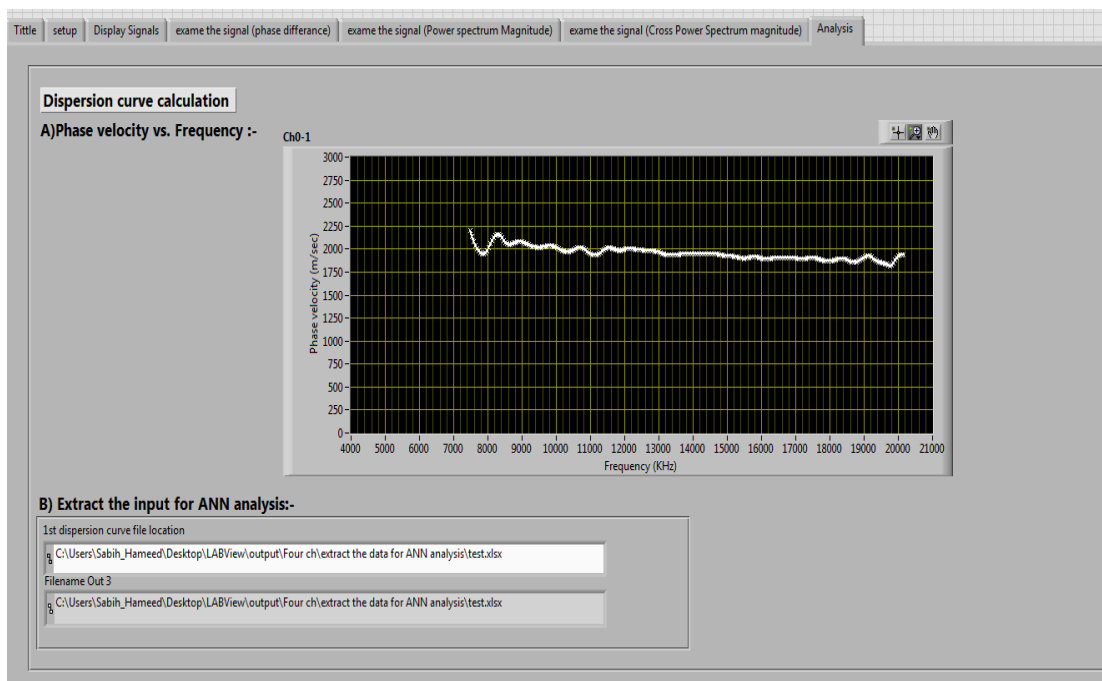
(c)



(d)



(e)



(f)

Figure (6-9) LabVIEW user interface for data collection and analysis based on contact sensors (accelerometers): (a) setting of the parameters, (b) display of saved signals, (c) cross power spectrum phase and coherence, (d) cross power spectrum magnitude, (e) auto-power spectrum magnitude, and (f) dispersion curve.

Title Setup Display Signals exam the signals (Phase Difference) exam the signals (Power Spectrum Magnitude) exam the signals (Cross Power Spectrum Magnitude) Analysis

A) Aquazition setting:-

physical channels
 cDAQ1Mod1/ai0:1

number of samples per channel
 2024

Sampling Frequency, fs (Hz)
 50000

Condition
 Above Level

Pretrigger Samples
 100

Window Amplitude / Hysteresis
 500.00m

Channel Name

Pretrigger Samples Acquired
 0

Elapsed Time (s)
 0

Elapsed Time (s) - Loop
 0

Channel Index
 0

Level
 0.002

timeout
 3.00

B) Configuration setting:-

X0 X1 X2 X3

X0 0.2
 X1 0.2
 X2 0.4
 X3 0

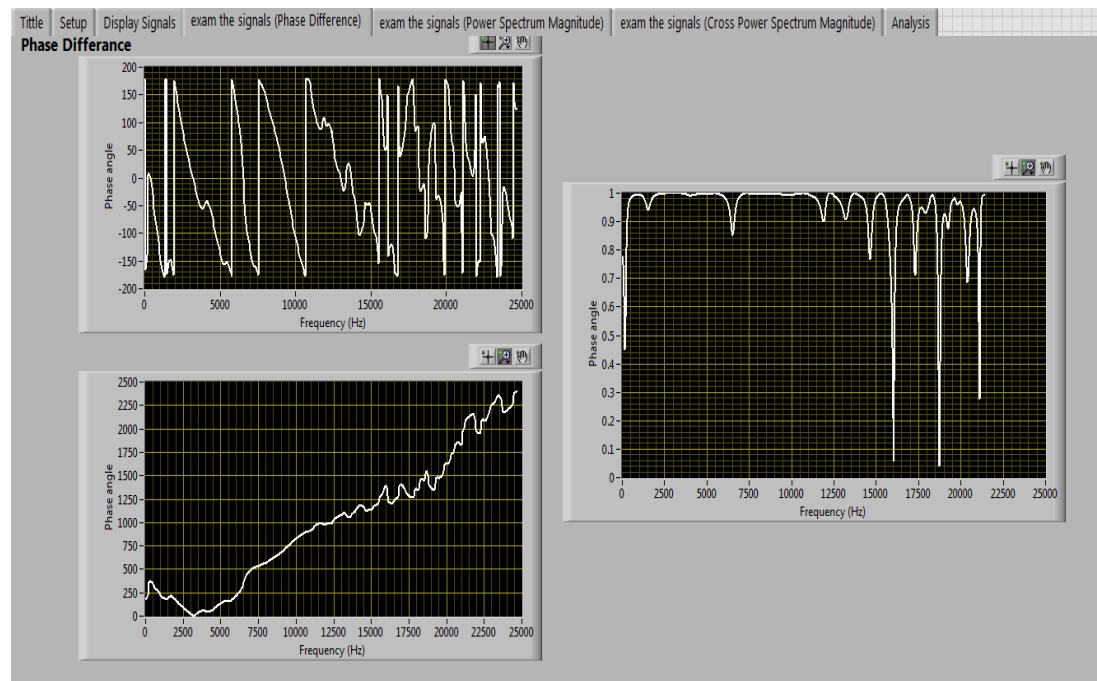
OK Button
 OK

STOP

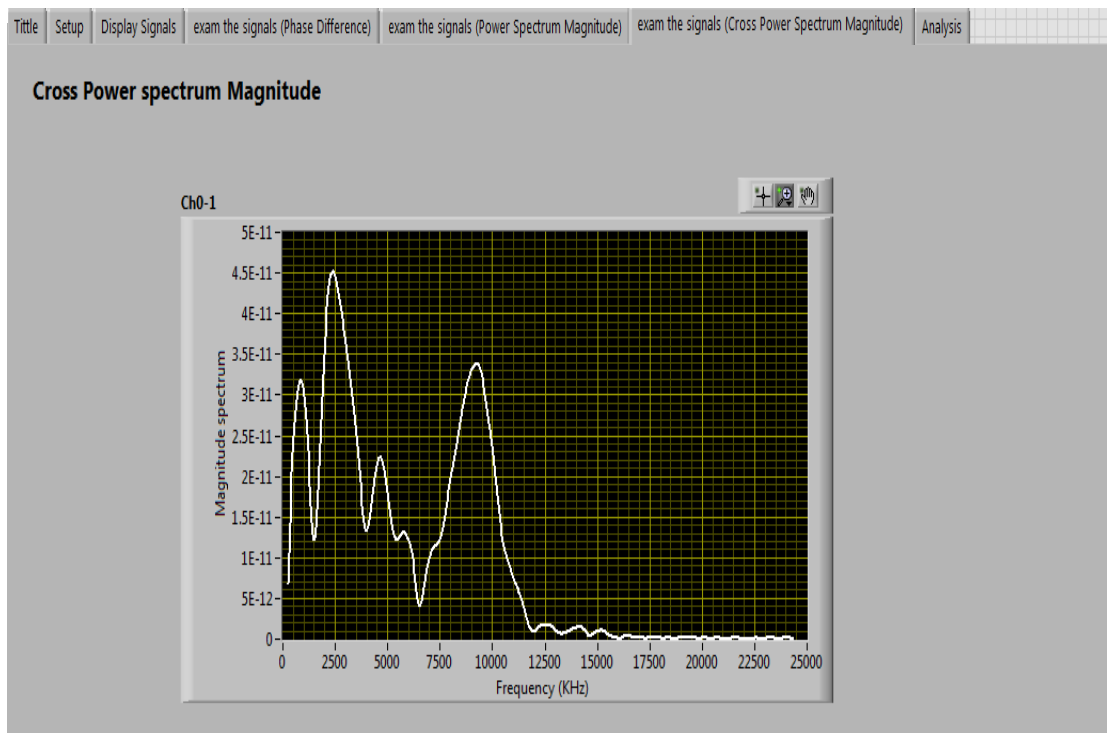
Error Indicator
 (Indicates if trigger occurs before pre-trigger samples were)

Ok

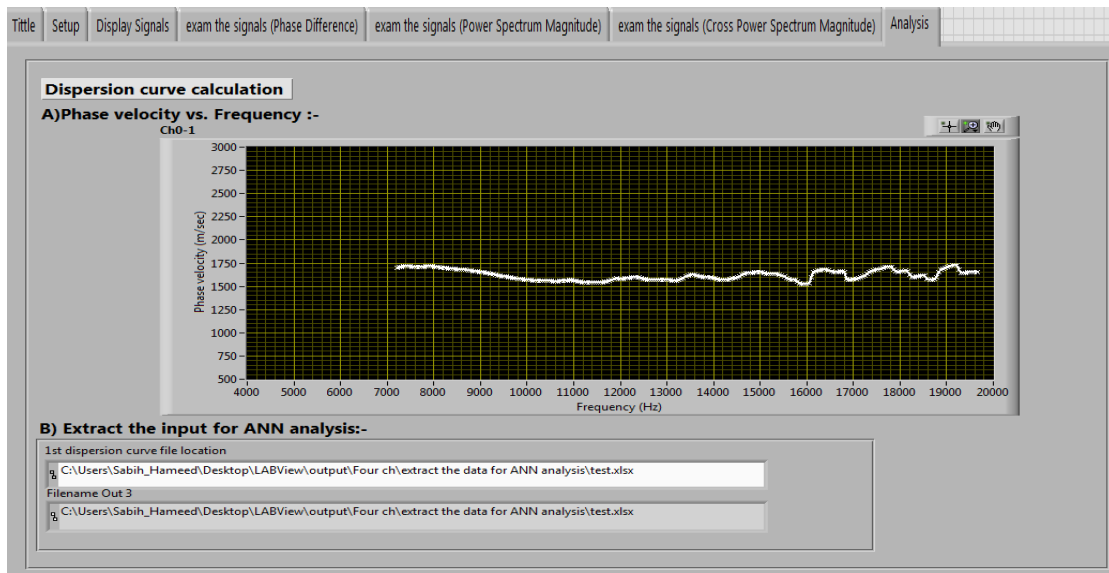
(a)



(b)



(d)



(e)

Figure (6- 10) LabVIEW user interface for data collection and analysis based on non-contact sensors (microphones): (a) setting of the parameters, (b) display of saved signals, (c) cross power spectrum phase and coherence, (d) cross power spectrum magnitude, (e) dispersion curve.

According to this preliminary investigation, it was shown that the surface wave dispersion curves which were obtained from contact and air-coupled SASW tests are not significant difference in estimating the phase velocity (i.e. apparent surface wave velocity) for the tested concrete structure. The percent of non-similarity between them is possibly due to the effect of body waves in the air-coupled signal are smaller than in the contact signal (Zhu and Popovics, 2008). This indicates that the microphones used are effective in capturing leaky surface wave, and that the system components work accurately.

Furthermore, it is noticed that the received signals by microphones have a low signal/noise ratio when they were set in the cart. The vibration of the cart when the load was acting was considered to be the main reason for this low ratio. Therefore, a professional grade damper or an isolator was used to isolate the microphones from the effect of cart vibrations induced by the applied load. Figure (6-11) provides an image of a signal obtained when the isolator was used. Moreover, the direct acoustic wave's effects can be eliminated by increasing the source-to-receiver spacing.

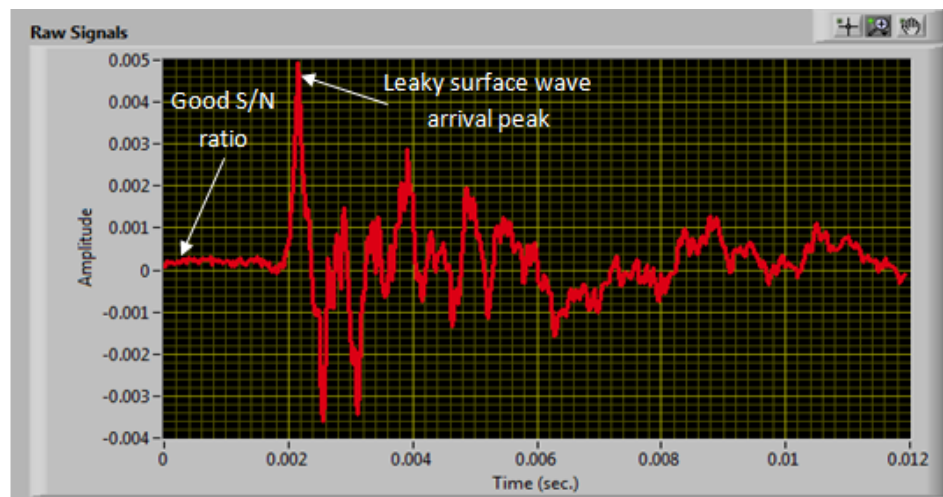


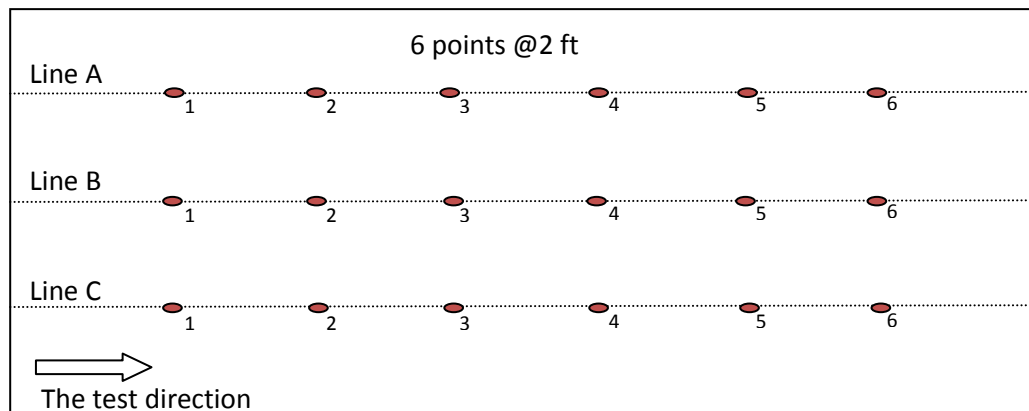
Figure (6-11) Detected signal by the microphone when the isolators was used

6-6 Validation of the ANN Performance Using Field Test Data

The developed automated system was tested and validated on a number of pavement sections located on Rutgers University campuses. The investigation included two different case studies. In first case study, an old constructed pavement with no ground truth information or design record was considered. The second case study included an investigation of a newly constructed pavement with record information, as explained below.

6-6-1 Case Study 1

The selected asphalt pavement sections were first tested using the GPR test, so that the pavement layers thicknesses can be identified. In addition, a portable seismic property analyzer (PSPA) was implemented to compare the elastic modulus of the surface layer with the one that was obtained directly from the dispersion curve. Evaluations by GPR and PSPA were explained previously in Chapter 3. Both tests were carried out on a pavement section of overall dimensions of 4ft by 8 ft. The GPR test layout included scanning along three lines with a clearance of 2ft to ensure that the entire pavement section was scanned. Each test line included 6 test points for implementation of PSPA and air-coupled SASW tests, as shown in Figure (6-12).



(a)



(b)

Figure (6-12) Case study1. (a) Field test layout, (b) GPR scanning.

The obtained GPR data is illustrated in Figure (6-13). According to the GPR B-scans; the tested points of each line were located within either thick AC layer side of 0.2m or within a thin AC layer side of about less than 0.1m. Only the tested points within the thicker side were considered in the validation of the ANN model's performance. The

tested pavement section included two layers: the AC surface layer and the base layer, with an estimated thickness of 0.2m and 0.3m, respectively.

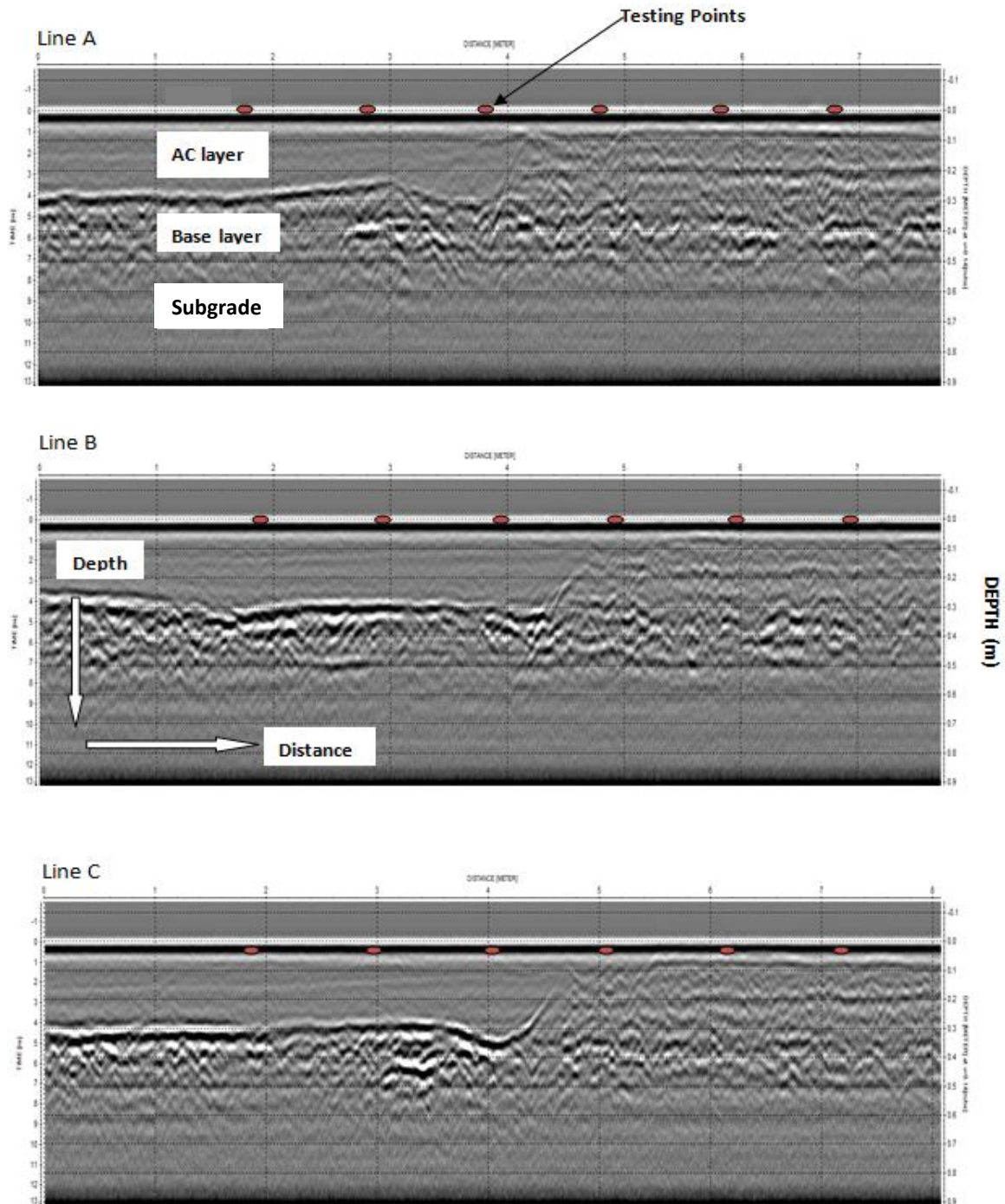


Figure (6-13) GPR B-scans for three test lines.

According to the PSPA results, the average moduli for each line from six points were 1350ksi \approx 9300 MPa, 1500ksi \approx 10300 MPa and 1100 ksi \approx 7600 MPa, respectively. Figure (6-14) illustrates an example of a screenshot for the PSPA program results on point #6 at line A. The yellow bar that is shown in the results is referring to the frequency range that is used in the dispersion analysis, including the calculation of average modulus. The dispersion curve for the test point is plotted across the thickness and averaged for the tested point.

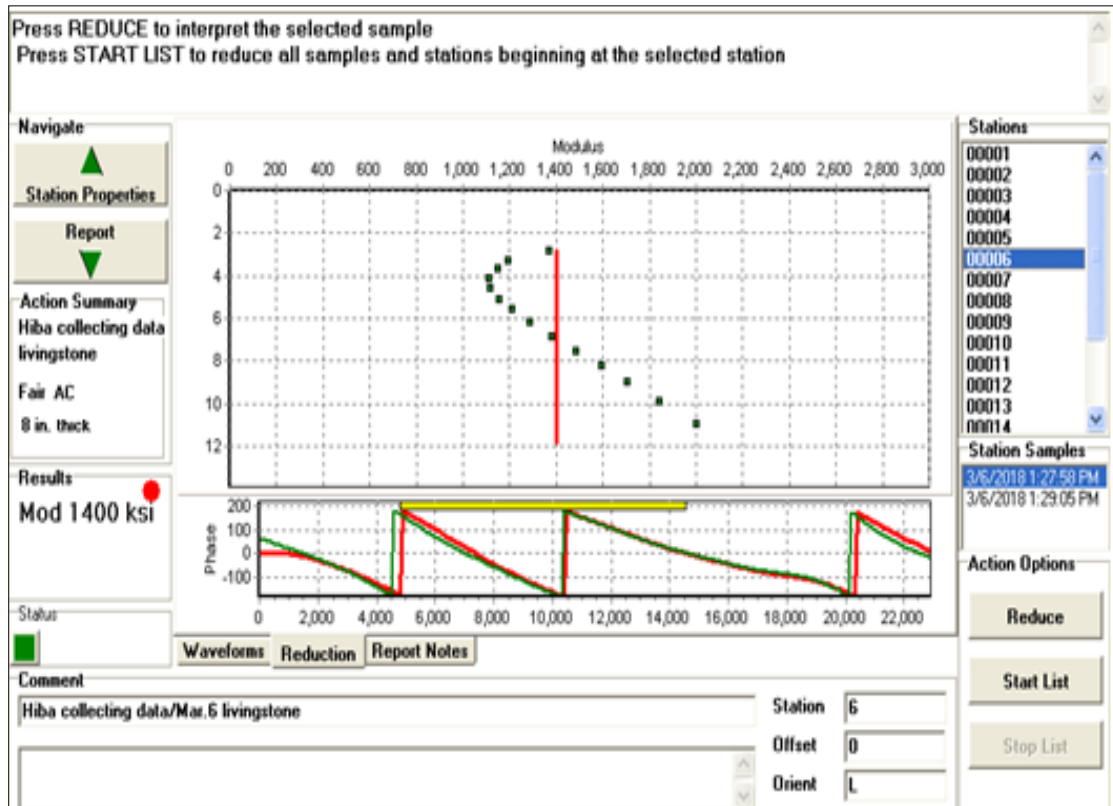


Figure (6-14) PSPA software program user interface

Air-coupled SASW test was implemented on the six fixed positions on each of the three test lines, as shown in Figure (6-15).



Figure (6-15) Implementing air-coupled SASW testing, case study1

To start acquiring the data and display the received signals (i.e. time histories for all receivers), both the hardware and software components have to be set first. For this investigation, three channels (i.e. three microphones) were in use, with a distance from the impact load equal to 0.2m, 0.4m and 0.8m, respectively. The maximum receiver spacing of 0.4 m was an optimum spacing to capture the waves with the wavelength reaching the targeted investigation depth, i.e. the upper part of the subgrade. The microphones were set at the same level above the pavement surface with a minimum distance of 3 mm to avoid the shadow zone, as explained previously in Chapter 3. However, the distance between all microphones and the pavement surface was not constant, since the pavement

surface was uneven, introducing minor errors in the measurements possibly due to the variability in signal amplitudes.

Accordingly, data acquisition parameters were selected, such as the number of samples per each channel, sampling frequency, the receiver configuration (spacing), etc. The selected setting parameters are shown in Figure (6-16).

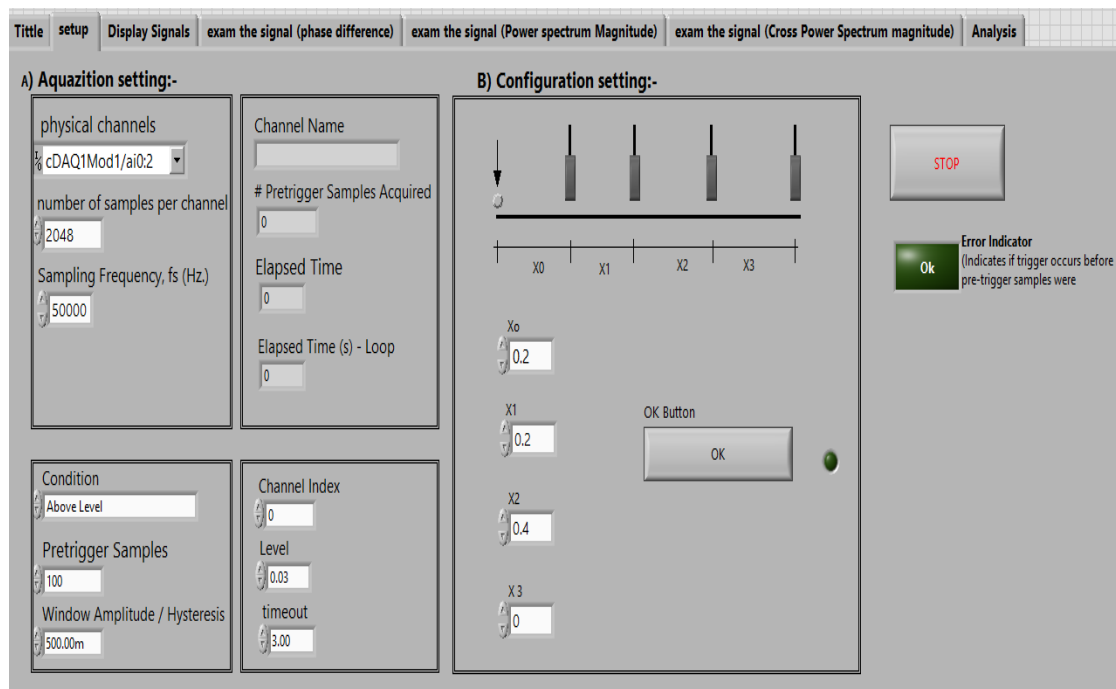
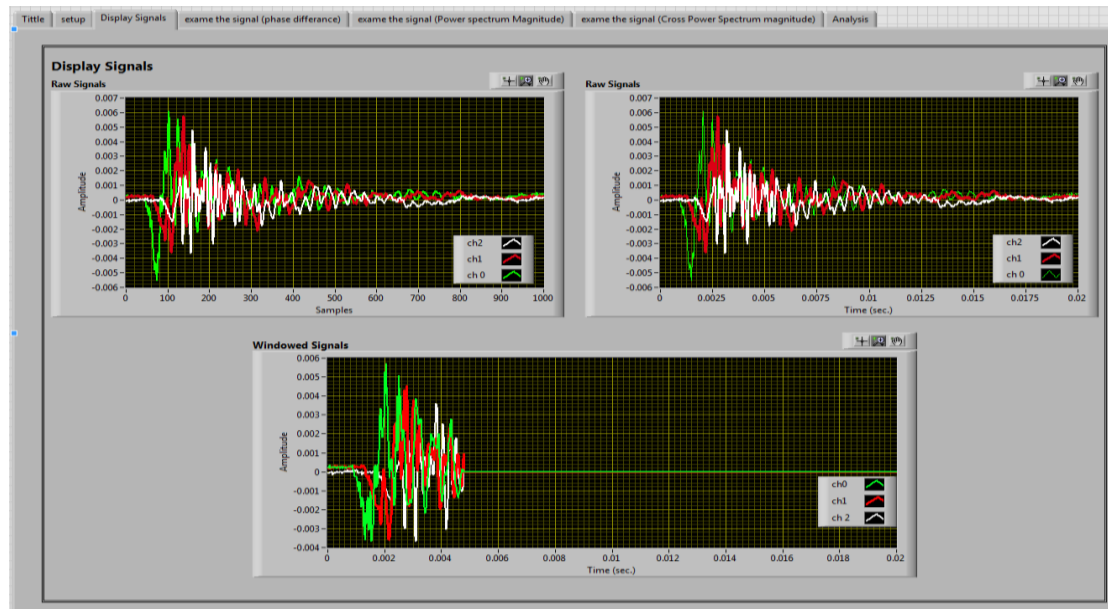
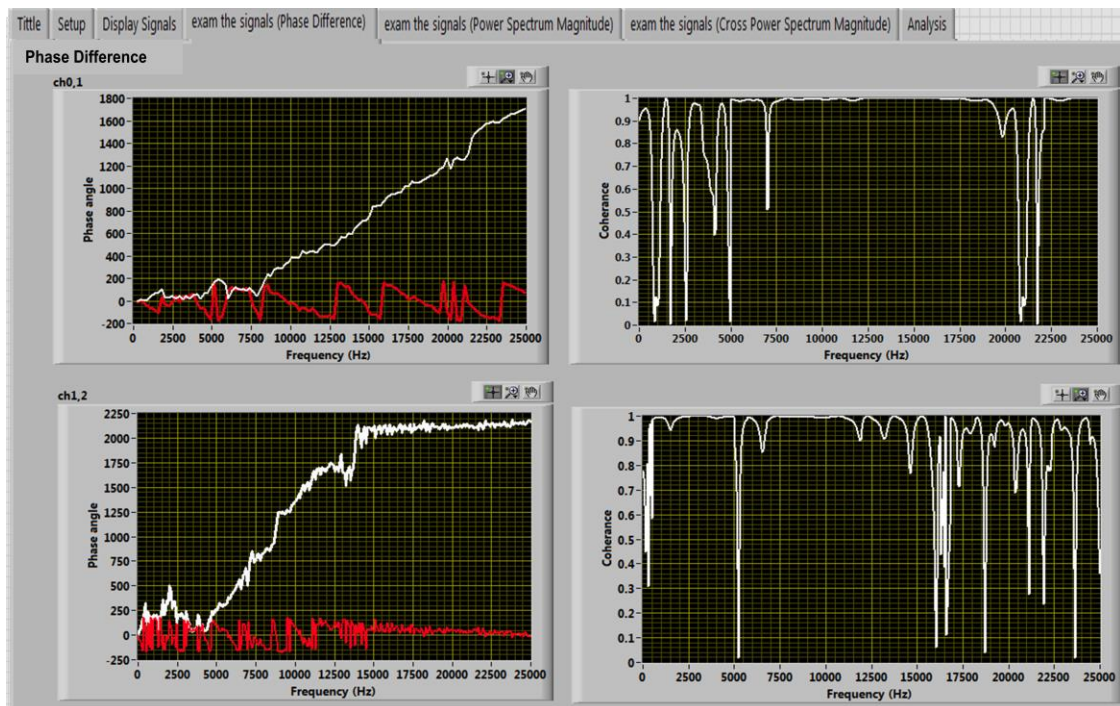


Figure (6-16) The user interface for setting up the input parameters, case study1

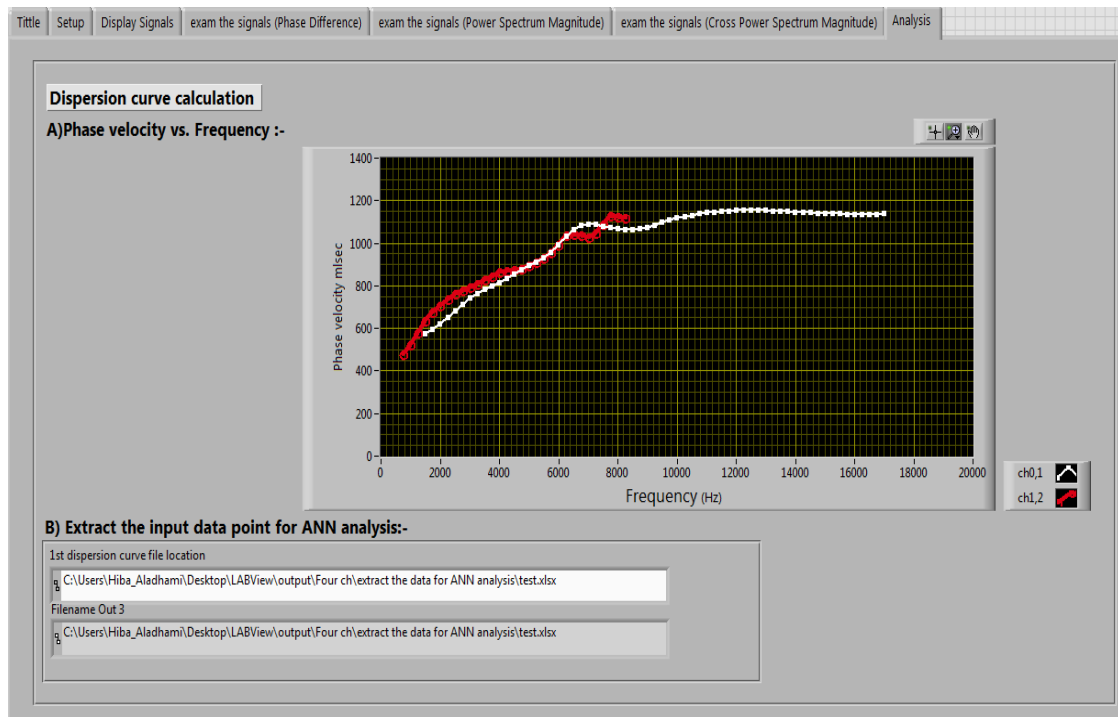
After the hardware/software setup is finished, the test is initiated and the impact load applied. The phase difference, the spectral magnitude and coherence, for at least three repeated signals, are plotted. Figure (6-17) provides an example of data interpretation at one test point.



(a)



(b)



(c)

Figure (6-17) The user interface with the signal acquisition and analysis for point #6 on test line A, case study 1: (a) time histories of acquired signals, (b) wrapped and unwrapped phase, and coherence, and (c) dispersion curve.

As a part of data post-processing within the MATLAB framework, the obtained individual dispersion curves were normalized before their implementation in the validation of the developed ANN models. The curves were normalized with respect to the shear wave velocity V_{s1} and the depth d_1 of the first layer, as explained in Chapter 5. The d_1 was obtained from the GPR survey. V_{s1} can be estimated from either the inspection of the dispersion curve of the near receivers' spacing, or from the PSPA results.

The profiles backcalculated by the developed ANN models at the tested points, based on the individual dispersion curve training strategy are shown in Figure (6-18). A uniform mass density of $1,800 \text{ kg/m}^3$ and a Poisson's ratio of 0.3 were assumed for further calculation of the shear wave velocity of all layers.

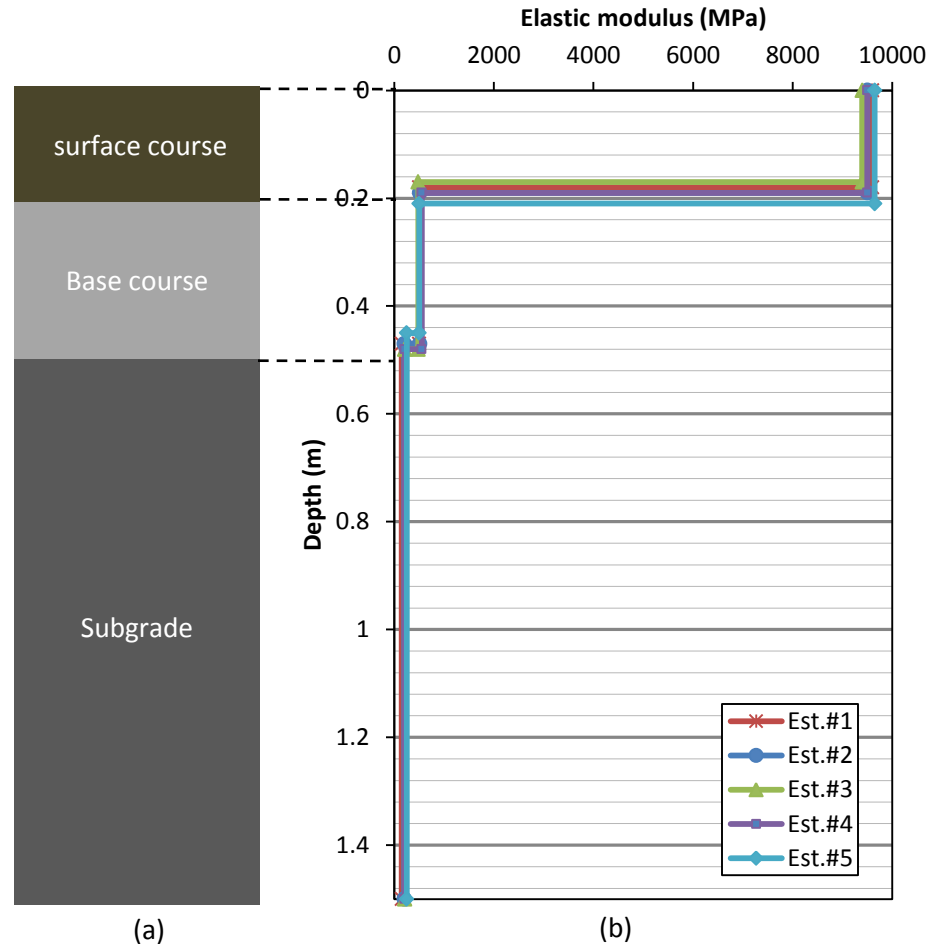


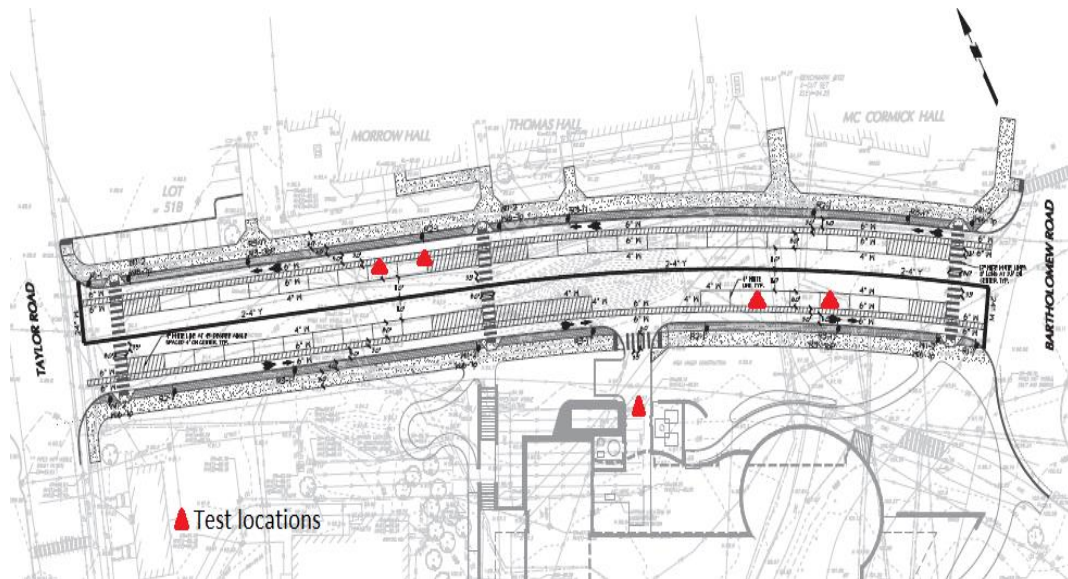
Figure (6-18) Validation of the ANN performance through case study 1: (a) the actual pavement structure profile, (b) estimated elastic modulus profiles.

According to the estimated profile No.1, the first asphalt layer has an estimated depth and an estimated elastic modulus of 0.19 m and 9600 MPa, respectively. The

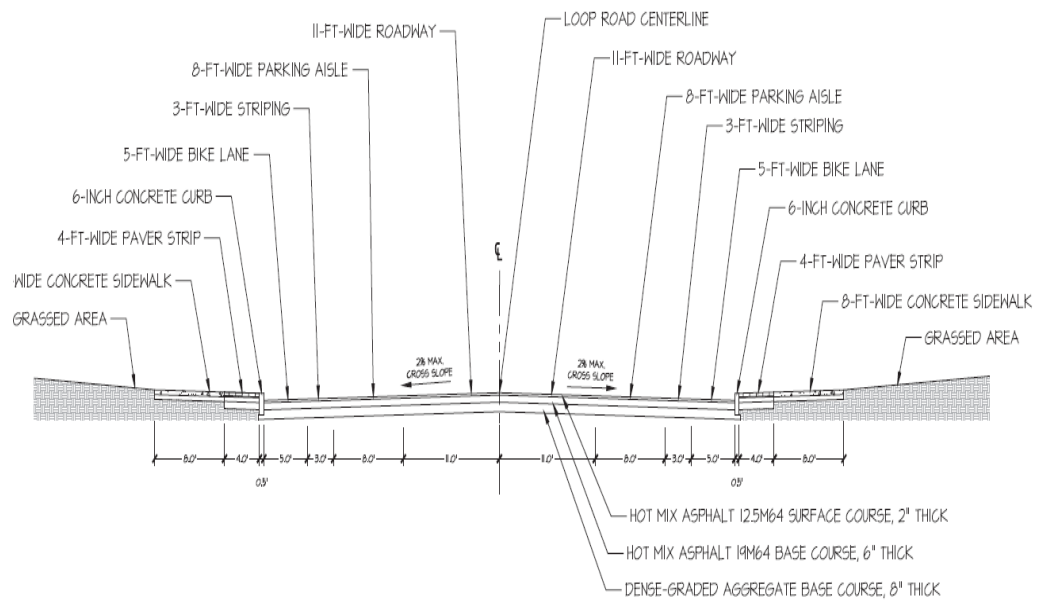
estimated elastic modulus falls into the range of a regular asphalt concrete material (Huang, 1992). Furthermore, the base course has an estimated depth of 0.28m and an estimated elastic modulus of 500 MPa, which falls into the range of a granular base material ranging 220MPa-950MPa (Huang, 1992). It is followed by a lower estimated elastic modulus of the subgrade of 150 MPa. The results demonstrate the capability of the proposed ANN based inversion algorithm. However, it can be noticed that the actual and the estimated pavement layers' thicknesses are not fully matching. That is due to a possible error in the interpretation of the GPR results to estimate the actual layer thicknesses.

6-4-2 Case Study 2

The second validation case study included an investigation of a newly constructed pavement section, for which the design information was available. The location of the tested pavement section was next to the new Richard Weeks Hall of Engineering building on Rutgers' Busch Campus. According to its design information, the pavement profile consists of two AC layers and a dense-graded aggregate base. The thicknesses of the three layers are 0.05m (2in), 0.15m (6in) and 0.2m (8in), respectively. The test location and the typical cross section of the tested pavement section are shown in Figure (6-19).



(a)



(b)

Figure (6-19) Drawings of the tested pavement section next to the Richard Weeks Hall of Engineering: (a) plan view with tested locations, and (b) typical cross-section.

The PSPA was again implemented to evaluate the modulus of AC layer. Figure (6-20) presents a snapshot of the PSPA program interface. The PSPA evaluated elastic modulus of the surface layer was 2380 ksi \approx 16400MPa.

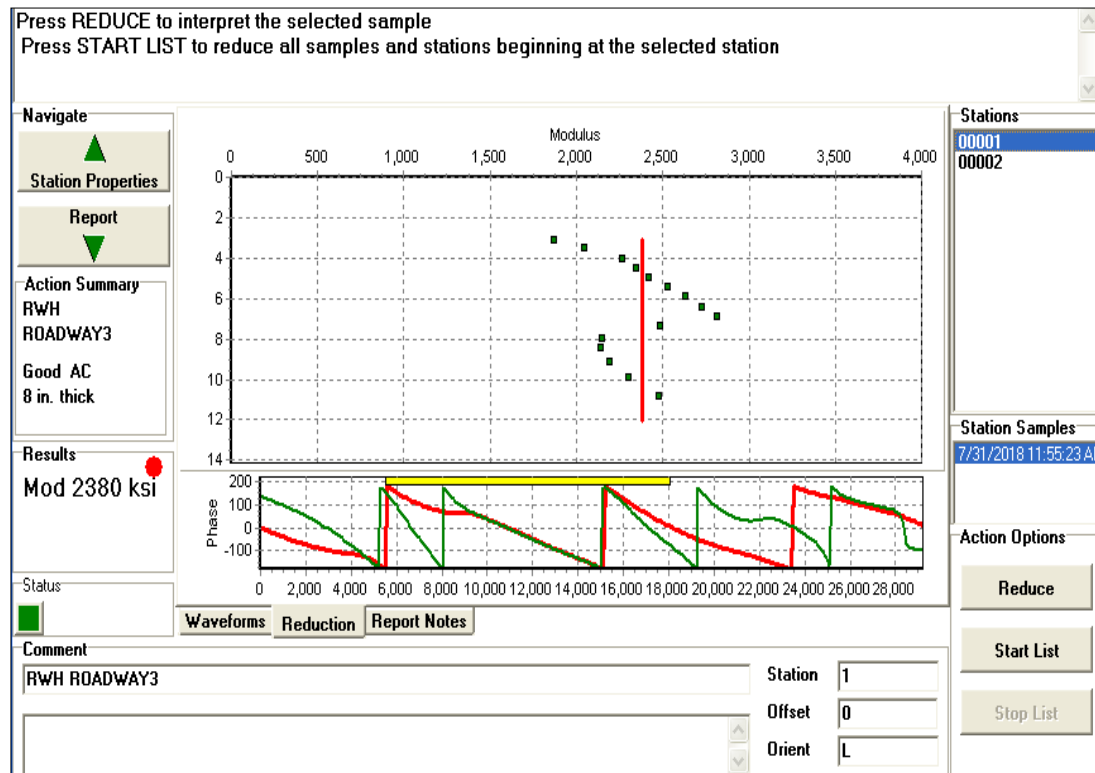


Figure (6-20) PSPA software program user interface, case study 2

The air-coupled SASW test was carried out at selected pavement locations, as shown in Figure (6-21(a)). The same setup and input parameters as in the case study 1 were used in this case study. Figure (6-22) provides snapshots of time histories, the phase of the cross power spectrum, unwrapped phase, coherence, and the dispersion curve for one of the test locations.

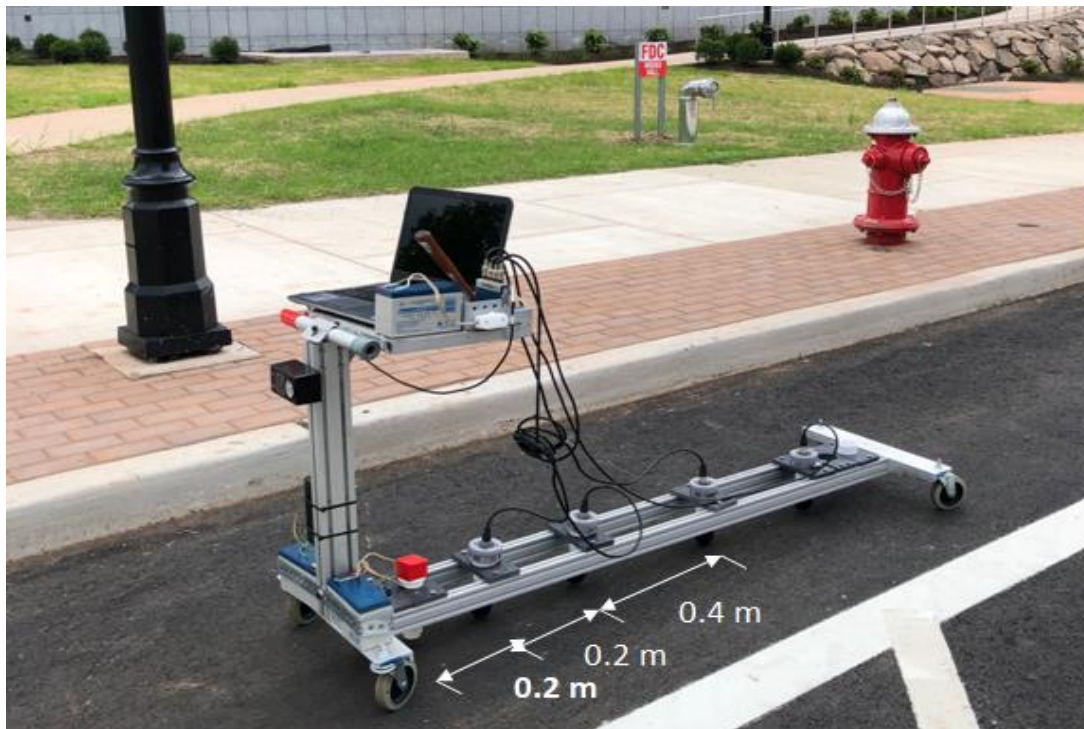
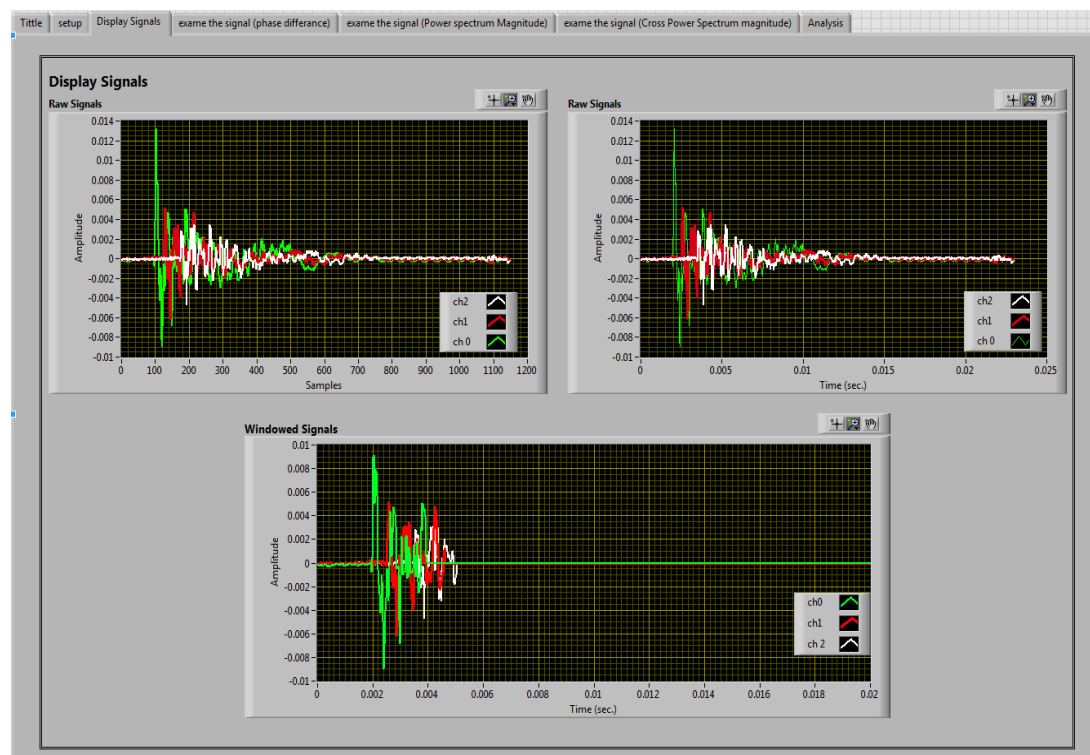
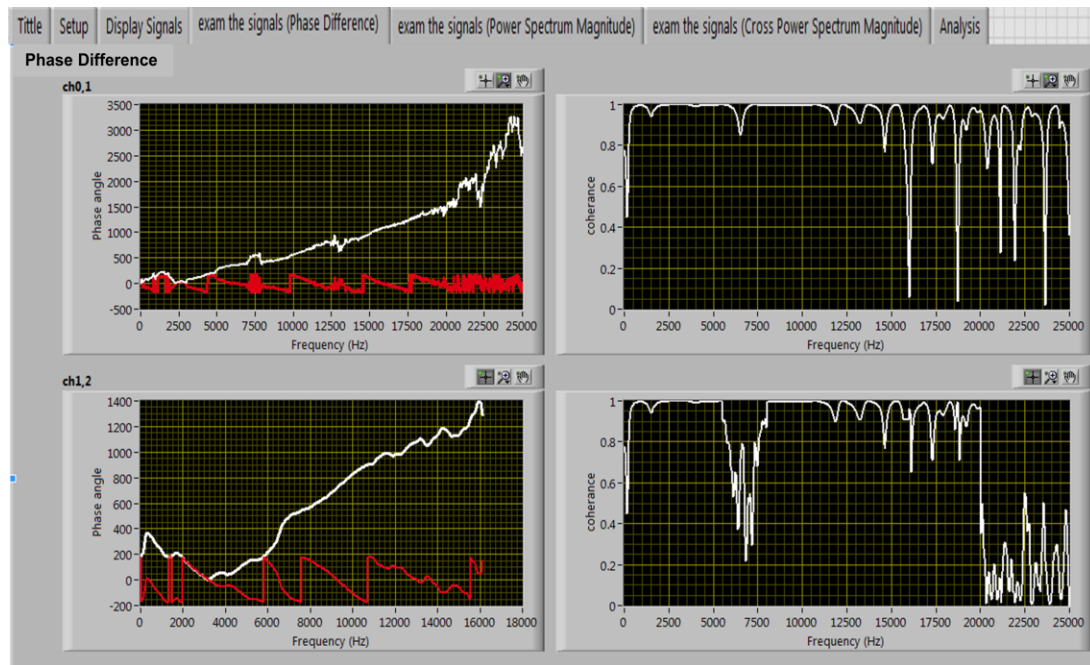


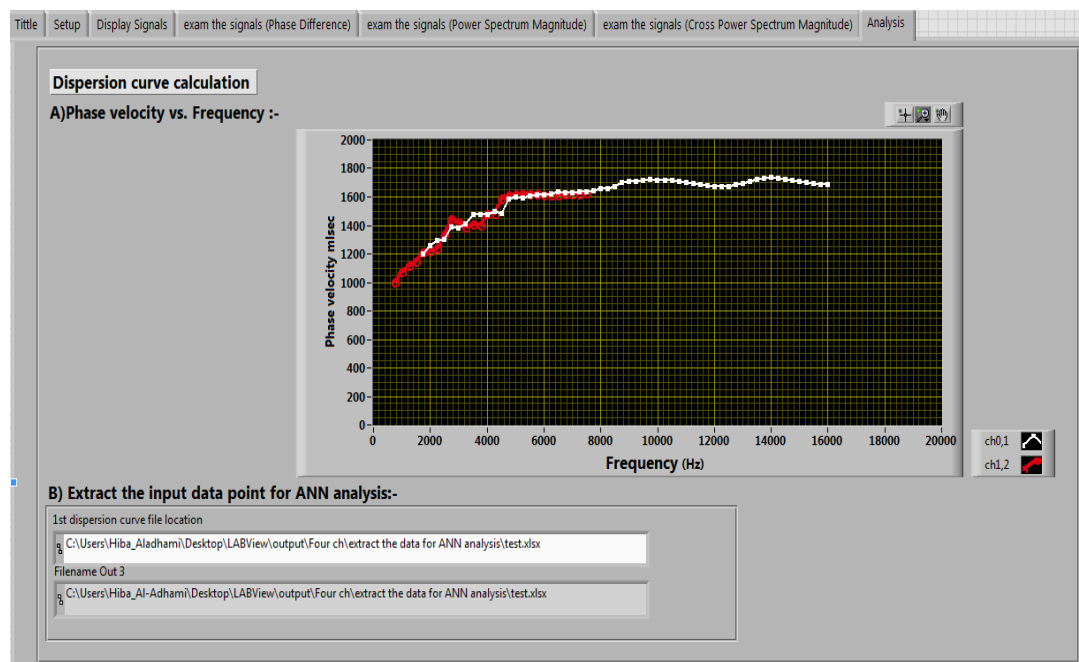
Figure (6-21) Air-coupled SASW testing; case study 2



(a)



(b)



(c)

Figure (6-22) The user interface with the signal acquisition and analysis for a test point in case study 2: (a) time histories of acquired signals, (b) wrapped and unwrapped phase, and coherence, and (c) dispersion curve.

Figure (6-23) provides the pavement profiles backcalculated by the ANN based inversion algorithm trained using individual dispersion curves at different test locations belong case study 2.

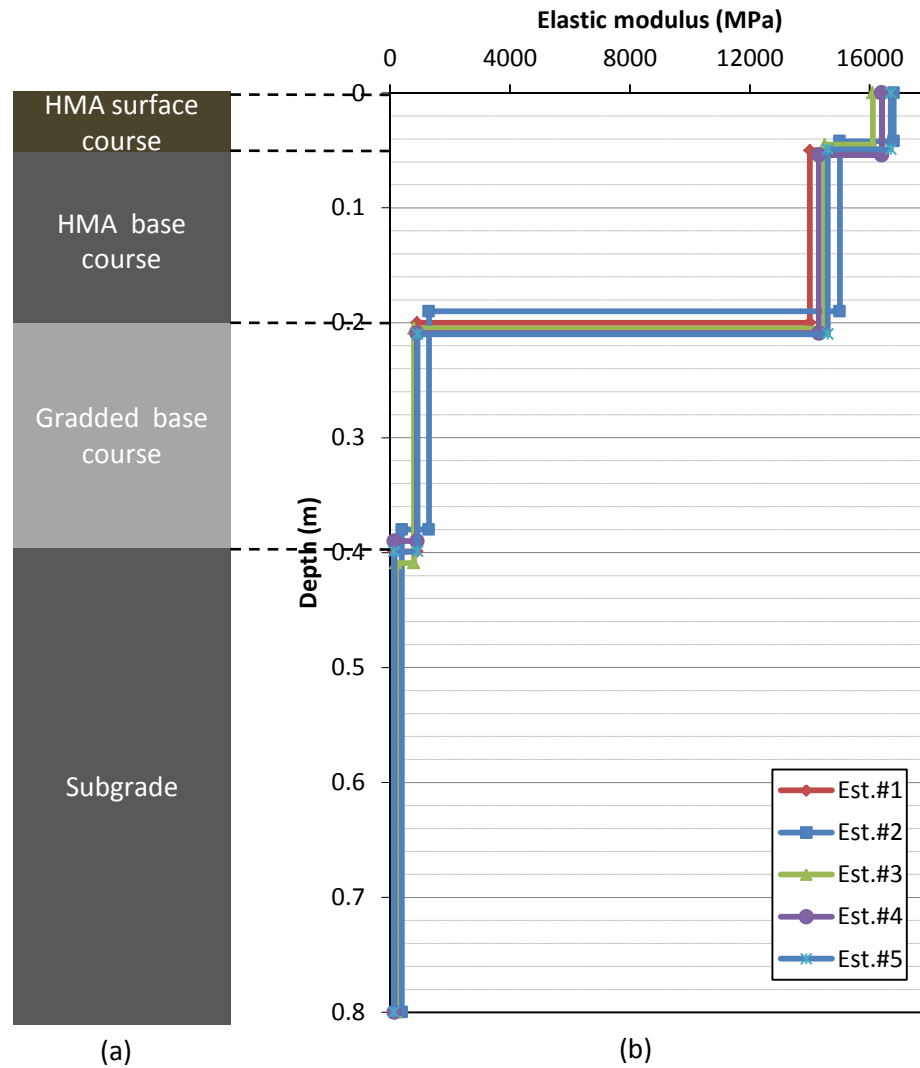


Figure (6-23) Validation of the ANN Performance, case study 2:(a) the actual pavement structure profile (b) estimated elastic modulus profiles.

By considering the estimated profile No.1, the thickness of AC and base layers was predicted accurately. Moreover, according to the estimated elastic moduli profile, the surface and base AC layers had estimated elastic moduli of 16300 MPa and 14000 MPa, respectively, which fall into the range of regular asphalt concrete material at lower temperatures(Huang, 1992), where the air-coupled test was conducted at an average temperature of 4°C (39°F). For the base layer, the estimated elastic modulus was 900 MPa, which falls into a range of a granular base material, 220MPa-950MPa. Moreover, the estimated elastic modulus of the subgrade; at the investigated depth, was 130 MPa. All this indicates that the developed ANN backcalculation algorithm performs well and can be used to evaluate the pavement modulus profile.

CHAPTER SEVEN

Closure

7-1 Summary

Spectral Analysis of Surface Waves (SASW) method is a surface seismic technique that has been used successfully to evaluate soil and pavement profiles. The method is based on the dispersive property of Rayleigh waves in layered systems. To accelerate the data collection, the non-contact SASW test has been used. Non-contact sensors replace ground-coupled sensors by capturing leaky surface waves, instead of ground vibrations, during the test execution.

An automated system for pavement modulus profiling based on air-coupled acoustic testing was developed as a part of this research. In the first phase of the research, numerical simulations of an air-coupled SASW test were conducted using FEA. Several hundred finite element models of various pavement configurations were used to develop an extensive database of surface wave dispersion curves for both three- and four-pavement layer systems. The database was further used to develop an artificial neural network (ANN) for backcalculation of a pavement modulus profile. Different strategies were used to train the ANN models, either by using a database of average dispersion curves, or a database individual receiver spacing dispersion curve. Furthermore, another training strategy was investigated and used to train the ANN models, in which the input points for individual dispersion curves were defined for two frequency steps. A small or short step was assigned to the low-frequency range, long wavelengths, while a large or long step was assigned to the high-frequency range, short wavelengths.

The performance of ANN models was validated using both numerical and field test data. The validation using numerical data included backcalculation of profiles for several additional synthetic pavement profiles and their required input data (i.e., dispersion curves). The actual and predicted pavement modulus profiles were compared. The field validation included implementation of the built non-contact SASW testing system on several pavement sections. The performance of ANN models was evaluated on two pavement sections. The first pavement was an old pavement with no design records available, while the second pavement was a newly constructed pavement with the design information available. To validate the results, the selected pavement sections were also evaluated using ground penetrating radar (GPR) and portable seismic property analyzer (PSPA), which implements the ultrasonic surface waves (USW) method.

7-2 Conclusions

The following conclusions can be drawn based on the results of this research:

1. Numerical simulation

- The surface wave velocities from numerical simulations are very close to those from rigorous theoretical solutions. This is an indication that numerical modeling, in this case using ABAQUS software, can precisely simulate wave propagation in layered systems. Thus, the dispersion curves generated through numerical simulation are accurate and can be used in the development of ANN models.
- Using infinite elements (CINAX4) as an absorbing boundary during the wave propagation simulations is not sufficient to prevent reflection of waves from the

model's edges. Therefore, the overall dimension of the FE model should be tested and verified by using ABAQUS visualization tools.

2. Dispersion curve analysis

- Each pavement layer parameter (i.e., thickness and elastic modulus) has an effect on the shape of its associated dispersion curve. That allows generating a wider training database and enhancing the inversion algorithm, in a way that the problem of one dispersion curve that may refer to different pavement profiles will be minimized.
- The leaky Rayleigh waves captured can be extracted directly from the time histories either by applying an appropriate time window or by using an isolation and signal amplifying technique.
- The suggested filtering criterion is likely to suit all the numerically developed pavement profiles of this research, and it can be used to evaluate the range of wavelength over which required measurements are made.

3. ANN models development

- Increasing the number of hidden layers in an ANN, and the number of nodes in each of the layers, does not guarantee better predictions.
- Developing ANN models for each needed output parameter individually gives a lower mean squared error than the training of networks to predict all the output parameters simultaneously.
- The ANN models developed based on the air-coupled dispersion curves database provide a satisfactory accuracy, based on the evaluation of ANN

model performance using both numerical and field-test data. Therefore, the developed automated system for backcalculation has the capability to predict the pavement profile with sufficient accuracy for practical applications.

- The developed model based on the individual receiver spacing training approach enhances the pavement profile prediction, compared to the average dispersion curve training approach.
- The ANN prediction of the pavement modulus profile is significantly improved by using synthetic dispersion curves that were defined by input points with two frequency steps.

4. Experimental work

- The used regular musical microphones detect the leaky surface waves effectively. The measured signals were captured with an acceptable S/N ratio within the frequency range of interest.
- Using a damper during the air-coupled SASW testing further enhanced isolation of microphones from the cart vibrations, especially during the application of impacts.

7-3 Recommendations for Future Research

The following recommendations describe further possible improvements of the air-coupled SASW test in pavement evaluations:

1. The numerical models presented did not assume any complicating factors commonly encountered in SASW testing, such as presence of other sources of

vibrations and geometrical and material inhomogeneities within the pavement system. Therefore, a more comprehensive numerical study is recommended, which would lead to an enhanced pavement profile evaluation process.

2. To enhance the ability of the air-coupled SAW to evaluate thicker pavement profiles, expanding the database for a large number of receivers and a larger spacing than the current database is recommended.
3. To reduce the effect of direct acoustic waves, and to enhance the signal quality, it is recommended to examine application of parabolic reflectors in SASW testing. As demonstrated by Kee et al.(2012), optimal parabolic domes can significantly improve the signal-to-noise ratio in the air-coupled IE measurements.

REFERENCES

- ABAQUS. (2016). Abaqus analysis user's manual. *Version 6.14-6*. Providence, RI, USA.
- Achenbach, J. D. (1973). Wave propagation in elastic solids. Amsterdam: North Holland.
- Ahmed, M., Tarefder, R. (2017). Incorporation of GPR and FWD into pavement Mechanistic-Empirical design. *Journal of Construction and Building Materials*. 154 (1272–1282).
- Azari, H., Nazarian, S., Yuan, D. (2014). Assessing sensitivity of impact echo and ultrasonic surface waves methods for nondestructive evaluation of concrete structures. *Journal of Construction and Building Materials*. 71(384–391).
- Bathe, K. J. (1996). Finite element procedures. Englewood, NJ: Prentice-Hall, Inc.
- Bolt, D. A. (1976). Nuclear explosions and earthquakes. San Francisco, CA: W. H. Freeman and Co.
- Beale, M., Hagan, M., Demuth, H. (2018). Neural Network Toolbox. The MathWorks Inc.,
- Bishop, C. M. (1995). Neural Networks for pattern recognition. Oxford: Oxford University Press.
- Bungey, J. H., and Millard, S. G. (1993, May). Radar inspection of structures. *In proceedings of institution of civil engineers: structures and bridges* (Vol. 99, No. 2).

- Bungey, J. H. (2004). Sub-surface radar testing of concrete: a review. *Construction and Building materials*, 18(1), 1-8.
- Cook, R. D. (2002). Concepts and applications of finite element analysis. John Wiley and Sons, Inc.
- Chao C., Lin D., Luo H., Wang Y. and Lo w. (2017). Non-destructive evaluation of a city roadway for pavement rehabilitation: A case study. *International Journal of Pavement Research and Technology*, <https://doi.org/10.1016/j.ijprt.2017.12.002>
- Castaings, M., and Hosten, B. (2001). Lamb and SH waves generated and detected by air-coupled ultrasonic transducers in composite material plates. *NDT and E International*, 34(4), 249-258.
- Celaya M., Tabrizi K. and Hameed O. (2018). Detection of buried trolley tracks using multichannel 3D ground penetrating radar technology. Proceedings of NDE/NDT for Highways and Bridges: SMT. ASNT. (80-90).
- Celaya M., Young G., and Nazarian S. (2009), Portable Seismic Property Analyzer Identification of Asphalt Pavement Layers, *Geomedia Research and Development*, Report No.FHWA-CFL/TD-09-002
- Eagleson, B., Heisey, J.S., Hudson, W.R., Meyer, A.H., and Stokoe, K.H., II (1981), IIComparison of Falling Weight Deflectometer and Dynaflect for Pavement Evaluation,II Report No. 256-1, *Center for Transportation Research, University of Texas*, Austin, TX.

- Elmore, W. C., Elmore, W. C., and Heald, M. A. (1969). *Physics of waves*. Courier Corporation.
- Ewing, W. M., Jardetzky, W. S., Press, F., and Beiser, A. (1957). Elastic waves in layered media. *Physics Today*, 10, 27.
- Foti, S., Hollender, F., Garofalo, H., Albarello, D., Asten, M., Bard, P., Giulio, G., Forbriger, T., Hayashi, K., Lunedei, E., Martin, A., Mercerat, D., Ohrnberger, M., Poggi, V., Renalier, F., Sicilia, D., Socco, V. (2017) Guidelines for the good practice of surface wave analysis:a product of the InterPACIFIC. *Journal of Bull Earthquake Eng.*
- Fernando, E., Scullion, T., and Nazarian, S. (2001). Predicting hot-mix performance from measured properties: phase II project documentation.Report No. FHWA/TX-02/0-1708-2
- Tofeldt, O., Ryden, N. (2018), Lamb Wave Phase Velocity Imaging of Concrete Plates with 2D Arrays. *Journal of Nondestructive Evaluation*.37:4.<https://doi.org/10.1007/s10921-017-0457-x>
- Ganji, V., Gucunski, N., and Maher, A. (1997). Detection of underground obstacles by SASW method: numerical aspects. *Journal of Geotechnical and Geoenvironmental Engineering, ASCE*, 212-219.
- Gedge, M., and Hill, M. (2012).Acoustofluidics 17: Theory and applications of surface acoustic wave devices for particle manipulation. *Lab on a Chip*,12(17), 2998-3007.

- Graff, K. F. (1975). Wave motion in elastic solids. Courier Corporation.
- Gucunski, N. (1991). Generation of low frequency Rayleigh waves for the spectral analysis of surface wave method. *PH.D thesis, The university of Michigan*.
- Gucunski, N., and Woods, R. D. (1992). Numerical simulation of the SASW test. *Soil Dynamics and Earthquake Engineering*, 11(4), 213-227.
- Gucunski, N. (1994). Detection of multi-course surface pavement layers by the SASW method. In *Nondestructive Testing of Pavements and Backcalculation of Moduli: Second Volume*. ASTM International.
- Gucunski, N., and Maher, A. (2002). Evaluation of seismic pavement analyzer for pavement condition monitoring. Report No.FHWA-NJ-2002-012.
- Gucunski, N., Slabaugh, G., Wang, Z., Fang, T., and Maher, A. (2008). Visualization and interpretation of impact echo data from bridge deck testing. *Transportation Research Record*, 2050, 11-21.
- Gucunski, N. Maher, A. Ghasemi, H. (2011). Condition monitoring of bridge decks through periodical NDE using multiple technologies. *First Middle East Conference on Smart Monitoring*, Dubai, AUE.
- Gucunski, N., Imani, A., and Romero, F. (2013). Nondestructive Testing to Identify Concrete Bridge Deck Deterioration. REPORT S2-R06A-RR-1.
- Gómez, P., Fernández, J. P., and García, P. D. (2011). Lamb waves and dispersion curves in plates and its applications in NDE experiences using Comsol Multiphysics. *In excerpt from proceedings of 2011 COMSOL Conference*, Stuttgart.

- Haskell, N. A. (1953). The dispersion of surface waves on multilayered media. *Bulletin of the seismological Society of America*, 43(1), 17-34.
- Haas, R., and Hudson, W. R. (1978). *Pavement management systems* (No. Monograph).
- Hadidi, R., and Gucunski, N. (2003). Inversion of SASW dispersion curve using numerical simulation. *Symposium on the application of Geophysics to Engineering and Enviromental Problems* (pp. SUR-01). San Antonio, Texas: SAGEEP.
- Heisey, J. S., Stokoe, I. I., and Meyer, A. H. (1982). Moduli of pavement systems from spectral analysis of surface waves. *Transportation research record*, (852).
- Hecht-Nielsen, R. (1989, June). Theory of the backpropagation neural network. In *Neural Networks, 1989. IJCNN., International Joint Conference on* (pp. 593-605). IEEE.
- Hughes, T. J. (1987). Finite element method- linear static and dynamic finite eLementanalysis. Engleweed, NJ, USA.
- Ismail, M. A., Samsudin, A. R., Rafek, A. G., and Nayan, K. A. M. (2012). Road Pavement Stiffness Determination using SASW Method. *Journal of Civil Engineering, Science and Technology*, 3, 9-16.
- Jackson, H. and Gucunski, N. (2015). Reduction of Impulse-Response Data on Rigid Pavement: Comparison of Single Degree of Freedom, Cone, and Lumped Parameter Dynamic Models. *Journal of Infrastructure Systems*. 4(21)
- Joh, S. H. (1996). *Advances in the data interpretation technique for spectral-analysis-of-surface-wave (SASW) measurements* (Doctoral dissertation).

- Kausel, E., and Peek, R. (1982). Dynamic loads in the interior of a layered stratum: an explicit solution. *Bulletin of the Seismological Society of America*, 72(5), 1459-1481.
- Karim, H., and Al-Qaissi, M. M. (2014). Evaluation of road pavement and subsurface defects mapping using ground penetrating radar (GPR). *Eng. and Tech. Journal, UOT*, Vol. (32A), No. (5), 1240-1250.
- Kee, S. H., and Zhu, J. (2010). Using air-coupled sensors to determine the depth of a surface-breaking crack in concrete. *The Journal of the Acoustical Society of America*, 127(3), 1279-1287.
- Kee, S., Gucunski, G. and Fetrat, F. (2012) Developing an optimal acoustic reflector for air-coupled impact-echo sensor, Proc. SPIE 8347, Nondestructive Characterization for Composite Materials, Aerospace Engineering, Civil Infrastructure, and Homeland Security. <https://doi.org/10.1117/12.914718>
- Kim J.H, K. H.-G. (2008). Nondestructive evaluation of elastic properties of concrete using simulation of surface waves. *Computer-aided Civil and Infrastructure Engineering*, 23(8), 611-24.
- Kim, J. H., and Kwak, H.-G. (2008). Nondestructive evaluation of elastic properties of concrete using simulation of surface waves. *Computer-Aided Civil and Infrastructure Engineering*, 23, 611-624.
- Kolsky, H. (1963). *Stress waves in solids* (Vol. 1098). Courier Corporation.

- Kuttruff, H. (1991), *Ultrasonic fundamentals and applications*, Elsevier Applied Science, New York.
- Lamb, H. (1917, March). On waves in an elastic plate. In *Proceedings of the Royal Society of London A: Mathematical, Physical and Engineering Sciences* (Vol. 93, No. 648, pp. 114-128). The Royal Society.
- Li, J. (2008). Study of Surface Wave Methods for Deep Shear Wave Velocity Profiling Applied in the Upper Mississippi Embayment, *Ph.D.Dissertation*, University of Missouri, Columbia.
- Lowe, M. (1995).Matrix techniques for modeling ultrasonic waves in multilayered media.*IEEE Transactions on Ultrasonics, Ferroelectrics, and Frequency Control*, 525-542.
- Lu, Y., Cao, Y., McDaniel, J. G., and Wang, M. L. (2015). Fast Inversion of Air-Coupled Spectral Analysis of Surface Wave (SASW) Using in situ Particle Displacement. *ISPRS International Journal of Geo-Information*, 4(4), 2619-2637.
- Menke, W., *Geophysical data analysis: discrete inverse theory*, Academic, San Diego, CMif., 1984.
- Moser, F., Jacobs, L. J., and Qu, J. (1999).Modeling elastic wave propagation in waveguides with the finite element method.*NDT&E International*, 32, 225–34 .
- Muller, W., and Reeves, B. (2012). Comparing Traffic Speed Deflectometer and Noise-Modulated Ground Penetrating Radar data for rapid road pavement investigations.

Proceedings of 14th International Conference on Ground Penetrating Radar, Shanghai, China, pp. 502-509.

Nasimifar, M.; Siddhartha, V., Radar, G., and Nazarian, S. (2015). Dynamic analyses of traffic speed deflection devices. *International Journal of Pavement Engineering*. <https://doi.org/10.1080/10298436.2015.1088152>.

Nazarian, S., Stokoe, I. I., Kenneth, H., and Hudson, W. R. (1983). Use of spectral analysis of surface waves method for determination of moduli and thicknesses of pavement systems *Transportation Research Record* (pp. 38-45). Washington D.C.: TRB 930. (No. 930).

Nazarian, Stokoe II, K. H., Briggs, R. C., and Rogers, R. (1987). Determination of pavement layer thickness and moduli by SASW method. *Transportation Research Record* (pp. 133-150). Washington D.C.: 1196.

Nazarian, S., and Desai, M. R. (1993). Automated surface wave method: field testing. *Journal of Geotechnical Engineering*, 119(7), 1094-1111.

Nazarian, S. (1984). In situ determination of elastic moduli of soil deposits and pavement systems by spectral-analysis-of-surface-waves method. *Ph.D. Dissertation University of Texas at Austin*.

Nazarian, S., and Stokoe, K. H. (1986). In situ determination of elastic moduli of pavement systems by spectral analysis of surface waves method (theoretical aspects) *Center for Transportation Research The University of Texas at Austin Austin, Texas*.

- Nazarian, S., Abdallah, I., and Yuan, D. (2004). Neural networks for rapid reduction interpretation of spectral analysis of surface waves results. *Transportation Research Record: Journal of the Transportation Research Board*, (1868), 150-155.
- Orozco, M. C. (2004). Inversion method for spectral analysis of surface waves (SASW), *Ph.D. Dissertation, Georgia Institute of Technology*
- Olson, L., Miller, P. (2018). Concrete Bridge Deck Assessments with Impact Echo for Bare Decks and Surface Waves Scanning for Asphalt Overlaid Decks and Asphalt Pavements. Proceedings of the NDE/NDT for Highways & Bridges: SMT. ASNT.
- Opra, N., Wood, R., and Al-Shayea, N. (1996). Nondestructive Testing of Concrete Structure Using the Rayleigh Wave Dispersion Method. *ACI Material Journal*. 93-M10
- Phillips, L., and Willoughby, K. (2003). Infrared Thermography Revolutionizes Hot-Mix Asphalt Paving. *InfraMation, the thermographer conference*.
- Xia, J., Miller, R. D., & Park, C. B. (1998). Estimation of near-surface shear-wave velocity by inversion of Rayleigh waves. *Geophysics*, 64(3), 691-700
- Qi, Q. (1994). Attenuated leaky Rayleigh wave, *J. Acoust. Soc. Am.* 95, 3222–3230.
- Reeves, B. (2014). Noise Modulated GPR: Second Generation Technology, *15th International Conference on Ground Penetrating Radar - GPR*, 708-713.

- Reeves, B., and Muller, W. (2012).Traffic-speed 3-D Noise Modulated Ground Penetrating Radar (NM-GPR). *Proceeding of 14th International conference on Ground Penetrating Radar*, Shanghai, China, pp. 165-171.
- Richart, F. E. (1962). Foundation vibrations. *Transactions of the American Society of Civil Engineers*, 127(1), 863-897.
- Richart, F. E., Hall, J. R., and Woods, R. D. (1970).Vibrations of soils and foundations. . *Prentice-Hall International Series in Theoretical and Applied Mechanics*. Englewood Cliffs, Nj, Usa.
- Rose, L. J. (2004).Ultrasonic waves in solid media. *Cambridge University Press*
- Ryden, N., Park, C. B., Ulriksen, P., and Miller, R. D. (2004).Multimodal approach to seismic pavement testing.*Journal of Geotechnical and Geoenvironmental Engineering, ASCE*, 130(6), 636-645.
- Ryden, N. (2004). Surface Wave Testing of Pavements.*Ph.D.Dissertation. Department of Engineering Gelogy, Lund Institute of Technology, Lund University*.
- Ryden, N., Lowe, M. J. S., andCawley, P. (2009).Non-contact surface wave testing of pavements using a rolling microphone array. *Proceedings of the NDTCE, Nantes, France*, 30.
- Sansalone, M. C. (1987). A finite element study of the interaction of transient stress waves with planar flaws. *Journal of Research of the National Bureau of Standards*, 92(4), 279-290.

- Sansalone, M., Carino, N. J., and Hsu, N. N. (1987). A finite element study of transient wave propagation in plates. *Journal of Research of the National Bureau of Standards*, 92(4), 267-278.
- Sharpe, P., Solly, R. (1995). Dealing with missing values in neural network-based diagnostic systems. *Neural Comput & Applic*, 3(2), 73–77 <https://doi.org/10.1007/BF01421959>
- Shirazi, H., Abdallah, I., Nazarian, S. (2009). Developing Artificial Neural Network Models to Automate Spectral Analysis of Surface Wave Method in Pavements. *Journal of Materials in Civil Engineering*. Volume 21, Issue 12.
- Smith, K., Bruinsma, J.E., Wade, M.j., Chatti, K., Vandenbossche, J., and Yu, H.T.(2017). Using Falling Weight Deflectometer Data with Mechanistic-Empirical Design and Analysis, Volume I: Final Report FHWA-HRT-16-009
- Tarantola, A. (2005). Inverse problem theory and methods for model parameter estimation. *Society of Industrial and Applied Mathematics 'SIAM'*.
- Thomson, W. T. (1950). Transmission of elastic waves through a stratified solid medium. *Journal of applied Physics*, 21(2), 89-93.
- Tokimatsu, K., 1997. “Geotechnical Site Characterization Using Surface Waves”, *Earthquake Geotechnical Engineering*, Ishihara (ed.), Baklava, Rotterdam, p1333 – 1368.
- Viktorov, I. A. (1967). Rayleigh and Lamb waves: physical theory and applications, vol. 147.

- Villacorta, F. L., Nordbeck, A. V. and Timm D. H. (2017). Non-destructive evaluation of sustainable pavement technologies using artificial neural networks. *International Journal of Pavement Research and Technology*, 10, (139-147).
- Viktorov, I. A. (1967). Rayleigh and Lamb Waves ,Plenum, New York..
- Wolf, J. P. (1985). *Dynamic soil-structure interaction*. Englewood Cliffs, N.J.: Prentice-Hall.
- WANG, H. (2011). Analysis of tire-pavement interaction and pavement responses using a decoupled modeling, *Ph.D. Dissertation*, University of Illinois, Urbana-Champaign.
- Wang, H., and Li, M. (2016). Nondestructive evaluation of pavement structural conditionfor rehabilitation design. TRID, <https://trid.trb.org/view.aspx?id=1319876>
- Williams, T. P., and Gucunski, N. (1995). Neural networks for backcalculation of moduli from SASW test. *Journal of computing in civil engineering*, 9(1), 1-8.
- Wilby, R. L., T. Wigley, D. Conway, P. Jones, B. Hewitson, J. Main, and D. Wilks, (1998). Statistical downscaling of general circulation model output: A comparison of methods. *Water Resources Research*, 34 (11), 2995–3008.
- Woods, J. D. (1968). Wave-induced shear instability in the summer thermocline. *Journal of Fluid Mechanics*, 32(04), 791-800.
- Wu, J., Liang, J., and Adhikari, S. (2014). Dynamic response of concrete pavement structure with asphalt isolating layer under moving loads. *Journal of Traffic and Transportation Engineering (English Edition)*, 1(6), 439-447.

- Yuan, D., and Nazarian, S. (1993). Automated surface wave method: inversion technique. *Journal of Geotechnical Engineering*, 119(7), 1112-1126.
- Zafka, A., and Sudyka, J.,(2015). Traffic speed deflectometer (TSD) measurement for pavement evaluation. *International symposium, Non-Distructive Testing in Civil Engineering (NDT-CE)*, Berth, Germany.
- Zerwer, A. C. (2002). Parameter estimation in finite element simulation of Rayleigh wave. *Journal of Geotechnical and Environmental Engineering, ASCE*, 128(3), 250-261.
- Zhu, J., and Popovics, J. (2002, May). Non-contact detection of surface waves in concrete using an air-coupled sensor. *In Quantitative Nondestructive Evaluation* (Vol. 615, No. 1, pp. 1261-1268).AIP Publishing.
- Zhu, J., and Popovics, J. S. (2007).Imaging concrete structures using air-coupled impact-echo. *Journal of engineering mechanics*, 133(6), 628-640.